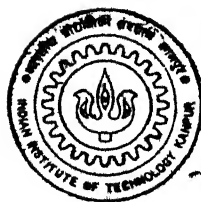


**Effects of granularity and correlated pinning disorder
on vortex dynamics in highly oriented platelets of
bismuth based cuprate superconductors**

by

Satyabrata Patnaik

TH
PHY/1999/P
P273C



DEPARTMENT OF PHYSICS

INDIAN INSTITUTE OF TECHNOLOGY KANPUR

AUGUST, 1999

**Effects of granularity and correlated pinning disorder
on vortex dynamics in highly oriented platelets of
bismuth based cuprate superconductors**

A thesis submitted

in Partial Fulfilment of the Requirements

for the Degree of

Doctor of Philosophy

by

Satyabrata Patnaik

to the

DEPARTMENT OF PHYSICS

INDIAN INSTITUTE OF TECHNOLOGY KANPUR

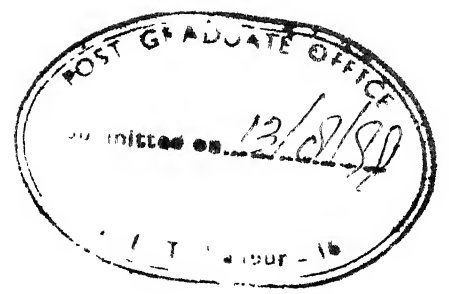
AUGUST 1999

74 JUN 2000
CENTRAL LIBRARY
I. I. T., KANPUR
A 131101

TH
Faint handwritten text

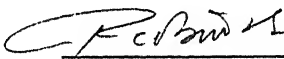


A131101



CERTIFICATE

It is certified that the work contained in this thesis entitled "*Effects of granularity and correlated pinning disorder on vortex dynamics in highly oriented platelets of bismuth based cuprate superconductors*", by Satyabrata Patnaik, has been carried out under my supervision and that this work has not been submitted elsewhere for a degree.

 12/8/99

Dr. R. C. Budhani

Professor

Department of Physics

Indian Institute of Technology

Kanpur

August, 1999

Synopsis

**Title : Effects of granularity and correlated pinning disorder on
 vortex dynamics in highly oriented platelets of bismuth
 based cuprate superconductors**

Name of the student:	Satyabrata Patnaik
Registration Number:	9310970
Degree for which submitted:	Doctor of Philosophy
Department:	Physics
Thesis Supervisor:	Prof. R. C. Budhani
Month and year of submission:	August 1999

Encompassing immense technological potential and fundamental science, vortex physics in high-temperature superconductors is in the forefront of condensed matter research in the recent years. While the ramifications of disorder and thermal fluctuations on statistical mechanics of vortices in anisotropic systems are the focus of theoretical interpretations, the enhancement of critical current density at liquid nitrogen temperature is the core issue from the technological point of view. Additionally, applications in the heavy engineering sector demand long lengths of superconducting conductors. While the propensity of $\text{Bi}_2\text{Sr}_2\text{CaCu}_2\text{O}_8$ (Bi-2212) and $(\text{Bi-Pb})_2\text{Sr}_2\text{Ca}_2\text{Cu}_3\text{O}_{10}$ (Bi-2223)

superconductors for a rapid platelet type growth in the ab - plane has been responsible for the phenomenal success in fabrication of silver sheathed multifilamentary tapes of these materials, problems remain with their capacity to carry useful current at 77 K, particularly in the presence of a magnetic field. The onset of dissipation in the presence of a magnetic field is due to the motion of grain boundary and intragrain fluxons in these well oriented polycrystalline materials. At lower temperatures, the vortices develop rigidity due to a stronger Josephson coupling between the grains and between copper oxide planes. A rigid flux line is effectively pinned by structural defects present in the material. At lower temperatures one can therefore foresee usages of these composite superconductors in simple dc magnets and the magnets for Tokamak fusion devices and magnetic resonance imaging. While in the first case the fluxons are subjected to a static Lorentz force, in the latter two situations the force has an oscillatory component as well.

The vortex dynamics in composite conductors of Bi-2212 and Bi-2223 cuprates has been studied thus far primarily using in-plane dc transport and magnetization measurements and through low frequency (~ 60 Hz) ac loss measurements. Similar studies have also been used to establish the flux pinning effects of irradiation induced point and extended defects. These studies have not been able to correlate the effect of characteristic granularity and weak link behaviour with current carrying capacity and history effects in tape samples. Understanding of the granularity and alignment aspects is essential for devising ways and means to enhance the critical current density in these inhomogeneous materials. It has been established that high frequency techniques are most suitable to study the interaction between the vortices and weak links in granular superconductors.

The prime motivation for this thesis is to study the effect of growth related intrinsic defects and heavy ion irradiation induced extrinsic defects on the DC and radio frequency vortex dynamics in the technologically important tape samples of bismuth based cuprates (BiSCCO). In our high frequency experiments, the silver sheath is removed by a unique chemical treatment and the true superconducting properties of the platelet samples are investigated. The variables in our experiments are; i) temperature (10 K to T_c), ii) DC

magnetic field strength (0 to 8 kG), iii) extrinsic disorder density (unirradiated, 2.5×10^{10} defects per cm^2 and 1.5×10^{11} defects per cm^2), iv) anisotropy (Bi-2223 and Bi-2212), v) angle with respect to *ab*-plane (0° - 360°), and vi) frequency (rf and DC).

Chapter 1 of the thesis draws the broad outline of the work and defines the questions that are dealt with in the subsequent chapters. It starts with a brief introduction to vortices in superconductors and discusses the modifications to the equilibrium behaviour due to the structural anisotropy, which is particularly the case with the copper oxide based layered superconductors. The dynamics of vortices under the influence of rf currents is discussed next and various aspects of the mixed state e.g. pinning and flux flow properties, granularity and hysteresis, and flux lock-in effects due to intrinsic and extrinsic pinning are reviewed. A brief summary of important results on dimensionality of vortices studied by DC flux transformer measurements is also included.

Two experimental techniques are reported in this work and a description of these is the main subject matter of Chapter 2. The techniques are; i) a radio frequency penetration depth measurement apparatus, and ii) a six terminal DC flux transformer transport measurement setup. The chapter begins with a discussion on the surface morphology and microstructural aspects of Bi-2223 and Bi-2212 tapes studied through X-ray, Scanning Electron Microscopy (SEM) and Electron Probe Micro Analysis (EPMA). The relevant physical parameters for the creation of columnar defects by irradiating the samples with 6 GeV lead ions are discussed. The design, fabrication, interfacing and calibration of the two experimental setups are presented in detail.

Chapter 3 is about the pinning and flux flow properties of Bi-2223 tape samples studied by the rf penetration depth technique. In all the experiments the rf field is always orthogonal to the external DC field. In the beginning the theoretical aspects of data interpretation using the Coffey - Clem model are discussed. In these high temperature, low - field studies, the different regimes of rf vortex dynamics are identified. The bulk pinning force constants (Labush parameter) and coefficient of viscosity are calculated and are compared to that of the irradiated sample.

Chapter 4 includes the angular dependence of the rf penetration depth in unirradiated and irradiated samples of Bi-2223. The inductive response shows a minimum when the external field is brought into alignment with the columnar defects (CDs). While this characteristic feature of anisotropic pinning due to the CDs disappear in a temperature regime where the J_c is high, in the vortex liquid state closer to T_c this feature grows with the increasing field strength. The overall changes in the angular dependence of rf penetration depth are discussed in the framework of the Bose glass theory for vortex dynamics in highly layered superconductors.

Chapter 5 deals with the identification of granularity using the rf technique. An anomalous hysteretic behaviour is seen in the rf penetration depth of unirradiated and heavy ion irradiated Bi-2223 platelets under field cycling. The range of temperature over which the hysteresis is seen depends on the strength of intragranular pinning. The observed behaviour is discussed quantitatively on the basis of the two-level critical state model of Ji, Rzechowski, Anand and Tinkham for microwave field penetration in inhomogeneous superconductors.

Chapter 6 focuses on DC Flux transformer experiments on silver sheathed Bi-2223 samples. A two level resistive transition, meaning a delayed onset of flux flow resistivity along the c-axis as compared to the ab-plane resistivity is observed. The studies identify various vortex liquid regimes with different c-axis correlation for the unirradiated and heavy ion irradiated tape samples. These observations are compared with reported FT measurements on $\text{YBa}_2\text{Cu}_3\text{O}_7$ and $\text{Bi}_2\text{Sr}_2\text{CaCu}_2\text{O}_8$ single crystals.

$\text{Bi}_2\text{Sr}_2\text{CaCu}_2\text{O}_8$ phase of the bismuth based high T_c cuprates is known to be more anisotropic as compared to the Bi-2223 phase. Chapter 7 presents rf penetration depth experiments on irradiated and as grown samples of Bi-2212 platelets. In the unirradiated samples, the rf response shows a characteristic feature which has been identified with vortex solid to vortex liquid transition. Some aspects of 2D scaling and flux lock-in effects are studied in the vortex liquid and solid phases respectively. Many important

parameters like the Ginzburg number and the mass anisotropy are ascertained for these tape samples.

In the end, Chapter 8 summarizes the main results of this thesis and proposes scope for future work.

Acknowledgements

I acknowledge, with deep sense of gratitude, the tremendous amount of help and guidance I received from my Thesis Supervisor Prof. R. C. Budhani during the course of this work. He introduced me to this fascinating area of research and taught me many things which will have broader implications in my life. I thank him from the core of my heart.

I thank Dr. M. Suenaga and Dr. Arup. K. Ghosh of Brookhaven National Laboratory, U.S.A. for supplying the superconducting tape samples used in this study. Dr. Marcin Konczykowski carried out the irradiation experiment on these samples. I am indebted to him. This research work is a part of an Indo-French project. The Indo-French Center for the Promotion of Advanced Research, New Delhi has been kind enough to grant financial assistance for this work and for a scientific visit to the laboratory of Prof. Hélène Raffy at the Laboratoire des Physique des Solides, Orsay, France. This visit gave me good exposure to the new trends in my area of research.

Sincere thank is also due to Prof. A. K. Majumdar, Dr. M. K. Verma and Dr. K. P. Rajeev for agreeing to be in my peer group committee.

I am happy to be part of the setting up team of our laboratory. That gave me opportunity to learn many new things and I wish I could use all of them. I will always remember the crucial help and good will I received from the technicians of our Institute Workshops especially at the Physics Workshop, Glass-Blowing Section, Precision Workshop and at the liquid helium/ liquid nitrogen plant. I thank Mr. Pramod Sharma for sharing the burden during the setting up period of our low temperature laboratory.

In the lab., Abhay and Himadri taught me interfacing. Chaitali, Leena, Prahallad Navneet and Vivekanand helped me in many ways. Anil's help was crucial in typing the manuscripts and drawing the Figures. I am indebted to all of them and I wish them good luck in their life ahead.

Finally, I wish to thank my parents for having unshakable faith in me.

Satyabrata Patnaik.

All affirmations are denied to lead to
a wider affirmation of the same
reality.

Sri Aurobindo in “ *The Life Divine*”

Contents

Synopsis	iii
Acknowledgements.....	viii
List of Figures.....	xiv
1 Introduction	1
1.1 Vortices in superconductors and vortex dynamics.....	2
1.1.1 The vortex state.....	2
1.1.2 Vortex dynamics.....	5
1.1.2.1 Vortex dynamics at rf frequency.....	5
1.1.2.1a Homogeneous superconductors with pinning disorder.....	5
1.1.2.1b RF vortex dynamics in granular superconductors.....	8
1.2 Bi-2223 and Bi-2212 superconducting tapes.....	8
1.2.1 Structure and physical properties.....	8
1.2.2 Vortex dynamics in bismuth family of superconducting tapes.	13
1.3 Motivation for the present work.....	15
2 Experimental details.....	17
2.1 Introduction.....	17
2.2 The samples, controlled defect generation and microstructure study.....	18
2.3 RF penetration depth measurement.....	25
2.3.1 The technique.....	25

2.3.2	Apparatus description.....	28
2.3.2.1	Electronic circuitry.....	28
2.3.2.2	Design and fabrication.....	32
2.3.2.3	Calibration.....	34
2.4	DC Flux Transformer experiment.....	40
2.4.1	The technique.....	40
2.4.2	Apparatus description.....	40
3	Pinning and flux flow properties of Bi-2223 tapes.....	44
3.1	Introduction.....	44
3.2	Results of unirradiated Bi-2223 platelets.....	46
3.2.1	Temperature dependence of rf penetration depth.....	46
3.2.2	Field dependence for $H \parallel c$ -axis.....	47
3.2.3	Field dependence for $H \parallel ab$ plane.....	53
3.2.4	Angular dependence of the rf response.....	56
3.3	Pinning enhancement with heavy ion irradiation.....	59
3.3.1	Temperature dependence of the frequency shift.....	59
3.3.2	Field dependence of frequency shift.....	59
3.4	Summary.....	68
4	Angle selective vortex dynamics in HII Bi-2223.....	69
4.1	Introduction.....	69
4.2	Results and discussion.....	71
4.2.1	Angular studies on unirradiated sample.....	71
4.2.2	Angular studies on 0.5 T irradiated sample.....	73
4.2.3	Angular studies on 3 T irradiated sample.....	75
4.3	Models for angular selectivity in HII anisotropic superconductors.....	80
4.4	Summary.....	82

5	Granularity and hysteresis in Bi-2223 tapes.....	83
5.1	Introduction.....	83
5.2	Results and discussion.....	84
5.2.1	Hysteresis in unirradiated Bi-2223.....	84
5.2.2	Hysteresis in irradiated Bi-2223.....	87
5.2.3	Ji, Rzechowski, Anand and Tinkham (JRAT) model.....	91
5.2.4	Quantitative analysis using the JRAT model.....	93
5.3	Summary.....	97
6	Flux Transformer experiment and vortex phases in Bi-2223 tapes.....	98
6.1	Introduction.....	98
6.2	Brief overview of results and discussion.....	100
6.2.1	The case of unirradiated Bi-2223 tape.....	100
6.2.2	Modifications in the strong pinning regime.....	104
6.2.3	Comparison between irradiated and unirradiated case.....	108
6.2.4	Arrhenius plots and the activation energy.....	110
6.3	Summary.....	112
7	Anisotropy dominated rf vortex dynamics in Bi-2212 tapes.....	113
7.1	Introduction.....	113
7.2	Results and discussion.....	114
7.2.1	Temperature dependence of rf penetration depth.....	114
7.2.2	Field dependence of unirradiated Bi-2212 platelets.....	115
7.2.3	Angular dependence.....	121
7.2.4	Determination of anisotropy factor γ	124
7.2.5	Field dependence of 0.5 T irradiated Bi-2212.....	127
7.3	Summary.....	131

8 Conclusion and scope for further work.....	132
8.1 Pinning and flux flow properties of Bi-2223 tapes.....	133
8.2 Angle selective response in HII Bi-2223 tapes... ..	133
8.3 Granularity and hysteresis..... ..	134
8.4 Transport measurements in the FT geometry..... ..	134
8.5 Vortex dynamics in Bi-2212 tapes.....	134
8.6 Scope for further work	135
References.....	137
List of Publications.....	144

List of Figures

Figure 1.1	Equilibrium vortex phase diagram for a highly anisotropic high T_c superconductor with (a) weak random pinning and (b) strong random pinning.....	4
Figure 1.2	Crystal Structure of Bi-2212 and Bi-2223. The schematic representation of the layered structure is also shown.....	10
Figure 1.3	Single vortex in an anisotropic superconductor when the field is applied parallel to the sample plane.....	11
Figure 2.1	Main steps for the preparation of the PIT BiSCCO tapes using spray pyrolysis technique.....	20
Figure 2.2	EDX study on a Bi-2212 sample after removing the silver sheath by chemical treatment.....	22
Figure 2.3a	X - ray diffraction studies on a Bi-2223 platelet. H, L and A stand for Bi-2223, Bi-2212 and silver respectively.....	23
Figure 2.3b	X - ray diffraction studies on a Bi-2212 platelet. L and A stand for Bi-2212 and silver respectively.....	23
Figure 2.4a	A SEM micrograph of Bi-2223 sample.....	24
Figure 2.4b	A SEM micrograph of Bi-2212 sample.....	24
Figure 2.5	Effective area of flux expulsion when the dc field is applied perpendicular to the sample plane.....	27
Figure 2.6	Enhanced rf field penetration with an external dc field depends on strength of vortex pinning in the material.....	27
Figure 2.7	A series parallel tunnel diode oscillator circuit. Values of the circuit elements are given in the text.....	30
Figure 2.8	Block diagram of Interfacing of the tunnel diode oscillator experiment.....	33

Figure 2.9 Sample Mounting stage of the cryostat: (a) Cross-sectional view of the copper pillbox housing two LC tank circuits. (b) The sapphire plate and the ceramic cubes are shown separately.....	35
Figure 2.10 Schematic diagram showing the inductor coil, superconducting platelet sample and orientation of magnetic fields and crystallographic axes.....	36
Figure 2.11 Block diagram of the rf penetration depth measurement setup.....	37
Figure 2.12 Resonant frequency shift of the tunnel diode circuit at 120 K plotted against magnet current. The duration of the field scan is 1 hour.....	39
Figure 2.13 Frequency shift for the tunnel diode circuit for the empty coil and for the coil with sample.....	39
Figure 2.14 Transport experiments setup for Flux Transformer measurements.....	41
Figure 2.15 Block diagram of interfacing for transport measurements.....	42
Figure 3.1 Zero field cooled temperature scan of unirradiated Bi-2223 sample at zero field, 1 kG and 2 kG.....	46
Figure 3.2 The frequency shift $\delta f [= f (H, T) - f (0, T)]$ as the external dc magnetic field which is oriented perpendicular to the tape plane is cycled in the positive and negative directions.....	48
Figure 3.3 Variation of frequency shift δf as the external magnetic field oriented perpendicular to the plane of the tape is increased from zero to 3200 Gauss. Curves shown in the Figure have been obtained from frequency measurements done at 70, 72.5, 75, 77.5, 80, 82.5, 85, 87, 89, 91, 93, 95, 97, 99, 101 and 103K.....	49
Figure 3.4 (a) $(\delta f)^2$ Vs. H at 60 K and, (b); $(\delta f)^2$ Vs H at 80 K. The external dc magnetic field H , was perpendicular to the plane of the tape in both cases. The range of field over which a $(\delta f)^2 \sim H$ dependence is followed is shown and the critical fields H_1^* and H_2^* are marked (see text).....	50
Figure 3.5 The pinning force constant k_p^\perp deduced from δf data between field H_1^* and H_2^* is plotted as a function of temperature. The variation of H_1^* and H_2^* with	

temperature is shown in the inset. Solid lines through data points are guide to eye.....	52
Figure 3.6 Variation of frequency shift δf as the external field (oriented parallel to the plane of the tape) is increased from zero to 3200 Gauss. Temperatures of measurement are listed in the Figures.....	54
Figure 3.7 The pinning force constant k_p^{\parallel} deduced from the data of Fig. 3.6 is plotted as a function of temperature. Inset shows the range of field over which δf^2 shows a $\sim H_{dc}$ dependence at 80 K.....	55
Figure 3.8 Magnetic field dependence of the penetration depth measured at 85 K for different value of the angle (θ) between the dc field direction and the plane of the tape.....	57
Figure 3.9 Variation of $k_p^{\perp}/k_p(\theta)$ with $\sin \theta$ for measurements performed at 85, 95 and 99 K. Solid line in the Fig. is a guide to the eye.....	58
Figure 3.10 Frequency shift δf plotted as a function of temperature at zero field for the unirradiated, 0.5 T and 3 T irradiated samples. Inset shows broadening of the transition when 1 kG field is applied perpendicular to the plane of the 0.5 T irradiated sample and the unirradiated sample.....	60
Figure 3.11 (a, b) The normalized frequency shift $\delta f_n = (f(H,T) - f(0,T)) / (f(0,T_c) - f(0,10\text{ K}))$ Vs. the external dc magnetic field applied perpendicular to the plane of the platelet. The field is increased upto a maximum of 3.2 kG at various temperatures; a) 0.5 T irradiated sample b) 3 T irradiated sample..	61
Figure 3.12 (a, b, c) $\delta\lambda$ Vs. $\sqrt{H_{dc}}$ at 80 K for the a) unirradiated , b) 0.5 T irradiated and c) 3 T irradiated samples. The magnetic field, H_{dc} , is perpendicular to the plane of the platelet in all cases. The change in slope is marked by critical fields H_1^* and H_2^* (see text).....	63
Figure 3.13 (a, b) Field scans at various angles with respect to ab plane for the 0.5 T irradiated sample at a) 80 K and b) 90K.....	64
Figure 3.14 The pinning force constant k_p / G^2 deduced from $\delta\lambda$ Vs. $\sqrt{H_{dc}}$ data between field H_1^* and H_2^* is plotted as a function of reduced temperature for the unirradiated and two irradiated samples.....	66
Figure 3.15 The coefficient of viscosity η / G^2 is plotted Vs. Temperature.....	67

- Figure 4.1 Angular scans for unirradiated Bi-2223 showing superior pinning characteristics when the external field is parallel to the planes. The effect is most prominent at high temperature and strong fields.....72
- Figure 4.2 A comparison between Bi-2212 and Bi-2223. The temperature and external magnetic field are held constant at 70 K and 1.75 kG. A sharper peak at 0° and 180° for Bi-2212 shows that the peak width is essentially dependent on interlayer coupling.....72
- Figure 4.3 Angular scan of $\delta\lambda$ for the 0.5 T irradiated sample with $H_{dc} = 2$ kG at several temperature except at 95 K where $H_{dc} = 0.72$ kG. The dip at $\theta = 90^\circ$ marks anisotropic pinning due to columnar defects.....74
- Figure 4.4 Angular scan of $\delta\lambda$ for the 0.5 T irradiated sample at 80 K for several dc field values. The dip at $\theta = 90^\circ$ is not present at 100 G. Only at field greater than 500 G, strong pinning at defect sites is observed.....76
- Figure 4.5 Variation of accommodation angle with respect to temperature for the 0.5 T irradiated sample. The data reflects negligible misorientation between the platelets.....77
- Figure 4.6 (a-f) Angular scans of 3 T irradiated sample at different temperatures. The dc field is 1.750 kG for all the scans.....79
- Figure 4.7 Angular scan of 3 T irradiated sample at high temperature.....80
- Figure 5.1 The rf penetration depth $\delta\lambda$ Vs. H_{dc} for the unirradiated sample at several temperatures. The y - axis varies from 0 to 7150 Å ($\delta f = 3250$ Hz = n) for 25 K and 35 K data. The scans at 45 K, 72.5 K, 91 K and 103 K are scaled by 2n, 3n, 10n and 10n respectively.....85
- Figure 5.2 Anomalous behaviour of the hysteresis in the measurement of $\delta\lambda$ Vs. H_{dc} for the unirradiated sample. Data have been shown for both increasing and decreasing field sweeps for lower values of H_{max} and only the positive side for $H_{max} = 2$ kG and 2.7 kG. Direction of the magnetic field was perpendicular to the plane of the tape.....86
- Figure 5.3 The normalized rf penetration depth $(\delta\lambda)_n$ Vs. H_{dc} for (a) unirradiated, (b) 0.5 T irradiated and (c) 3 T irradiated sample at 15 K and H_{dc} perpendicular to the plane of tape.....88

- Figure 5.4 The hysteresis of the 3 T irradiated sample at several temperatures. The external field is perpendicular to tape plane. For all the plots y - axis varies from 0 to 5500 Å.....89
- Figure 5.5 Reverse branch of hysteresis for successive values of maximum external dc field. (a) unirradiated sample at 15 K, and (b), (c), and (d) for 3 T irradiated sample measured at 55, 45 and 30 K respectively.....90
- Figure 5.6 (a,b,c,d) A plot of local field current density in Bean Critical state model for different external field values. The Bean critical field H_g^* corresponds to flux penetration into the entire width of the sample. (a) local field gradients, (b) critical current density for constant external field. (c) and (d) represent the case when the external field is removed. The trapped flux gives rise to hysteresis.....94
- Figure 5.6 (e, f) (e) Examples of grain boundary (h_f) and grain pinned fluxon (h_p) in JRAT model in the ordered case. The cubes represent superconducting grains. (f) The flux profile in the two level critical state. The dotted lines enclose the grain boundaries.....94
- Figure 5.7 Variation of H_{mr} Vs H_{max} at different temperatures. Open symbols are for the unirradiated sample measured at 15 K, and closed symbols are for the 3 T irradiated sample. Inset shows the variation of J_{cg} with temperature for the unirradiated (\square) and 3 T irradiated sample (\blacklozenge). Dotted lines show fit of Eqs. 5.4 and 5.5 to 30 K and 45 K data respectively (see text).....96
- Figure 6.1a. Temperature dependence of the top and bottom voltages (V_T and V_B) as a function of external dc magnetic field for the unirradiated silver sheathed Bi-2223 tape. Solid symbols are for the top voltage and open symbols for bottom voltage. Magnetic fields from right to left are 0, 0.2, 1, 2, 5, and 8 kG. The inset shows transformer contact configuration for in plane resistive measurements.....101
- Figure 6.1b. Temperature dependence of bottom (V_B) and c-axis voltage (V_C) at external field 0, 1, 2, 5 and 8 kG (right to left). Notice the two step resistive transition and simultaneous occurrence of onset of c-axis resistivity and the

- decrease in bottom voltage. The inset shows contact configuration for c-axis resistive measurement.....102
- Figure 6.1c Temperature scan of top, bottom and c-axis voltage at 2 kG field applied parallel to C-axis. Onset of c-axis resistivity marks the decrease in bottom voltage. At high temperature the c-axis coupling is further weakened leading to a transition from line liquid to 2D liquid.....105
- Figure 6.2a In-field temperature scans for the irradiated sample with $B_\phi = 3$ T. The magnetic fields from right to left are 0, 0.075, 0.2, 0.5, 1, 2, 5, and 8 kG..106
- Figure 6.2b. The bottom (V_B) and c-axis (V_C) voltages for the irradiated sample. The shoulder at higher temperature with weaker c-axis correlation is not seen in this case. Also notice that unlike the unirradiated case, the peak of V_B initially increases with field and then attains a saturation value. The external magnetic field values are 0, 2, 5 and 8 kG from right to left.....107
- Figure 6.3 The measured (R_m), silver (R_{Ag}), and superconducting core (R_s) resistances as a function of temperature at 5 kG for the unirradiated sample. R_s is calculated assuming the measured resistance to be due to a parallel combination of 25 μm thick silver sheath and superconducting core of thickness 80 μm109
- Figure 6.4 The activation energy calculated from the slopes of Arrhenius plots for the unirradiated and 3 T irradiated samples. Inset shows linear fits in the high temperature regime for the irradiated sample. The slopes are calculated from top surface resistance $R_T (= V_T / I)$. Similar plots for V_C did not yield straight lines indicating to the fact that the loss mechanism is not thermally activated along c-axis.....111
- Figure 7.1 Frequency shift δf is plotted as a function of temperature at 0, 1 and 2.5 kG field applied perpendicular to the plane of the tape. Notice the large in-field broadening of inductive transition.....116
- Figure 7.2 The frequency shift δf as the external dc magnetic field which is oriented perpendicular to the tape plane is scanned upto a maximum field of 3.2 kG at various temperatures. The arrow marks the appearance of a shoulder in ac field penetration response in a particular field and temperature regime.....117

- Figure 7.3 The frequency shift δf Vs. H_{dc} when the field is applied parallel to the planes. The shoulder seen in perpendicular orientation is not seen here. Notice also the delayed saturation of ac field penetration as compared to the perpendicular configuration.....119
- Figure 7.4 δf Vs. $\sqrt{H_{dc}}$ at several temperatures for the field applied perpendicular to the tape plane. At field values less than the point where the shoulder appears, straight lines can be fitted to the data.....120
- Figure 7.5 The crossover field H_2^* plotted as a function of temperature. The solid line is a best fit for the melting transition. Also shown are experimental results of Zeldov et al. and van der Beek et al. (See text).....120
- Figure 7.6 The normalized pinning force constants calculated from slopes of δf Vs. $\sqrt{H_{dc}}$ curve is plotted as a function of temperature and is compared with available Bi-2212 single crystal and Bi-2223 data.....122
- Figure 7.7 Frequency shift δf as a function of angle at 50 K with external dc field of magnitude 0.5, 1 and 2 kG. Notice the sharp cusp in inductive response when the field is made parallel to the ab-plane of the sample. Here $\delta f = f(H, T, 0^\circ) - f(H, T, \theta)$123
- Figure 7.8 Field scans at various angles with respect to ab plane of the sample ($\theta = 0^\circ$ is the parallel to plane configuration) at $T = 40$ K. The inset shows low field regime. The critical value of applied field for vortex unlocking from the planes decreases with increasing angle.....125
- Figure 7.9 Field scans at different angles with respect to ab plane of the sample at $T = 60$ K.....126
- Figure 7.10 The data of Fig. 7.9 as a function of the c- axis component, $H \sin \theta$, of the external field. All the curves collapse into a narrow band for angle θ between 15° to 90° with respect to ab plane.....126
- Figure 7.11 Variation of inductive response as a function of $H / \beta(\theta)$ on a logarithmic scale at $T = 60$ K.....128
- Figure 7.12 Scaling parameter $\beta(\theta)$ as a function of $2\theta / \pi$ for Bi-2212 tape sample at $T = 60$ K. The dotted line is a scaling with $1 / \sin \theta$. The solid line is a best

fit to the anisotropic effective mass model (see text) and yields an anisotropy $\gamma = 10$ 128

Figure 7.13 Field scans at different temperature for 0.5 T irradiated Bi-2212 platelets. A reentrant behaviour is observed for $35 \text{ K} < T < 65 \text{ K}$. Right y-axis is scaled for 75 K and 85 K..... 129

Chapter 1

Introduction

The aim of this thesis is to gain more insight into the dynamics of vortices in technologically important silver sheathed bismuth based superconductors. In this preliminary chapter, a brief review of the relevant field of research is undertaken. The chapter begins with an introduction to vortices and vortex dynamics in superconductors and discusses the influence of intrinsic and extrinsic disorder on these properties. Since our experiments are primarily based on the use of a radio frequency (rf) technique, we have reviewed the literature on vortex dynamics at high frequency in homogeneous and granular superconductors, particularly the reported work on bismuth family of superconducting tapes. The chapter ends with a section on the motivation for this thesis work.

1.1 Vortices in superconductors and vortex dynamics

1.1.1 The vortex state

The copper oxide based high T_c superconductors are known to be extreme type - II superconductors. This means that there is a large mixed state region in the $H - T$ phase diagram where inhomogeneous field distribution inside the material co-exists with superconductivity [1]. For an external field stronger than the lower critical field H_{c1} , the field penetrates into the superconductor as an array of vortices. Each of these imaginary magnetic flux lines contains exactly one quantum of flux $\phi_0 = h / 2 e = 2.07 \times 10^{-15}$ Wb. The vortex core where the charge carriers are depaired electrons, extends upto superconducting coherence length ξ and is shielded by azimuthal supercurrents. The characteristic length λ , the penetration depth, defines the length scale over which the field decays exponentially into the superconductor. This vortex state or mixed state is dependent on material property and is achieved for superconductors with Ginzburg - Landau parameter $\kappa (= \lambda / \xi) > 1/\sqrt{2}$. In this limit, the surface tension at the interface between the normal and superconducting region is negative and the system decreases its energy by creating largest possible number of such interfaces.

For the conventional type - II superconductors the topography of vortex state is well described by the mean field hexagonal Abrikosov lattice structure [2]. As the field increases, the vortex density increases and at the field corresponding to the upper critical field H_{c2} , the normal cores entirely overlap with one another and drive the material into the normal state. The material parameters of the oxide superconductors, however, lead to a vortex state which is rich and complicated for many reasons. The layered perovskite structure and dominance of thermal fluctuations introduce new features to the thermodynamic phase diagram. A higher transition temperature, extremely small coherence length and anisotropic electric behavior lead to melting of the vortex lattice and creation of vortex liquid phases over a broad range of temperature and field [3]. These novel phases are further altered by introducing controlled disorder. The dynamical behaviour of such vortices and vortex phases is studied by subjecting them to the Lorentz force due to externally imposed static or oscillating currents. In this sense the vortex

state in high T_c materials provide experimental accessibility to the entire gamut of statistical mechanics of one dimensional interacting elastic strings.

At low temperatures, the mutual repulsion between the vortices leads to an ordered hexagonal lattice structure. The dominance of thermal fluctuations destroy this long range order at high temperature and for clean single crystals a first order transition separates the ordered vortex solid phase from the short range vortex liquid phase [4]. The liquid phase is further subdivided into disentangled, entangled and decoupled phases depending on material disorder and coupling energy between the superconducting planes and thermal fluctuations. Quantitatively, the dominance of thermal effects are parametrized in terms of Ginzburg number (Gi). While for conventional superconductors $Gi \sim 10^{-8}$, in extremely anisotropic $\text{Bi}_2\text{Sr}_2\text{CaCu}_2\text{O}_8$ crystals, $Gi \sim 10^{-1}$. Therefore for bismuth based (BiSCCO) superconductors, the line like nature of the vortices is less important and at the high temperature the vortices behave more like discs of circulating currents (so called pancakes) in the Cu-O planes which are coupled in the field directions through interplane Josephson coupling and magnetic interactions.

While the thermal effects lead to dynamical disorder in the vortex state, structural defects in the superconducting material are a source of static disorder. All real samples contain dislocations, stacking faults, point and surface defects to some extent. Defects, where the superconducting order parameter is either zero or greatly suppressed, are preferential sites for localizing vortices because this amounts to saving the condensation energy which would otherwise be lost in the vortex core. For a uniaxially anisotropic superconductor such as the high T_c cuprates, the energy saved on localization of a vortex in a spherical point defect of radius r ($\sim \sqrt{\xi_c \xi_{ab}}$) is given by $\sim (H_c^2 / 8\pi) \pi \xi_c \xi_{ab}^2$, where H_c is the thermodynamic critical field and ξ_c and ξ_{ab} are coherence lengths along directions perpendicular and parallel to ab plane respectively. In this sense defects act as pinning centers and the cumulative effect of all the defects in the material is quantified as the bulk pinning force. Due to random and statistical nature of the defects, the pinning centers destroy the long range order of the vortex lattice.

While the point defects are very effective in low T_c materials, it is not so in oxide superconductors due to extremely small coherence length. Further, the anisotropy leads

to suppression of line tension of vortices (by a factor ξ_{ab}^2 / ξ_c^2), and point defects do not provide effective localization to such flexible flux lines. A cylindrical defect of radius equal to the coherence length on the other hand provides optimum pinning across the thickness of the sample. The maximum core pinning energy per unit length of the vortex in this case is given by [5],

$$U_p \sim (H_c^2 / 8\pi) \pi \xi_{ab}^2 \text{ for } H \parallel c \quad (11)$$

$$U_p \sim (H_c^2 / 8\pi) \pi \xi_c \xi_{ab} \text{ for } H \perp c \quad (12)$$

Linear extended defects or columnar defects are conveniently introduced in the material by Heavy Ion Irradiation (HII) in particle accelerators. At an optimum energy such irradiation creates continuous amorphous tracks of radius ~ 7 nm [6]. A verity of heavy ions like Pb[7], I [8], Sn [9] and Au [10] with energies varying from 0.5 to 6 GeV have been used for this purpose. Liberating a vortex from such a linear defect requires considerable amount of force and therefore the current carrying properties over useful field range are significantly improved after HII. The strong pinning provided by columnar defects completely alters the equilibrium properties of a clean vortex state [3,11]. At low temperature the vortices freeze into a glassy phase characterized by a second order phase transition. Theoretically, the effects of columnar defect on mixed state properties have been described in the Bose glass model of Nelson and Vinokur [12]

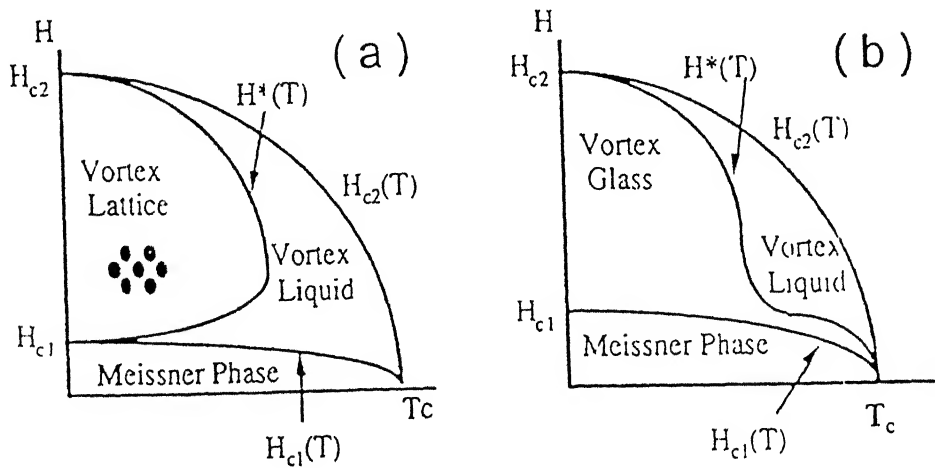


Figure 1.1 Equilibrium vortex phase diagram for a highly anisotropic high T_c superconductor with (a) weak random pinning, and (b) strong random pinning. (From Ref [11]).

1.1.2 Vortex dynamics

A single vortex line can be in the state of static equilibrium at any given position only if the net superfluid velocity due to all other sources is zero there. This is achieved for a symmetrical array of vortices and it turns out that only the triangular array is rigid against small perturbative displacements. Even the triangular array will face a transverse force under the influence of any external transport current unless the vortices are pinned by defects and inhomogeneities in the material. When the total force on the vortex due to the external current exceeds the force available from pinning, the vortices start moving in a direction perpendicular to both the external field and transport current. Due to the motion of the flux line, an electric field is induced in the direction of the transport current. This electric field sets up a current in the normal cores of the moving vortices and it turns out that its magnitude is exactly equal to that of the transport current driving the motion. Equivalently, the transport current flows right through the normal core producing dissipation. This is called Flux Flow and the dissipative fluxon motion is accounted by a viscous force $F_v = \eta v$ where η is the Bardeen - Stephen drag coefficient [13] given by $(\mu_0 H_{c2} \phi_0 / \rho_n)$. Here ρ_n is the normal state resistivity. Even in the absence of external current, thermal fluctuations render mobility to vortices leading to lossy vortex creep [14] and therefore in the superconducting state there is some finite loss at all temperatures above absolute zero.

1.1.2.1 Vortex dynamics at rf frequency

1.1.2.1a Homogeneous superconductors with pinning disorder

The theories of vortex motion are based on microscopic parameter of vortices such as pinning constant, coefficient of viscosity and Hall coefficient [15]. High frequency techniques are particularly suitable for the determination of these parameters because the measurements are carried out with negligible probe current leading to minimal perturbation and sample heating effects. In a dc measurement, if the vortex density is not large, the supercurrent can take a least resistance path to avoid the normal vortex cores.

Actually, vortex dynamics does not mean movement of quasiparticles in the core. What happens is that the Cooper pairs in the front side of the moving vortex are reconverted to quasiparticles and in the rear side quasiparticles are converted to Cooper pairs. In the high frequency measurements, because of finite relaxation time between the depairing and recombination processes, some energy is always lost in the process. In this sense the small probe current leads to enhanced dissipation, which would have otherwise occurred for either very high dc transport current or a large external magnetic field. There are two frequency regimes which are of particular interest. Above microwave frequency almost all effects of flux pinning fall away and one can study the ideal superclean mixed state even in the most strongly pinned materials. In the rf regime, on the other hand, the interaction between the flux line lattice and the pinning defects can be studied. Gittleman and Rosenblum [16] have argued that there is a characteristic frequency for each material which delineates the regime below which pinning is effective and above which only the viscous drag effects control the dynamics of flux lines.

The interaction with various defects in the crystal lattice leads to pinning of the vortices and the dynamics is approximated as small oscillations in a pinning potential U . If there are many pinning centers, the pinning potential is periodic in the flux line lattice constant d and is typically given by $U = (1 - \cos(2\pi x/d))$. The restoring force per unit length of the vortex, the Labush parameter, is given by $k_p = (d^2U/dx^2)_{x=0}$ in the rigid vortex limit. Since this early work of Gittleman and Rosenblum, models of the dynamics of vortices subjected to Lorentz forces of alternating screening currents have been refined considerably [17-20]. However, restricting ourselves to the simplest one-vortex picture, we can say that the Lorentz force of the induced surface currents makes the ends of the vortices oscillate with the currents. This motion is transmitted deeper into the sample by the stiffness of the flux line, and thus, more currents are induced in the volume of the sample. Flux pinning by defects, and viscous drag effects on a moving vortex inturn damp this oscillatory motion. Neglecting Hall and stochastic thermal force, the equation of motion of a single vortex in this framework can be written as ;

$$m \ddot{\mathbf{x}} + \eta \dot{\mathbf{x}} + k_p \mathbf{x} = \mathbf{J} \times \phi_0 \quad (1.3)$$

where \mathbf{x} is the instantaneous displacement of the vortex from its equilibrium position. The mass of the vortex is neglected [21] and assuming a linear response of the system and a periodic pinning potential, the net complex penetration depth λ of rf currents can be written as [19];

$$\lambda = [(\lambda_L^2 - (i/2) (\lambda_v)^2) / (1 + i (2 \lambda_L^2 / \delta_{nf}^2))]^{1/2} \quad (1.4)$$

$$\lambda_v = (\lambda_f^{-2} - (\frac{i}{2}) \lambda_c^{-2})^{-1/2} \quad (1.5)$$

where λ_L is the London penetration depth, $\lambda_c^2 = B\phi_0 / \mu_0 k_p$ defines the Campbell penetration depth, $\lambda_f^2 = 2B\phi_0 / \mu_0 \eta \omega$ is the flux flow penetration depth and δ_{nf} represents the normal fluid skin depth. Here ϕ_0 , μ_0 , ω , k_p and η are respectively the flux quantum, permeability of free space, the resonant frequency, pinning force constant and flux flow viscosity. In the mixed state of the superconductor, the depairing contribution to the change in penetration depth ($\delta\lambda$) is dominated overwhelmingly by the vortex contribution. Further, in the rf regime, the normal fluid skin depth is appreciable only very close to T_c . One can therefore, neglect the contributions to rf penetration depth from depairing effects and normal fluid skin depth at low fields, and correlate the measured $\delta\lambda$ to the vortex contribution given in Eq. 1.5. For $k_p \gg \eta$, the above expression reduces to the Campbell penetration depth with a characteristic \sqrt{B} dependence for λ . The \sqrt{B} dependence follows even in the flux flow regime where the vortices essentially ignore the pinning potential and the penetration depth becomes the flux flow skin depth. Above a certain temperature dependent field $H^* (T)$, a transition from pinning to flow regime is expected. The above derivation does not take into account Thermally Activated Flux Flow (TAFF) effects. The TAFF processes would make the transition from pinning to flow dominated region less defined.

Depending on the vortex concentration and defect density, there are two main pinning regimes. At low fields when there are few vortices and many pinning sites, individual pinning is realized and the pinning constant is field independent. At high fields there are many vortices per defect site, the pinning is collective and the pinning constant is smaller and field dependent. The pinning constant k_p reflects the interaction of

single vortex with the defect site in the individual regime and statistical summation of the vortex-defect interaction in the collective regime.

1.1.2.1b RF vortex dynamics in granular superconductors

The high frequency magneto-impedance measurements on Type - II superconductors show hysteretic effects due to pinning and granularity [22-26]. While in single crystal samples the field increasing branch of absorption lies above the field decreasing branch, in inhomogeneous superconductors, absorption is less during field reversal. The detailed shape of this inverted (anomalous) hysteresis depends on granularity, maximum field traversed, surface imperfections and geometry of the sample. In the low-temperature, low-field, radio frequency regime when the pinning centers are active in grains, the observed dissipation is due to the motion of intergranular vortices. The coefficient of viscosity in the grains is orders of magnitude greater than the viscosity in intergrain region. This is the basis for the two level critical state model developed by Ji, Rzechowski, Anand and Tinkham (JRAT) to explain magneto-absorption in granular YBCO samples [25]. On the other hand, a theory based on gradual decoupling of Josephson coupled grains due to external field above a certain characteristic temperature also leads to the inverted hysteresis in rf absorption, which is dependent on strength and density of Josephson Junctions [26]. The measurements in ceramic samples show that high frequency techniques can be powerful tools to probe the extent of granularity in a nominally clean superconductor [27-29].

1.2 Bi-2223 and Bi-2212 superconducting tapes

1.2.1 Structure and physical properties

Since the discovery of superconductivity at ~ 35 K in $\text{La}_{1-x}\text{Ba}_x\text{CuO}_4$ compound by Bednorz and Müller, unprecedented efforts have been made globally to synthesize new cuprate superconductors of higher and higher critical temperature. For technological application to be possible at liquid nitrogen temperature, it was necessary to have a

superconductor that would allow flow of large dissipation - less currents in moderate to high magnetic fields at this temperature. The material must also have necessary metallurgical characteristics for formability. Although some Tl and Hg based cuprates of T_c between 115 - 135 K have been synthesized successfully, the technological potential of these compounds is limited due to their toxicity and stringent synthesis conditions. The ~ 92 K T_c compound $YBa_2Cu_3O_7$ or the bismuth family of cuprates, on the other hand, have shown considerable promise. The bismuth based compounds are particularly suitable for heavy engineering applications because of their layered structure which allows a rapid platelet type growth in the ab-plane. This characteristic has been utilized to synthesize kilometer long multifilamentary silver sheathed tapes of these superconductors. This technology is considered mature for intracity power transmission applications. The performance of these superconductors at 77 K even in moderate fields is however, poor. Their ability to carry large lossless current drop precipitously on application of a magnetic field. The objective of this thesis is to understand the physical process responsible for the onset of dissipation in silver sheathed composite conductors of Bi-cuprates.

The general formula for Bismuth based high temperature superconducting compounds is $Bi_2Sr_2Ca_{n-1}Cu_nO_{4+2n}$, $1 \leq n \leq 3$. The crystal structure is the body centered tetragonal but usually a slight orthorhombic distortion is also found. Like all other high T_c materials, the BiSCCO superconductors also exhibit layered structure and concomitant anisotropy. The crystals consist of n adjacent Cu-O planes (for $n \geq 2$), each separated by a plane of Ca atoms. Two sets of adjacent Cu-O planes are separated by a Sr-O plane, two Bi-O planes and another Sr-O plane. Both from theoretical and experimental grounds, it is understood that superconductivity and charge transport is essentially confined to the Cu-O planes. The schematic diagrams of $Bi_2Sr_2Ca_2Cu_3O_{10}$ (Bi-2223) and $Bi_2Sr_2CaCu_2O_8$ (Bi-2212) are shown in Fig. 1.2.

The large distance $\sim 15\text{\AA}$ between the adjacent copper oxide planes leads to highly anisotropic superconducting behaviour. The anisotropy is quantified in terms of a dimensionless parameter $\gamma = (m_c / m_{ab})^{1/2}$, where m_c and m_{ab} are Ginzburg - Landau

effective mass of carriers for motion perpendicular and parallel to the copper oxide planes respectively.

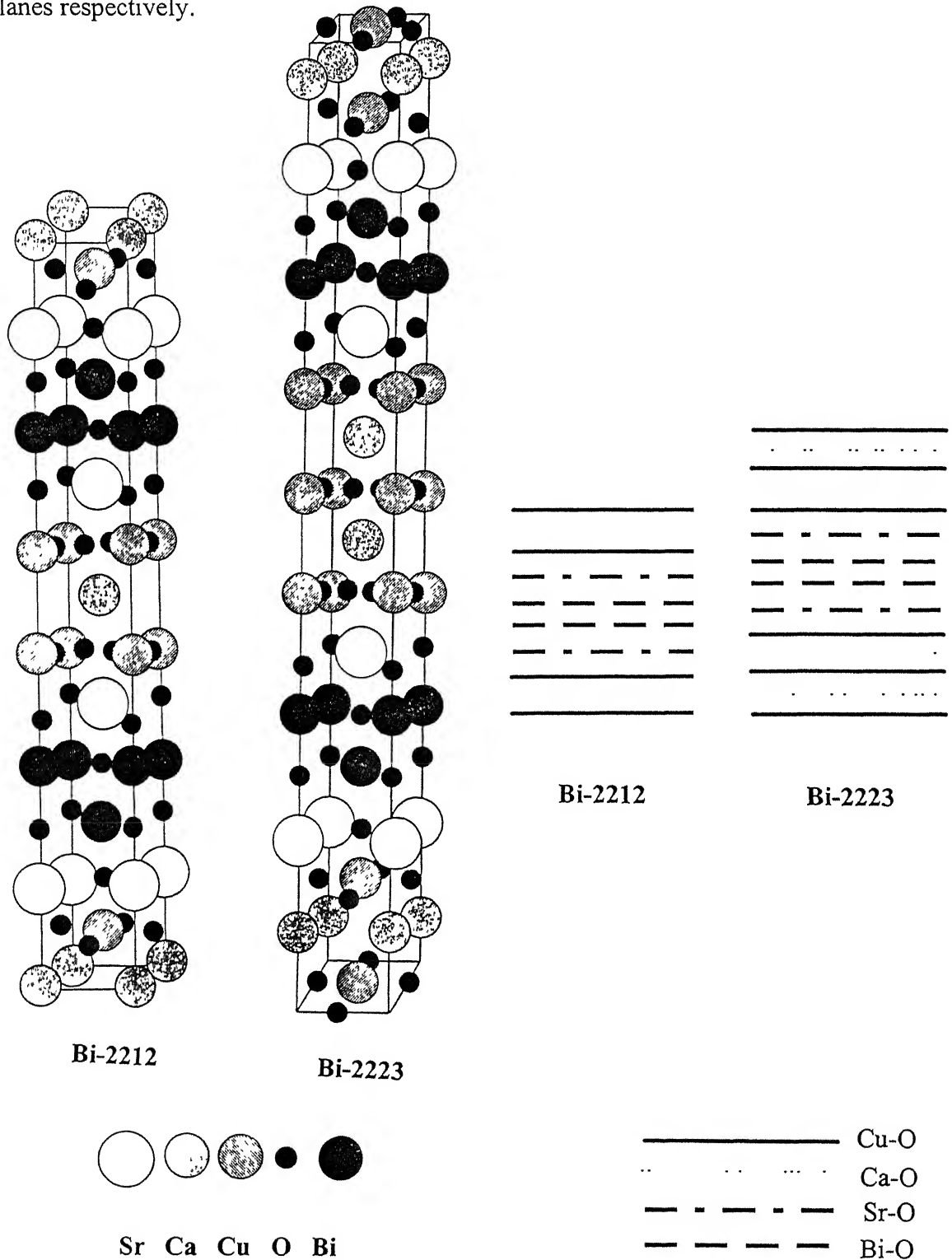


Figure 1.2 Crystal Structure of Bi-2212 and Bi-2223. The schematic representation of the layered structure is also shown.

The fundamental superconducting parameters in the two directions are related to mass anisotropy in the following manner.

$$\gamma = \left(\frac{m_c}{m_{ab}} \right)^{1/2} = \frac{\lambda_c}{\lambda_{ab}} = \frac{\xi_{ab}}{\xi_c} = \frac{H_{c2||ab}}{H_{c2||c}} = \frac{H_{c1||c}}{H_{c1||ab}} \quad (1.6)$$

The topology of the vortex state is altered profoundly by this anisotropy. While for moderate anisotropy, vortices can be considered as three dimensional objects and a 3D anisotropic Ginzburg - Landau Theory [30] is applicable, for the highly layered case, the Lawrence - Doniach model [31] is more appropriate. The vortices in highly anisotropic high T_c superconductors such as Bi-2212 can be modeled as 2 - Dimensional pancakes connected via Josephson coupling between the layers and magnetic interactions [32,33]. Due to the anisotropy, the field applied parallel to ab-plane and perpendicular to ab plane of the sample yield entirely different vortex characteristics. For external field applied parallel to the planes, the vortices do not have normal core; They reside between the sets of copper oxide layers where the superconducting order parameter is greatly suppressed and hence the loss of condensation energy due to field penetration is minimal [34]. A schematic diagram of a vortex along **a** axis (parallel to ab-plane) in an anisotropic superconductor is shown in Fig. 1.3. Many interesting physical phenomena like a 2D to 3D crossover [35] and lock - in transition [36] are a direct consequence of the structural anisotropy.

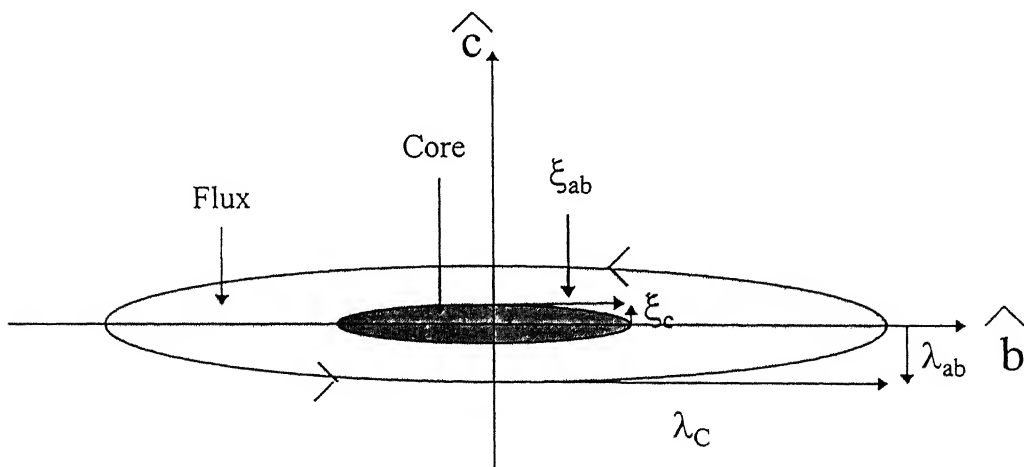


Figure 1.3 Single vortex in an anisotropic superconductor when the field is applied parallel to the sample plane. (from Ref .[34]).

In addition to these features of the mixed state related to crystallographic structure and electronic anisotropy of Bi - cuprates, the current transport in silver sheathed tape samples is further limited by the microstructure. Understanding the microstructure is critical from the technological application point of view. It has been established that the structural units of the tape samples are well aligned platelet shaped grains of length $\sim 20\mu\text{m}$ and width $\sim 1\mu\text{m}$ [37]. These platelets grow predominantly parallel to the silver sheath and are stacked on top of each other, separated by c-axis grain boundaries. Similarly, ab-axis grain boundaries separate the grains at the sidewise interfaces. Because of the thermomechanical processing techniques, various kinds of defects such as secondary phases, oxygen vacancies and incompletely reacted phases have also been observed in the tape samples. The grain boundaries and the defects have Josephson character, and behave as weak links. This means that the supercurrent undergoes an exponential attenuation while passing through a weak link. The magnitude of this attenuation is proportional to the barrier thickness and inversely proportional to the coherence length. Theoretically, the characteristic granularity in BiSCCO tapes have been represented in terms of the “Brick wall model”, where it is assumed that the tape is made up of brick like platelets of unequal size and shape [37,38]. The main idea behind the model is a network of Josephson junctions where the macroscopic supercurrent flows in an interconnected array. The grains and grain boundaries have many different sizes and correspondingly the weak links have various limiting currents. Studies by Bulaevskii et al. show that only a small well connected fraction of the grains which are found close to the silver - BiSSCO interface is responsible for providing high critical current densities. The results from magneto - optical imaging of Bi-2223 tapes also indicate that the effective current carrying cross-section is much smaller compared to the geometrical cross-section and the current flows in a complicated percolative path [39]. Several possibilities including columnar defects and increasing the well aligned grain volume fraction are suggested to improve critical current density in tape samples.

1.2.2 Vortex dynamics in bismuth family of superconducting tapes

Unlike the case of Bi-2212 single crystals, the dynamics of the superconducting mixed state in Bi-2223 phase has been investigated rather scantily due to the unavailability of large single crystals. The studies done todate on Bi-2223 have been limited primarily to measurements of dc magnetization, low frequency power loss and dc critical current density of well oriented platelets [40-43] and oriented thin films [44,45]. Early magnetization experiments on Bi-2223 composite superconductors were carried out by Li et al and these studies established the dominance of thermal fluctuations and determined many of the fundamental parameters for this system [46]. Flux pinning aspects in Bi-2223 tapes have been studied by many workers. While the data for magnetization which scales with the size of the platelets [37,40,41] suggest that the flow of screening currents is not inhibited by the ubiquitous grain boundaries and weak links in the sample, dc current flow patterns [39] and field dependence of J_c do suggest a microstructure limited supercurrent transport. The pinning force density and irreversibility fields in Bi-2223 tapes at various temperature and magnetic field strength have also been calculated [41,47]. It has been suggested that despite the structural anisotropy, the pinning mechanism for field applied perpendicular to the planes and for parallel to the planes is essentially the same. The focus on Bi-2212 tapes on the other hand has been confined to fabrication techniques to enhance critical current density [48]. A comparative study by Shibutani et al. on Bi-2212 and Bi-2223 tapes shows that alignment of grains and volume fraction of well aligned grains in Bi-2212 tapes is greater than the Bi-2223 tapes [49].

Two reports of transport measurement on Bi-2223 tapes using a Flux Transformer (FT) geometry are available in the literature. Cho et al. determine the anisotropy in resistivity for current transport along c-axis and perpendicular to it (ρ_c / ρ_{ab}) ~ 10 from the FT measurements [50]. Similar studies by Sun et al. show an anomalous broad peak in the bottom voltage which is assigned to a decoupling transition and a resistivity anisotropy between $10^2 - 10^3$ [51]. The four probe transport measurements, of Li et al.

[52] suggest that for fields smaller than 1.2 T, the onset of dissipation in Bi-2223 is well represented by a vortex glass to vortex liquid phase transition.

As discussed earlier, the layered structure of high T_c superconductors results in modulation of superconducting order parameter along the c-axis of the sample, and it is maximum in the copper oxide layers and minimum in other layers. The copper oxide planes therefore act as potential barrier to vortex motion and provide intrinsic pinning against vortex dynamics. The strong pinning due to columnar defects alters the scenario by enhancing pinning in the direction parallel to latent tracks. These features have been studied in detail for YBCO and Bi-2212 single crystals. The research with regard to heavy ion irradiation induced defects in BiSCCO / Ag tapes is focussed in two directions; i) enhancement in critical current density and ii) study of localization of vortices at the defect sites in these anisotropic superconductors. Transport measurement by Neumüller et al. showed an order of magnitude increase in J_c at low temperatures after irradiation with 0.6 GeV Ni ions [53] while magnetization measurement by Civalé et al. show significant enlargements of the irreversible region (~ 25 K for $B \leq 2$ T) after HII [54]. The angular dependence of pinning in 2.65 GeV lead ions has been carried out by Kummeth et al. [55]. Their studies show that enhancement in pinning is isotropic at low temperatures and there is a crossover to directional pinning at high temperatures. For $T \geq 60$ K cusp like features in $J_c(\theta)$ plots are observed centered around the track direction. These results indicate that vortices in irradiated crystals are not entirely decoupled. The directionality of pinning in Bi-2223 tapes has been studied by Fukumoto et al. as well. The angular dependence on 5.8 GeV lead ions irradiated Bi-2223 tapes was measured on standard four probe transport measurement [56]. Cusp like features were observed in angular scans of J_c for $T > 55$ K and 2D scaling was not observed. At lower temperatures ($T < 27$ K) neither the cusp nor the 2D scaling was observed and based on these results the authors concluded that the vortices have a line like character in HII Bi-2223 tapes. The absence of directional effects at low temperatures was assigned to increased coupling between the layers and the pinning at the uncorrelated defects created during irradiation. Studies of pinning effects in unirradiated and irradiated Bi-2212 tapes with linear and point defects have been carried out by Kazumata et al. [57] and the superior pinning ability of columnar defects over point defects at all temperatures was

verified. Further, the angular dependence of irreversibility field (H_{irr}) at 55 K showed a clear indication of unidirectional pinning.

1.3 Motivation for the present work

The above discussion has broadly outlined the scope of the present thesis. The studies of pinning due to growth related and irradiation induced defects in Bi - family of cuprates is of considerable technological importance in view of the recent successes in fabrication of silver sheathed multifilamentary tapes, and the possibility of incorporating linear defects not by irradiation but through less expensive metallurgical routes [58]. Furthermore it has not been possible to synthesize single crystals of meaningful size of Bi-2223 phase. The well oriented tapes are the best systems to undertake fundamental studies of vortex dynamics in this high T_c compound. The specific aspects of mixed state of Bi-2223 and Bi-2212 tapes probed in this thesis are;

- i) To estimate pinning force constants and flux flow coefficients in as grown and heavy ion irradiated Bi-2223 tapes:

The tremendous technological potential notwithstanding, pinning and flux flow parameters of BiSCCO tapes, particularly with columnar defects are still poorly defined. This is primarily because the high frequency techniques are not adaptable to tape samples due to contribution from silver sheath. By a unique chemical treatment we have removed the silver sheath from the surface and there by ascertained the intrinsic pinning parameters of Bi-2223 and Bi-2212 platelets. Further, the effects of grain boundaries and heavy ion irradiation on the pinning ability and flux flow properties of these materials are studied in detail.

- ii) To understand and estimate the temperature and field range of anisotropic pinning in heavy ion irradiated Bi-2223 superconductor.

Measurements of the angular dependence of pinning in HII single crystal / thin films of YBCO, Bi-2212 and Tl-2223 have indicated that directional pinning depends on the degree of anisotropy in the superconductor. The Bi-2223 cuprate provides an interesting system because, (a) it is less anisotropic as compared to Bi - 2212 and (b)

the T_c of this material is higher by $\simeq 20$ K which allows studies over a much wider dynamical range. This enables a detailed study to address the relative strength of pancake - pancake and pancake - columnar defects interaction in this quasi two dimensional superconductor.

iii) To evaluate the effect of grain boundaries in dictating the history effects in BiSCCO tapes

The current carrying capability of BiSCCO tapes is critically linked to the characteristic brick wall type granularity. In particular, hysteretic effects at low temperature are influenced by strong intragrain pinning and Josephson character of the weak links. Clearly, the macroscopic granularity in the tape samples makes the description of magnetization in terms of standard Bean model inadequate. It is also of interest to know how the hysteretic behaviour alters when the pinning potential in the grains is enhanced by heavy ion irradiation.

iv) To ascertain various vortex phases and activation energies in unirradiated and heavy ion irradiated Bi-2223 superconductor.

Transport measurement in the six terminal Flux Transformer geometry is a powerful means to study c-axis correlation, vortex dimensionality and entanglement under thermal fluctuations in a verity of superconductors. There have been reports on the existence of two vortex liquid regimes in twinned YBCO and heavy ion irradiated Bi-2212 single crystals. Such measurements are desired for the Bi-2223 phase as well.

v) To compare the results of Bi-2223 with more anisotropic Bi-2212.

Finally, the data from the experiments on Bi-2223 are compared with the measurements on more anisotropic Bi-2212 tapes. Moreover, since the vortex dynamics in Bi-2212 single crystals has been studied extensively, it is interesting to compare these results with measurements on tape samples to highlight the granularity and extent of anisotropy in Bi-2212 tapes.

Chapter 2

Experimental details

2.1 Introduction

The design, fabrication and performance aspects of the two experimental techniques used in this thesis are presented. The techniques are; a tunnel diode oscillator circuit for measurements of the rf penetration depth and a six probe setup for the dc transport studies in the flux transformer geometry. The measurements are carried out on five different sets of samples. All the instrumentation and interfacing of the experiments reported in the present study are designed and developed during the thesis work. The penetration depth which defines the length scale over which magnetic fields and current vary, is an important parameter of a superconductor. In the Meissner state for example, a knowledge of λ and its temperature dependence provide fundamental information about the strength and type of superconducting coupling, while in the mixed state it sets the length scale for vortex dynamics and vortex-defect interactions. The effectiveness of ac susceptibility techniques to measure temperature dependent change of penetration depth

was first experimentally established by Laurmann and Sohenberg [59]. But the advantages of radio frequency measurements, where the contribution from normal electrons can be neglected, were first shown by Schawlow and Devlin and their experiment verified many aspects of the BCS model [60]. The advent of high T_c superconductor with relatively larger penetration depth and unknown superconducting coupling, brought a revival of interest in high frequency $\lambda(H, T)$ measurements [61,62]. In the microwave range, the surface impedance measurements yield the superconducting penetration depth and quite generally various kinds of resonators or bolometric techniques are used. In the rf range however, LC resonators are used instead of a cavity.

The original Flux Transformer experiment on the other hand, conducted by Giaever used two superconducting tin films separated by a thin insulating SiO_2 layer [63]. The current was passed through one of the film (primary) and the resulting voltage drop across both the top and bottom (secondary) films were measured. A voltage in the secondary of the same magnitude as that of the primary, confirmed the vortex movement induced dissipation in the flux flow regime. Due to anisotropy, and layered structure, the vortices in high T_c superconductors in the liquid state do not always behave as elastic rods piercing through the entire thickness of the samples. Therefore, the voltage drops across the top and bottom contacts can be effectively used to understand the correlation of vortex along the c-axis and the anisotropic current flow in the layered systems.

2.2 The samples, controlled defect generation and microstructure study

The high quality c-axis oriented Bi-2223 tapes were prepared at Brookhaven National Laboratory using standard powder in tube (PIT) method [64]. The x-ray diffraction measurements of these samples revealed highly c-axis oriented growth with $< \pm 10^\circ$ variation along the ab plane. Similarly processed tapes exhibited J_c values as high as $30000 \text{ A} / \text{cm}^2$ at 77 K in self field. The main steps for the processing of PIT BiSCCO tapes are shown in Fig. 2.1. A homogeneous fine powder of Bi-2223 phase is prepared

by spray pyrolysis technique. A submicron order particle size mixture is produced in this way and this method is very promising from the industrial application point of view because it is a continuous process. The critical current density J_c of these tapes is crucially linked to many microstructural factors such as volume fraction of Bi-2223 phase, orientation of the platelets, density and type of secondary phases. The Bi-2212 tapes used in this study were prepared at Intermagnetic General Company (IGC), New York using a dip technique. The process leads to the formation of a c-axis oriented thick film ($\sim 25 \mu\text{m}$) of Bi-2212 on both faces of a $\sim 50 \mu\text{m}$ thick, 6mm wide silver tape[65].

Two sets of Bi-2223 and Bi-2212 tapes were irradiated with 6 GeV lead ions at the fluence of 1.5×10^{11} ions / cm^2 and 0.25×10^{11} ions / cm^2 at Grand Accélérateur National d'Ions Lourds (GANIL, Cern, France). The defects are created parallel to c-axis of the samples. The structure and density of defects through irradiation is dependent on a verity of factors such as a) rate of energy loss in the medium, b) thermal conductivity and chemical state of the medium, c) crystallographic orientation with respect to incident beam, and d) the density of preexisting defects in the material [6]. The energy transfer from the projectile to the sample material takes via two different processes; an electronic loss mechanism and a nuclear loss mechanism. The former process leads to excitation or ionization of target atoms and leads to localized melting and formation of amorphised tracks if the energy deposition rate is high. The later contributes to direct deformations of target atoms at the normal lattice sites and leads to vacancies in the material.

It has been established that electrons, neutrons, and light ions produce point defects and clusters. Point defects produce weak pinning force and are not effective for high temperature superconductors in a temperature range where thermal fluctuations are important. High energy heavy ions on the other hand produce columnar defects. The necessary condition for the formation of these defects is that the energy loss rate in the material should be above a threshold value.

1. Raw materials : The metal nitrates of bismuth, strontium, calcium and copper. Substitution of Pb in place of Bi enhances reaction diffusion and leads to stabilization of Bi-2223 phase.

2. An aqueous solution is prepared by dissolving stoichiometric amounts of metal nitrates in ultrapure water which contains nitric acid (5 %).

4 The furnace is maintained at $\sim 800^{\circ}\text{C}$ and the solution is thus thermally decomposed. The powder produced are collected using an electrostatic precipitator which is kept at $\sim 150^{\circ}\text{C}$.

3. The solution is sprayed using an ultrasonic nebuliser. The droplets thus generated are lead to a reaction furnace with a carrier gas (mixture of nitrogen and oxygen)

5. The submicron order homogeneous powder is packed into silver tubes. The tubes act as a mechanical and thermal stabilizer. Silver is chosen because it does not react with oxygen and oxygen can diffuse through Silver (oxygen is the key element for high T_c superconductivity).

6. The silver rods with calcined powders inside are elongated by applying force homogeneously in all direction of the composite. This process is called drawing

8. Heat treatment : At $820^{\circ}\text{C} - 840^{\circ}\text{C}$ in air or reduced oxygen to form Bi-2223 phase.

7. The wire is rolled to 0.1 to 0.2 mm thickness. Important step for achieving high J_c

Repeat

9. Pressing and Rolling : The volume fraction of Bi-2223 is increased by intermediate pressing and rolling. Crystal alignment and connection between the grains is improved.

10. Final Heat treatment

Figure 2.1 Main steps for the preparation of the PIT BiSCCO tapes using spray pyrolysis technique.

For BiSCCO it is of the order of ~ 20 keV / nm. With lead ions, the stopping power of Bi-2223 is approximately of the same order and the large ionization energy ~ 6 GeV ensures linear tracks of amorphised material across the width (~ 130 μm) of the tape. The general feature of the defects is a cylinder of amorphised material of diameter ~ 70 to 80 Å. A convenient way of characterizing the aerial density of defects is in terms of the density of vortices in the Abrikosov lattice given by B_ϕ ($= \phi_0 \times \text{fluence}$). The irradiation fluence in our case in this scale corresponds to 3 T and 0.5 T.

For the rf measurements, the silver is removed by using a 20 % solution of Hydrogen Peroxide with Ammonium Hydroxide as an etchant. This does not affect the superconducting material. This was confirmed through Electron Probe Micro Analysis and Electron Dispersive X - ray Analysis done on an etched sample. In Fig. 2.2 we show the results of EDX done on a Bi-2212 sample after the chemical treatment. We could observe some contribution from impurities like carbon, but silver is effectively removed from the surface. Therefore we have neglected the contribution from silver during rf measurements. After removal of silver, the platelets of Bi-2223 are cut into the size of $\sim 1.8 \times 1.8 \times 0.08$ mm³. Four layers of bare BiSCCO platelets were glued on top of each other on a $\sim 2.2 \times 4$ mm² sapphire plate using GE varnish, which is then attached to a teflon sample holder. The thickness of Bi-2212 platelets was ~ 25 μm and six layers were used for rf measurements. Figures 2.3a and 2.3b show X - ray analysis on Bi-2223 and Bi-2212 platelets respectively. The bottom silver sheath was not removed in these samples. The possible impurity phases are marked in the Figures. The sharp peaks corresponding to (001) planes reflect the excellent c-axis orientation of the platelets. These studies are carried out on a Rich & Seifert ISO DEBEYFLEX 2002 X - ray powder diffractometer with a copper K_α source. Figures 2.4a and 2.4b show the SEM photographs of Bi-2223 and Bi-2212 tapes respectively. The micrographs are taken on a JOEL JSM 840 A Scanning Electron Microscope. The granularity and platelet type of growth in these tape samples is evident from these Figures. The dc flux transformer studies are done only on Bi-2223 tapes and the silver sheath is not removed considering the excellent contact between the sheath and the superconductor [51]. The typical sample size in these measurements is $\sim 6 \times 1.5 \times 0.13$ mm³ with approximately 25 μm silver sheath on both sides.

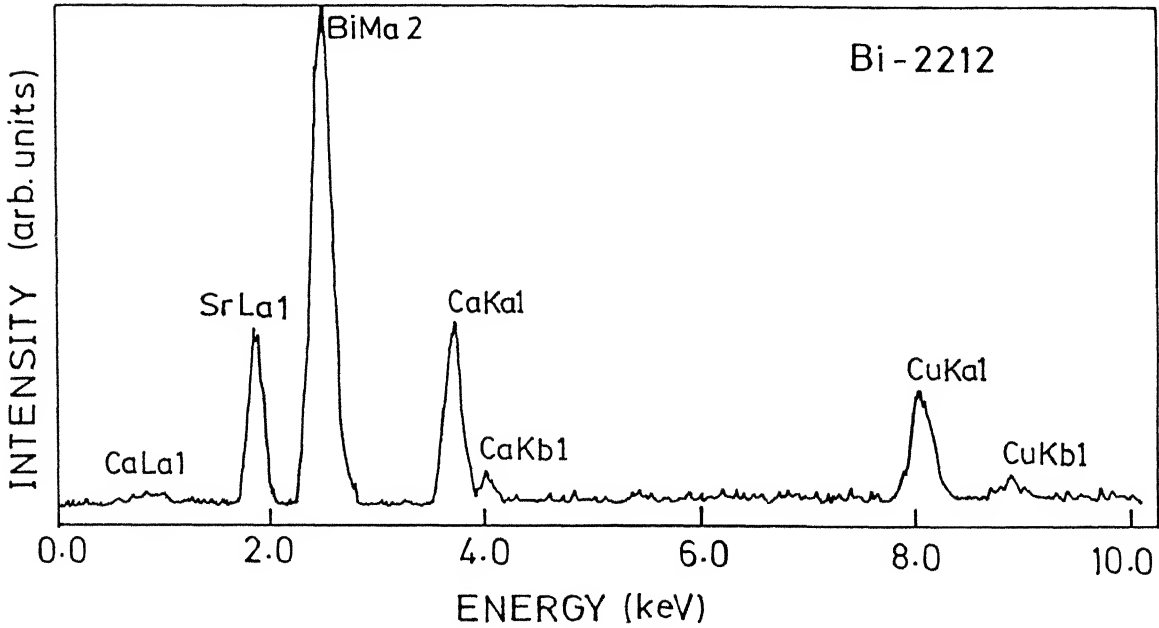


Figure 2.2 EDX study on a Bi-2212 sample after removing the silver sheath by chemical treatment.

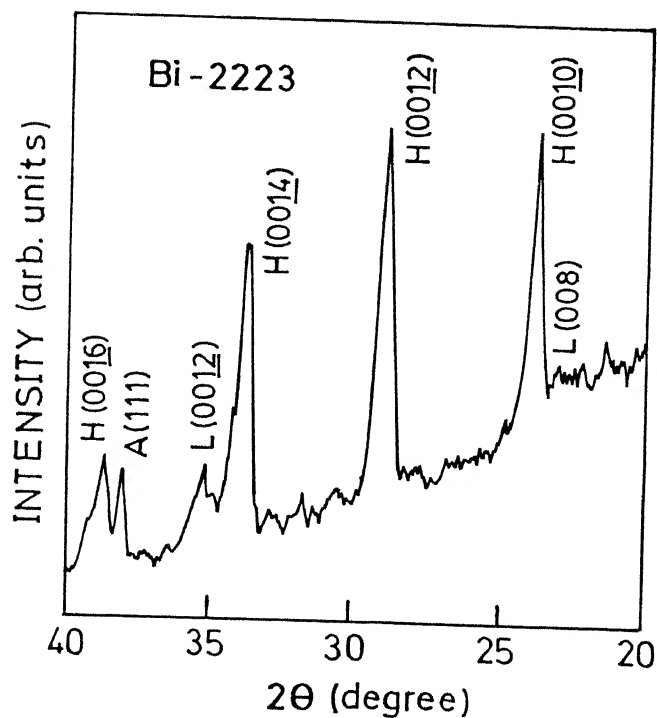


Figure 2.3a X - ray diffraction studies on a Bi-2223 platelet H, L and A stand for Bi-2223, Bi-2212 and silver respectively

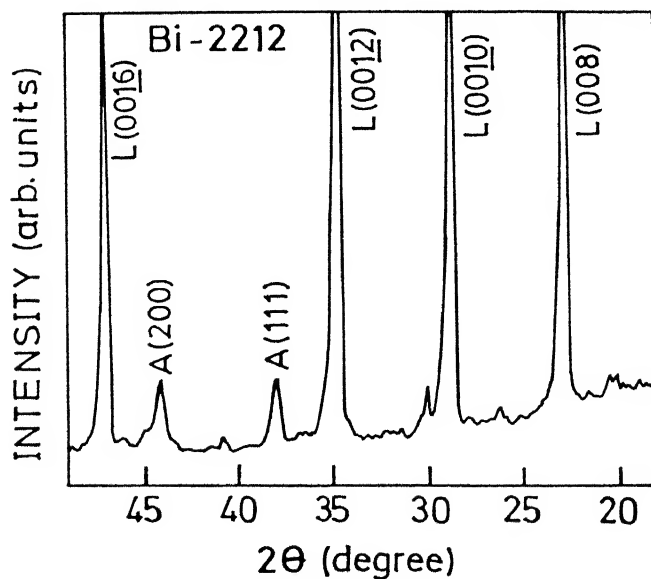


Figure 2.3b X - ray diffraction studies on a Bi-2212 platelet. L and A stand for Bi-2212 and silver respectively



Figure 2 4a A SEM micrograph of Bi-2223 sample.

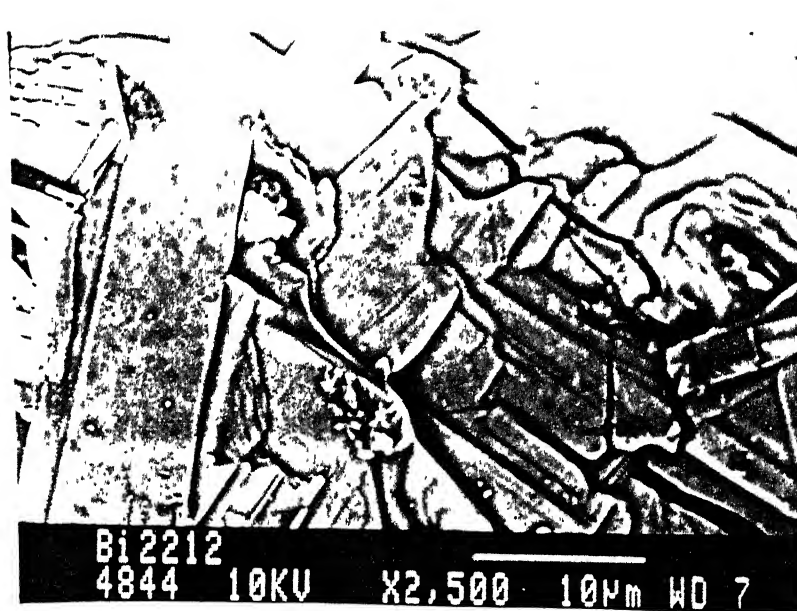


Fig. 2.4b A SEM micrograph of Bi-2212 sample.

2.3 RF Penetration depth measurement

2.3.1 The Technique

The method we have used is based on a LC resonator circuit. It involves placing the sample in a coil which is part of the LC circuit of resonant frequency f in the rf range and measuring the shift of f to detect changes in sample susceptibility. Operation at low rf field H_f and hence small induced currents J_f ensures small perturbation and hence linear theories of vortex dynamics can be applied. Techniques based on this general principle have been used previously to measure superconducting transition and mixed state properties of low T_c [20,60,66] and high T_c superconductors [15,62,67].

The underlying principle of measurement is the fact that the inductance L of a solenoid is proportional to the area offered to the flux to pass through it. In the Meissner state when $H < H_{c1}$ and a complete flux expulsion from the sample occurs, this area is the least. The area increases as the critical temperature is approached due to weakening of the Meissner screening. For an ultrastable oscillator, this would imply a shift in the resonant frequency of the LC circuit and this can be measured by an equally stable frequency counter. As has been analyzed by Schawlow and Devlin, the basic expression for the change in inductance is given as;

$$dL / L = (2 w d\lambda + 2 b d\lambda) / A \quad (2.1)$$

Here dL is the change in inductance caused by $d\lambda$ effective change in penetration depth and b and w are width and thickness of the sample respectively. A is the total area containing the flux i.e. $\pi R^2 - \pi R_{\text{eff}}^2$, R and R_{eff} being effective coil radius and radius of flux exclusion region respectively (See Fig. 2.5). For an anisotropic superconductor the London penetration depths are unequal and are represented by λ_{ab} and λ_c along ab plane and c - axis respectively. Clearly,

$$\pi R_{\text{eff}}^2 = b w - (2 \lambda_{ab} w + 2 \lambda_c b) \quad (2.2)$$

An external magnetic field $H > H_{c1}$, induces spatially inhomogeneous excitations which allow penetration of the external field in the form of flux lines. The Lorentz force of the induced rf screening current causes vortices near the surface of the sample to oscillate. These oscillations are transmitted deeper into the sample by the elasticity to the flux line lattice, thereby increasing the effective penetration depth. Flux pinning by defects and viscous drag on a moving vortex in turn damp this oscillatory motion. The situation is discussed in Fig. 2.6, with the dc and ac field perpendicular to each other; this corresponds to all the experiment in the mixed state described in this thesis. Pinning constant and coefficient of viscosity are derived from the Campbell and flux flow expressions relating rf penetration depth with external field. The derivations assumes single vortex pinning regime where vortex - pin interaction dominates the response. At high fields, vortex-vortex interaction dominates and the response becomes collective. The corresponding Campbell penetration depth at various field regimes has been derived by Koshelev and Vinokur[68].

When dc field is applied perpendicular to the ac field, the increased ac field penetration is primarily along c-axis and therefore we can write $dL / L = (2 \pi R_{\text{eff}} d\lambda) / A$. Using the relationship $4 \pi^2 f^2 = 1 / LC$, we have $df / f = dL / 2L$, and therefore

$$d\lambda = (A / \pi R_{\text{eff}} f) df \quad (2.3)$$

To eliminate 'A' from Eq. 2.3, we calibrate the system with several samples of high purity copper of different thickness and study the screening response [60,69]. Since inductance L is directly proportional to A , then,

$$A \propto L \propto 1 / f^2 = B - C (\pi R_{\text{eff}}^2) \quad (2.4)$$

Here $B = \pi R^2$ and a graph between $1 / f^2$ and R_{eff}^2 yields the constant C . Further, if the dc field is applied perpendicular to the plane of the sample then the extra penetration of the rf field is only along c-axis. Therefore from Eqs. 2.2 and 2.4,

$$-(1 / f^3) df \approx C b d\lambda \quad (2.5)$$

$$\text{and, } d\lambda = - (1 / C b f^3) df = - G df \quad (2.6)$$

Where G is a constant, which depends on geometric factors such as the coil configuration and the size of the sample.

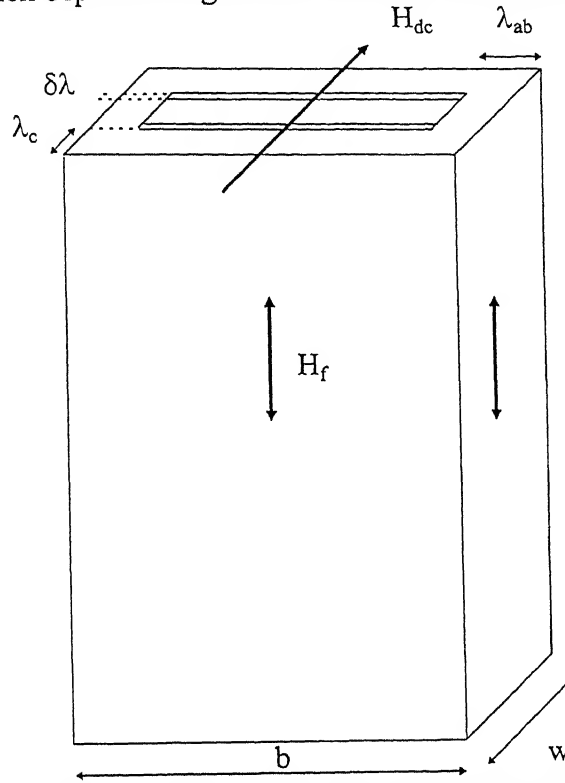


Figure 2.5 Effective area of flux expulsion when the dc field is applied perpendicular to the sample plane.

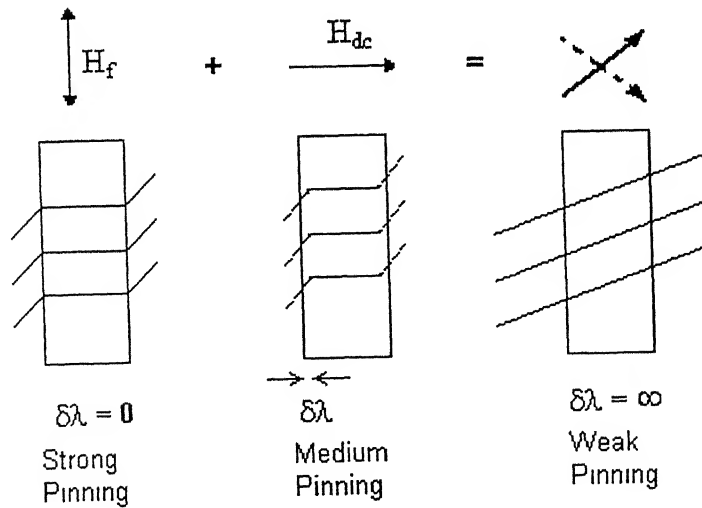


Figure 2.6 Enhanced rf field penetration with an external dc field depends on strength of vortex pinning in the material.

2.3.2 Apparatus description

2.3.2.1 Electronic circuitry

The diagram of tunnel diode oscillator circuit is shown in Fig. 2.7. Oscillators work on a form of instability caused by a regenerative feedback without which the input dies out due to energy losses. Reactive elements in a positive feedback circuit cause the gain magnitude and phase shift to change with frequency. In general, there will be only one frequency corresponding to which the gain magnitude is unity and the phase shift is equivalent to $0^\circ / 360^\circ$. This satisfies the basic criteria for production of sustained oscillations. Simple analysis would show that at resonance, the tank circuit is equivalent to a pure resistance of value $(L/C R_{dc\ coil})$. This resistance can be nullified by a negative resistance of magnitude $-R$ placed in parallel with the resonant circuit. The parallel combination gives infinite shunt resistance and the oscillations continue indefinitely without damping. A positive feedback circuit is equivalent to a negative resistance and many devices, specifically the tunnel diode with this property has been extensively used as oscillators. With extraordinary temperature stability, more so at low temperature and with delay time of the order of nano seconds, tunnel diodes are ideal choice for low temperature studies of materials upto a few thousand megacycles.

We have used a Germanium Power Devices BD2 tunnel diode which is equivalently called a germanium back diode. This is chosen because of low peak point current so that the ac field is negligibly small compared to the dc field. Maximum peak point current for BD2 is 0.5 mA and for our inductor, the ac field magnitude is 4.8 μ T. Low terminal capacity and series inductance, typically 6pF and 1.5 nH respectively, make it suitable for high frequency applications. The calculated output power and the negative resistance ($1/g_d$) are approximately 18 μ W and $-270\ \Omega$ respectively.

The frequency of the series parallel circuit shown in Fig. 2.7 is primarily dependent on the L and C of the tank circuit. This is important because a simple “series” circuit will lead to instability as fundamental frequency explicitly depends on magnitude of trans-conductance, g_d , which is a time averaged value and varies with voltage and temperature. The condition for constant amplitude of oscillation and resonating

frequency is obtained by the vanishing real and imaginary part to the total circuit impedance [70]. A detailed analysis for the “series parallel” circuit [71] shows that the resonant frequency is given by

$$f = \frac{1}{2\pi} \sqrt{\frac{1}{L(C + C_1)} - \frac{g_d^2}{C_1(C + C_1)}} \quad (2.7)$$

and for stable oscillations,

$$R_T = \frac{g_d}{\omega^2 C_1^2 + g_d^2} \quad (2.8)$$

where R_T is the effective resistance of the circuit other than the tunnel diode, consisting mainly of $R_{dc \text{ coil}}$ and R_B .

From the design point of view, R_T ought to be smaller than $1/g_d$, typically $0.7/g_d$. With this approximation Eq. 2.8 gives $C_1 = 120$ pF. Further,

$$C + \frac{C_1}{1 - R_T g_d} = \frac{1}{L \omega^2} \quad (2.9)$$

The inductance L of the coil depends on geometric factors and for our inductor it is approximately 2.3×10^{-6} H. This leads to a C value of 680 pF for 3.2 MHz frequency. In order to increase the quality factor Q of the oscillator, we have used a ATC 100B series multilayer porcelain capacitor, which has a Q factor of more than 1000 at 1 MHz. The thermal coefficient is 90 ± 20 ppm / $^{\circ}\text{C}$ with no aging effects. Further, these are nickel free and therefore there is hardly any change in capacitance due to the magnetic field.

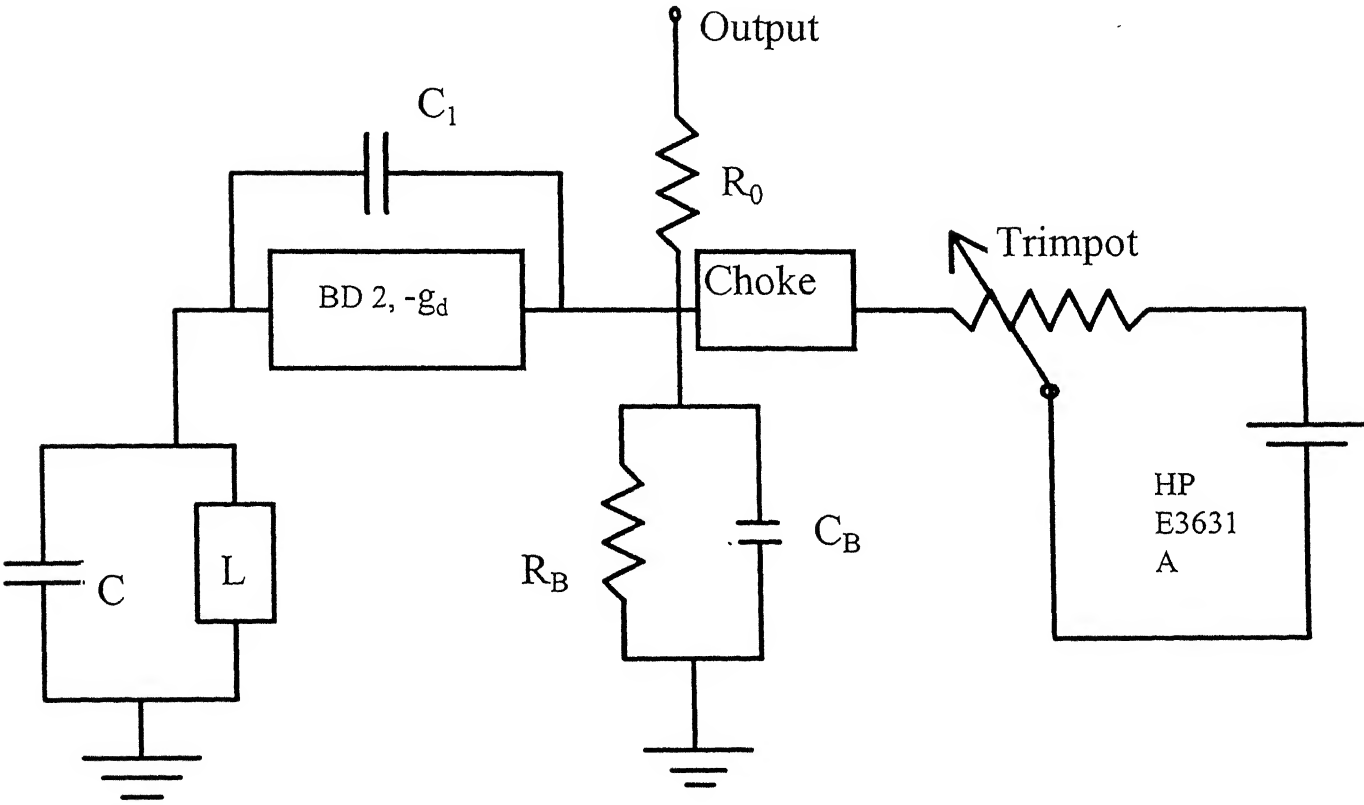


Figure 2.7 A series parallel tunnel diode oscillator circuit. Values of the circuit elements are given in the text.

The oscillator frequency is sensitively dependent on dc bias voltage. Since the oscillator swings over different portions of the I - V characteristics curve at different bias voltage, the harmonic content of the output changes with bias. This is because of the operation of the diode in the nonlinear region. Moreover, the change in bias voltage causes finite variations in voltage dependent capacitance C_d of the diode across the junction. This also leads to instability near the fundamental frequency. Therefore a steady bias voltage is of optimum importance. We have used a HP E3631A triple output dc power supply for this purpose. The voltage was fixed at 2.6 V with resolution 0.001 V and noise less than 2 mV. The potentiometer is a 500 Ω multiturn trimpot. From the equivalent circuit, dc bias can also be calculated. Bypass capacitor C_B is chosen large, so that it appears as short circuit at the operating frequency. The rf choke is to segregate ac signal from the dc power supply components. We have found optimum performance for the following set of components, $C_1 = 120$ pF, $C = 680$ pF, $R_o = 47$ Ω , $C_B = 330$ pF, choke = 0.1 mH. The output is 40 mV peak to peak. Some key advantages of the circuit used in the present case are as follows;

i) Only the tank circuit sees the low temperature enabling simplified shielding and isolation of stray EM radiation and influence from magnetic materials. Since the peak current remains constant for all field scans at different temperatures, $|H_f|$ is a constant for all measurements. The magnetic field dependence of tunnel diode is ruled out. This is not the case if the tunnel diode is inside the cryostat. ii) For the first time, to our knowledge, we have used a close cycle refrigerator and the stability is not compromised. iii) Because of proper radiation shield, no co - axial cable is necessary inside the cryostat. iv) To suppress parasitic capacitance no resistance in series with tunnel diode is included as this leads to disturbance in fundamental frequency oscillations. Instead, an extra 47 Ohm resistance (R_o) before the output leads to better stability.

The shift in frequency is measured with HP 53131A frequency counter which has an inbuilt oven time base for resolution of the order of 1 Hz in 10^{10} Hz. It has an added advantage of performing statistical analysis on-line with the experiment. The fluctuation introduced due to mechanical vibration generated by the close cycle piston is thus taken

care of by measuring the mean of 20 data points. The counter has adjustable triggering level and slope. Since the output is small, the measurements were made in automode, which sets the level at 50 percent of input signal at positive slope and high sensitivity. The magnetic field is ramped in steps by increasing current in a programmed way via HP 6030A autoranging dc power supply. The optimum programming resolution is 4.25 mA. A Ruthenium Oxide sensor of negligible magnetoresistance is used in conjunction with a programmable temperature controller (Scientific Instruments Model 5650) for measurement of temperature with a stability of $\pm .05$ K. In order to study the angular dependence of the vortex dynamics, the electromagnet was rotated with a stepper motor. The use of a worm gear assembly allowed a precision of 0.05 degree in the rotation. The frequency counter, magnet power supply, and the temperature controller and the stepper motor are interfaced to a 486PC via Keithley 486 GPIB card for data acquisition. The block diagram of interfacing is shown in Fig. 2.8

2.3.2.2 Design and fabrication

The apparatus we have used consists of three major parts: (i) a closed cycle cryocooler with the sample stage, (ii) detection and control unit held at room temperature, and (iii), an electromagnet for measurements in a dc field. In Fig. 2.9 we show a cross sectional view of the low temperature end of the variable temperature cryostat (APD Cryogenics USA, model 204SL) and a copper pillbox which is firmly screwed to the copper stem of the cryostat with indium seal. The pillbox contains a parallel resonant LC tank circuit. This is driven with the tunnel diode oscillator. The measurements are carried out by placing the superconducting sample inside the inductor of the tank circuit. The inductor is a 49 turn tightly wound solenoid of 42 gauge copper wire. It has inner diameter of 0.25 cm and length 0.64 cm. The inductor is glued to the walls of a cigar shaped cavity made in a cube of machinable ceramic. This rendered mechanical strength to the solenoid against thermal cycling and loading / unloading of the sample. The ceramic cube is then glued to a sapphire plate ($1 \times 0.5 \text{ in}^2$) which is clamped to a copper stem. The latter is soldered to the copper pillbox. The twisted pairs of the sensor wires and coil wires are taken out of the pillbox.

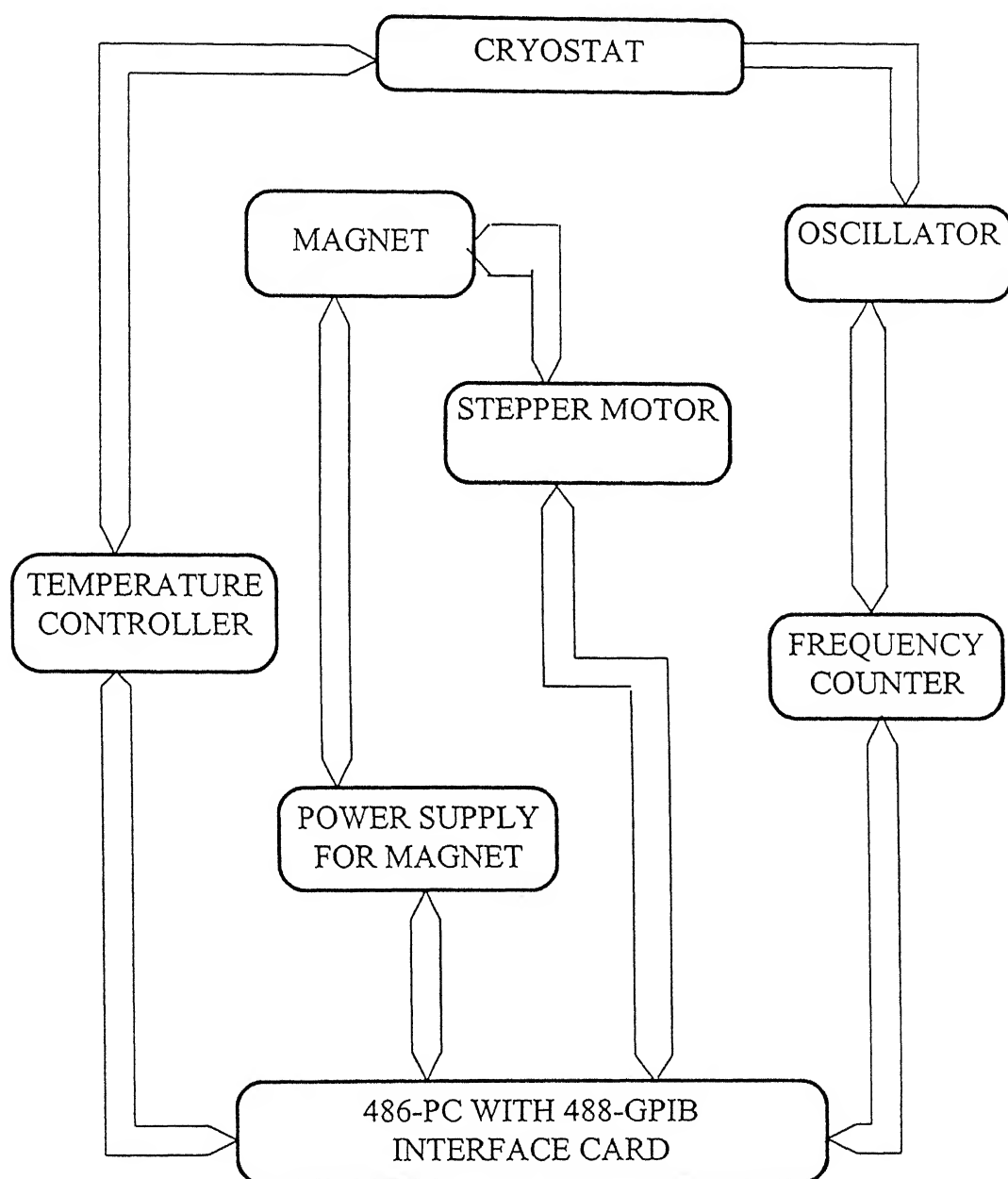


Figure 2.8 Block diagram of Interfacing of the tunnel diode oscillator experiment

through a stycast sealed leak tight port. A glove box was used to fill the pillbox with helium exchange gas for better temperature stability during the measurements. The pillbox is then attached to the coldhead of the cryostat which easily goes down to 9 K.

The holder along with the sample slides smoothly into the inductor. The 680 pF capacitor is soldered to the inductor inside the pillbox. Thus only the critical components of the oscillator i.e. the inductor and the capacitor see the low temperatures and the rest of the components including tunnel diode stay at room temperature. The axis of the inductor in our experiment is oriented such that the rf magnetic field (\mathbf{H}_f) is always perpendicular to the dc magnetic field (\mathbf{H}_{dc}).

While the maximum shift in frequency at T_c is obtained by placing the oriented platelet sample perpendicular to the axis of the inductor, this configuration restricts \mathbf{H}_{dc} only to the ab - plane of the sample. On the other hand, if the plane of the crystal is made parallel to the axis of the solenoid, the orientation of \mathbf{H}_{dc} can be varied from \mathbf{H}_{dc} parallel to ab - plane to \mathbf{H}_{dc} parallel c-axis. The orientations of the fields, induced rf currents and crystallographic axis of the sample are shown in Fig. 2.10. It is important to note that in this configuration \mathbf{J}_f is always orthogonal to \mathbf{H}_{dc} and thus the vortices experience the maximum Lorentz force. The schematic diagram of the experimental set up is shown in Fig. 2.11.

2.3.2.3 Calibration

As mentioned earlier, the experiment depends crucially on the stability of the oscillators. In Fig. 2.12 we show the stability of tunnel diode oscillator during a typical magnetic field scan. It is taken at 120 K (i.e. in the normal state) by ramping the field in the steps of 25 mA upto 5 A and back to zero in one hour. The maximum current corresponds to a dc field of 3.2 kG for 8.4 cm pole separation. The Fig. also reflects the negligible drift of the oscillations with time. The 20 Hz fluctuation is insignificant compared to the magnitude of the effect, that is a frequency shift of ~28 KHz at the superconducting transition. It must be mentioned however that an order of magnitude improvement in stability can be achieved by using a liquid helium cryostat instead of close cycle cryocooler.

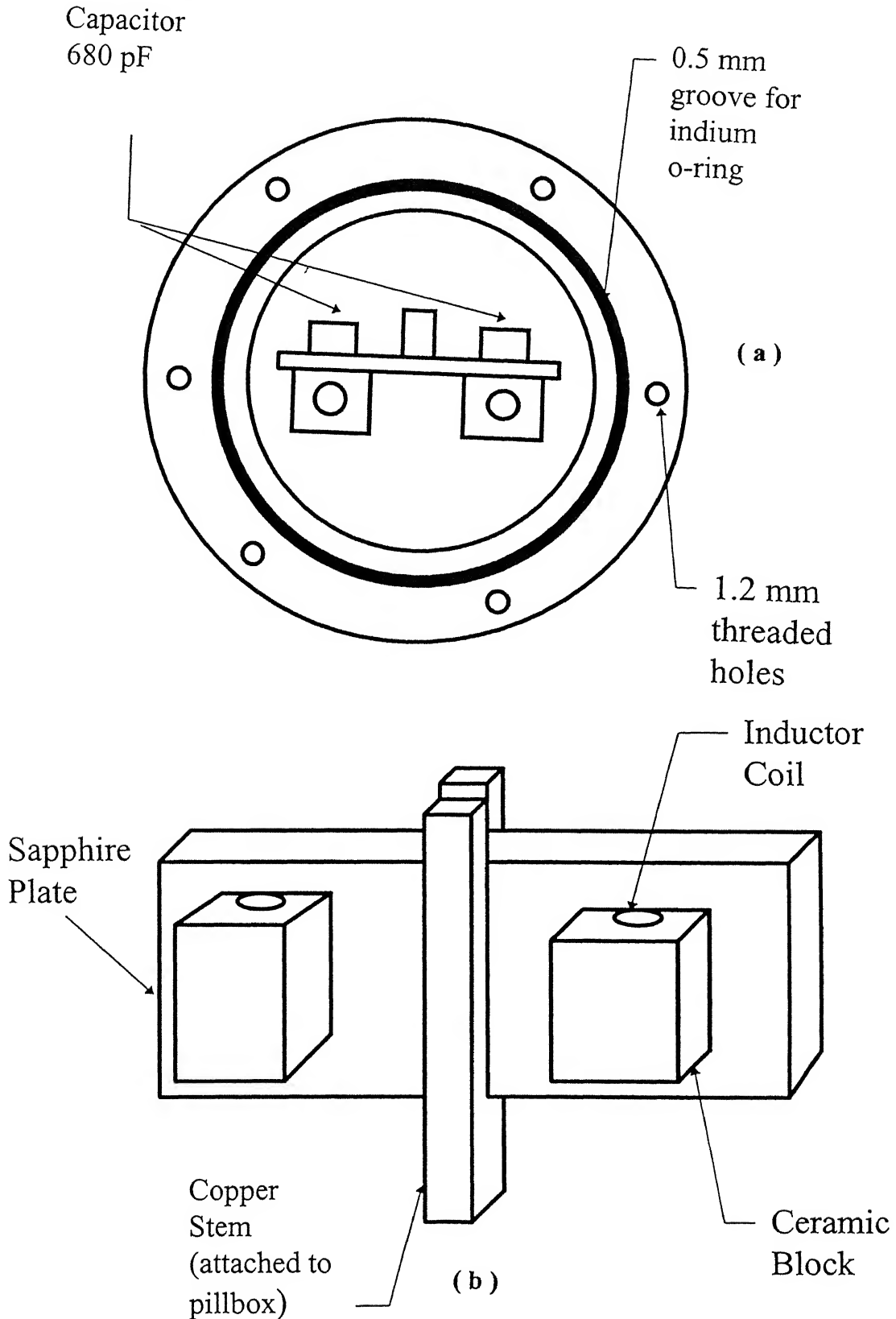


Figure 2.9 Sample Mounting stage of the cryostat: (a) Cross-sectional view of the copper pillbox housing two LC tank circuits. (b) The sapphire plate and the ceramic cubes are shown separately.

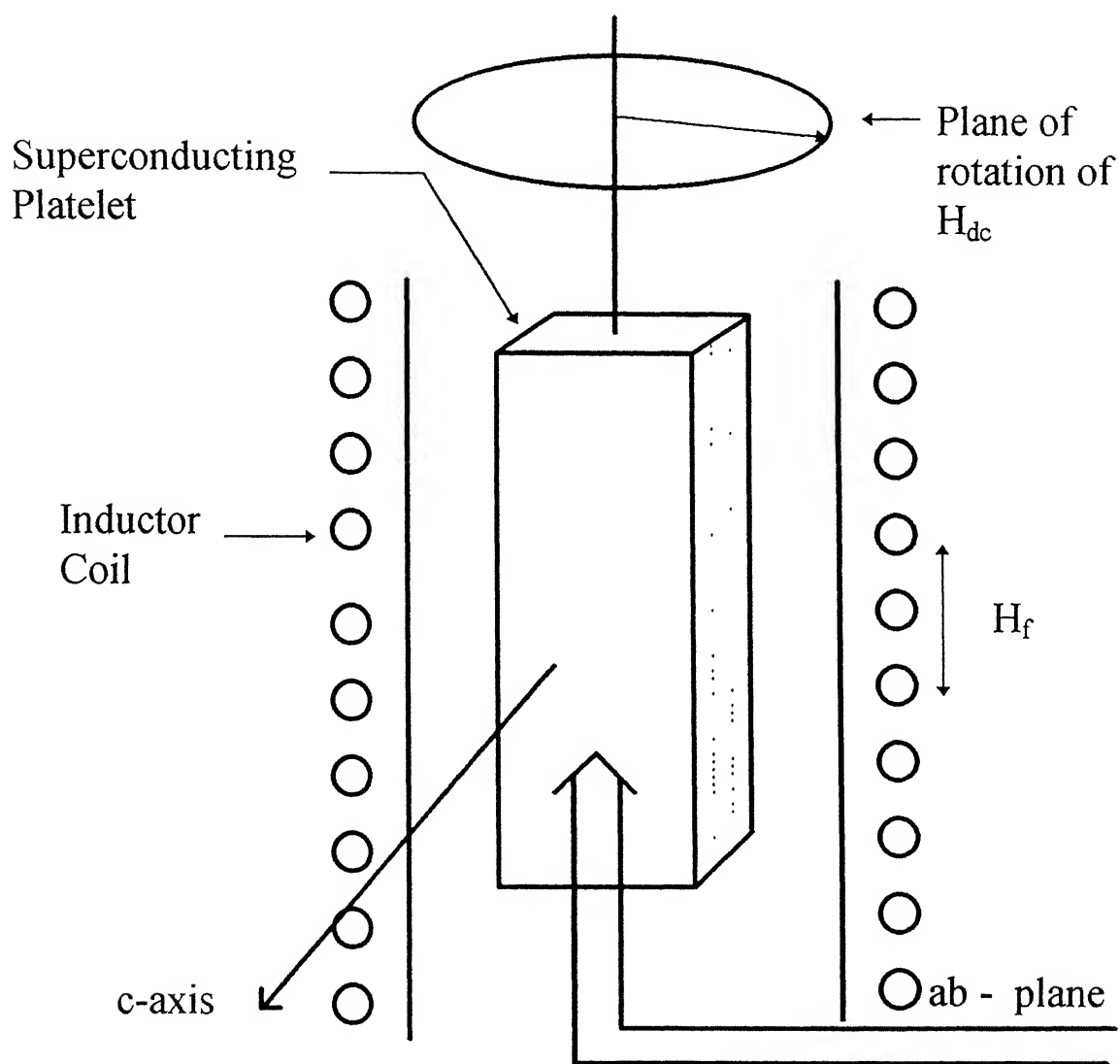


Figure 2.10 Schematic diagram showing the inductor coil, superconducting platelet sample and orientation of magnetic fields and crystallographic axes.

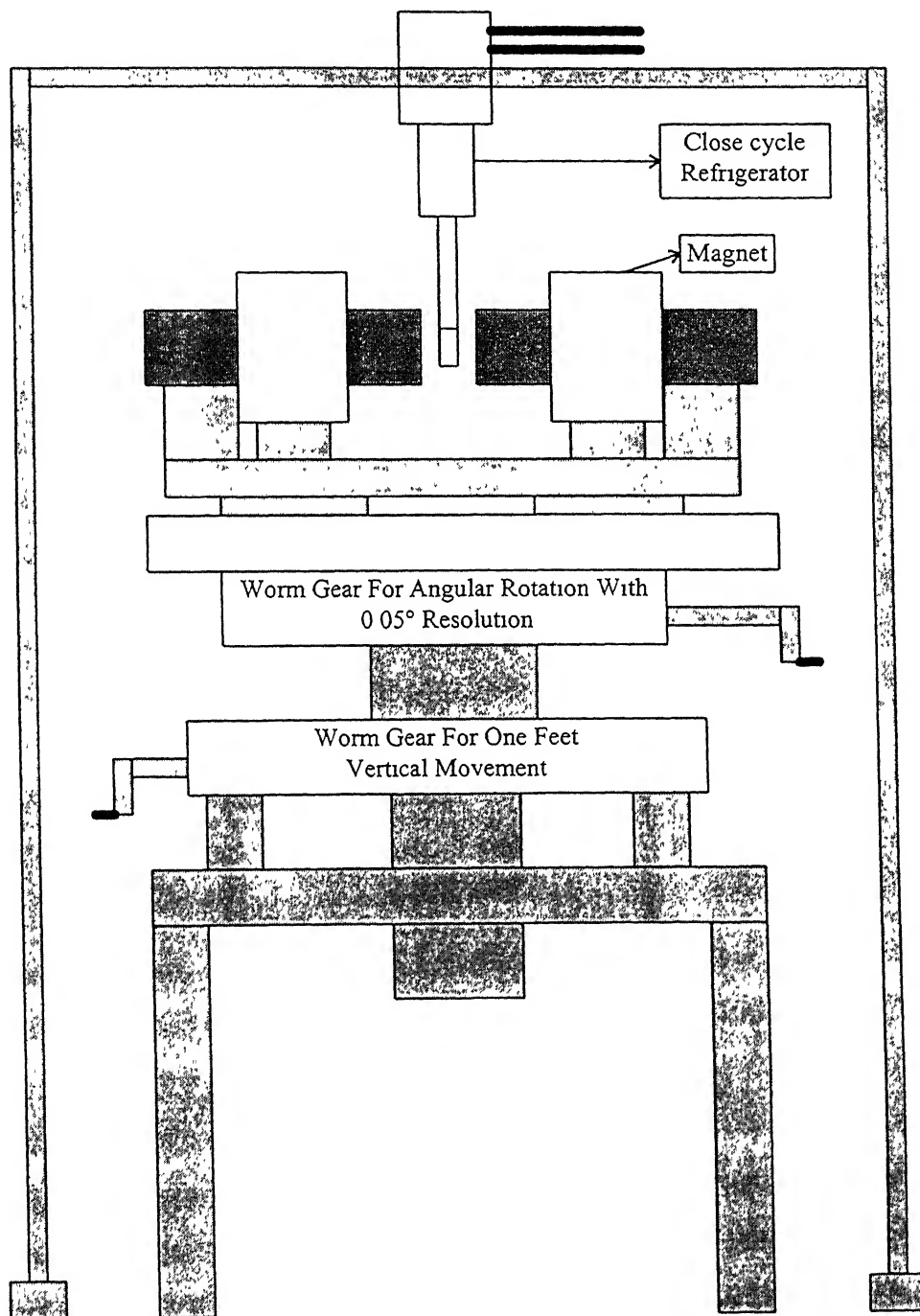


Figure 2.11 Block diagram of the rf penetration depth measurement setup.

While most of our study focuses on relative change in penetration depth, a quantitative analysis of pinning force constants required accurate determination of G factor for the coil and sample geometry. Following the method of Shawlow and Devlin [60], we have calibrated our system using OFHP copper plates of size similar to that of our platelet samples. This calibration procedure has also been used by Sridhar et al. [69]. The effective thickness of the plates was varied from $80\mu\text{m}$ to $320\mu\text{m}$ and after placing the plates, the corresponding frequencies were noted down. The plot between $1/f^2$ Vs. R_{eff}^2 yielded a straight line of slope $C = 7 \times 10^{-28} \text{ Hz}^{-2} \text{ \AA}^{-2}$ (see Eq. 2.4). For the platelet geometry, assuming negligible field penetration from the sides, the G factor as calculated from Eq. 2.6 is $2.2 \pm 0.4 \text{ \AA} / \text{Hz}$, where the error is due to the uncertainty in measuring the thickness accurately.

Fig. 2.13 shows the frequency shift of the empty coil plotted against temperature. This shift in frequency is primarily due to shrinking of coil radius at low temperatures. At very low temperatures, saturation effects are observed. The true response of the superconducting samples was extracted after subtracting the empty coil response (background) from the measured frequency.

The demagnetization factor (n) for our sample geometry is calculated assuming an ellipsoidal volume for the sample [72].

$$n = (1 - \gamma^2)^{-1} [1 - \gamma(1 - \gamma^2)^{-1/2} \cos^{-1} \gamma] \quad (2.10)$$

where γ is the ratio of polar axis to equatorial axis. For our sample geometry, $n \sim 0.7$ and the demagnetization factor for field enhancement is ~ 4.4 . But considering dominant granularity we have not taken this factor into account during our analysis.

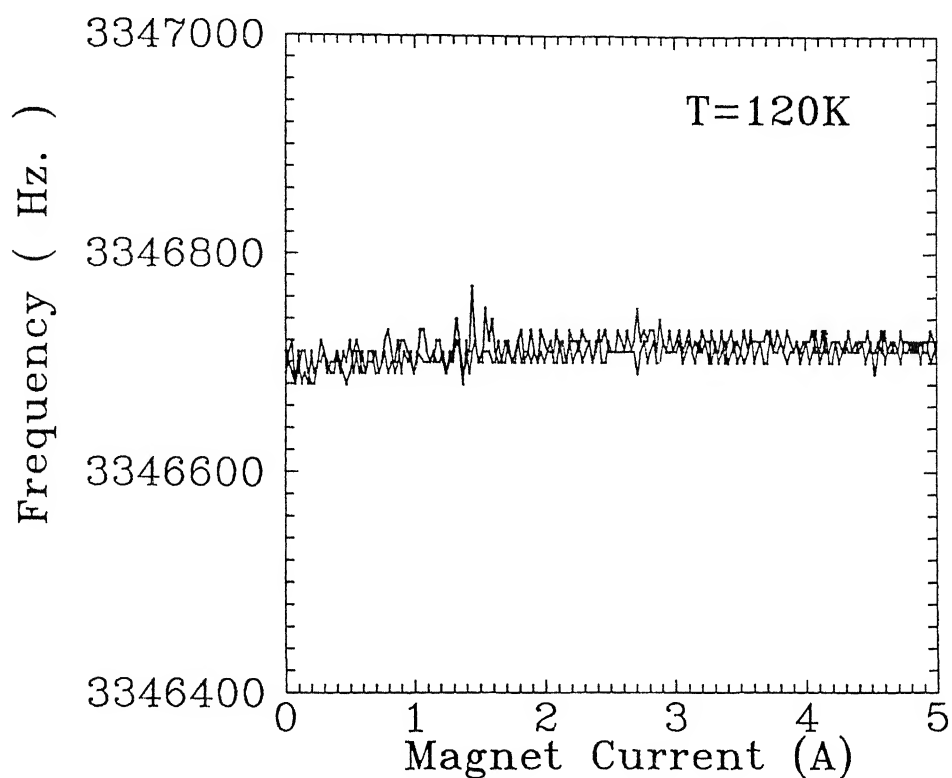


Figure 2 12 Resonant frequency shift of the tunnel diode circuit at 120 K plotted against magnet current. The duration of the field scan is 1 hour.

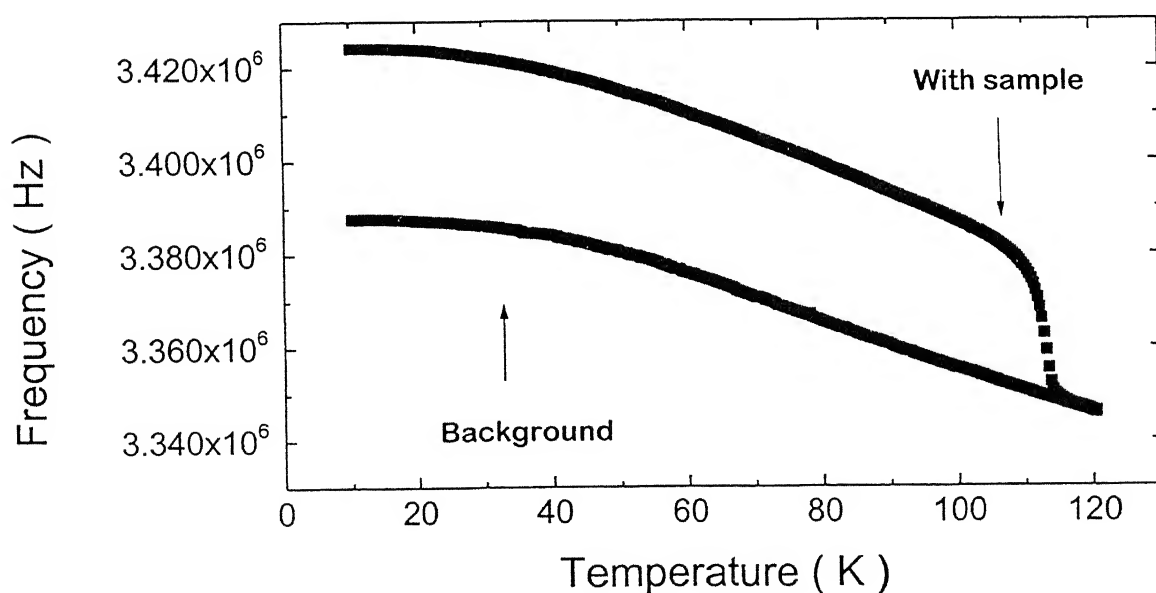


Figure 2 13 Frequency shift for the tunnel diode circuit for the empty coil and for the coil with sample.

2.4 DC Flux Transformer Experiment

2.4.1 The technique

The experiment consists of ab-plane and c-axis electrical transport measurements in the mixed state of silver sheathed Bi-2223 samples. With the flux transformer contact configuration, it is possible to simultaneously study the magnetic field induced dissipation in both faces of the sample. When the current is injected in the top surface, the experiments yield ab-plane resistivity along the top and bottom surfaces. Alternatively a probe current along c-axis would lead to measurement of c-axis

2.4.2 Apparatus description

A schematic diagram of this apparatus is shown in Fig. 2.14. Insets of Fig. 6.1a and Fig 6.1b show the contact geometry for the ab-plane and c-axis transport measurement respectively. The samples are glued to a sapphire plate using GE varnish and placed in a dip-stick type cryostat. The measurements are performed by immersing the sample holder in liquid nitrogen dewar which was placed between the pole pieces of Varian V2100 NMR electromagnet. Six contacts, four on the top and two on bottom surfaces are soldered with indium considering excellent Ohmic contact between the silver sheath and superconducting core. The distance between the contacts was ≈ 1.2 mm. The Ag sheath was carefully removed from the sides of the platelet to eliminate the possibility of a direct short between the top and bottom face. This configuration however has a direct influence on the normal state properties since the current flow takes place via the silver sheath rather than the metallic Bi-2223 core which has an order of magnitude higher resistivity. The bottom sheath and the core act as parallel combination of resistances above the superconducting transition temperature. Because of relatively large dimension of the sample, we could flow 150 mA as probe current to amplify the signal strength. The linearity of the effects are verified by observing the effects by varying current from 5 mA to 150 mA. The contribution due to thermal voltage was eliminated by nulling the background voltage at zero current.

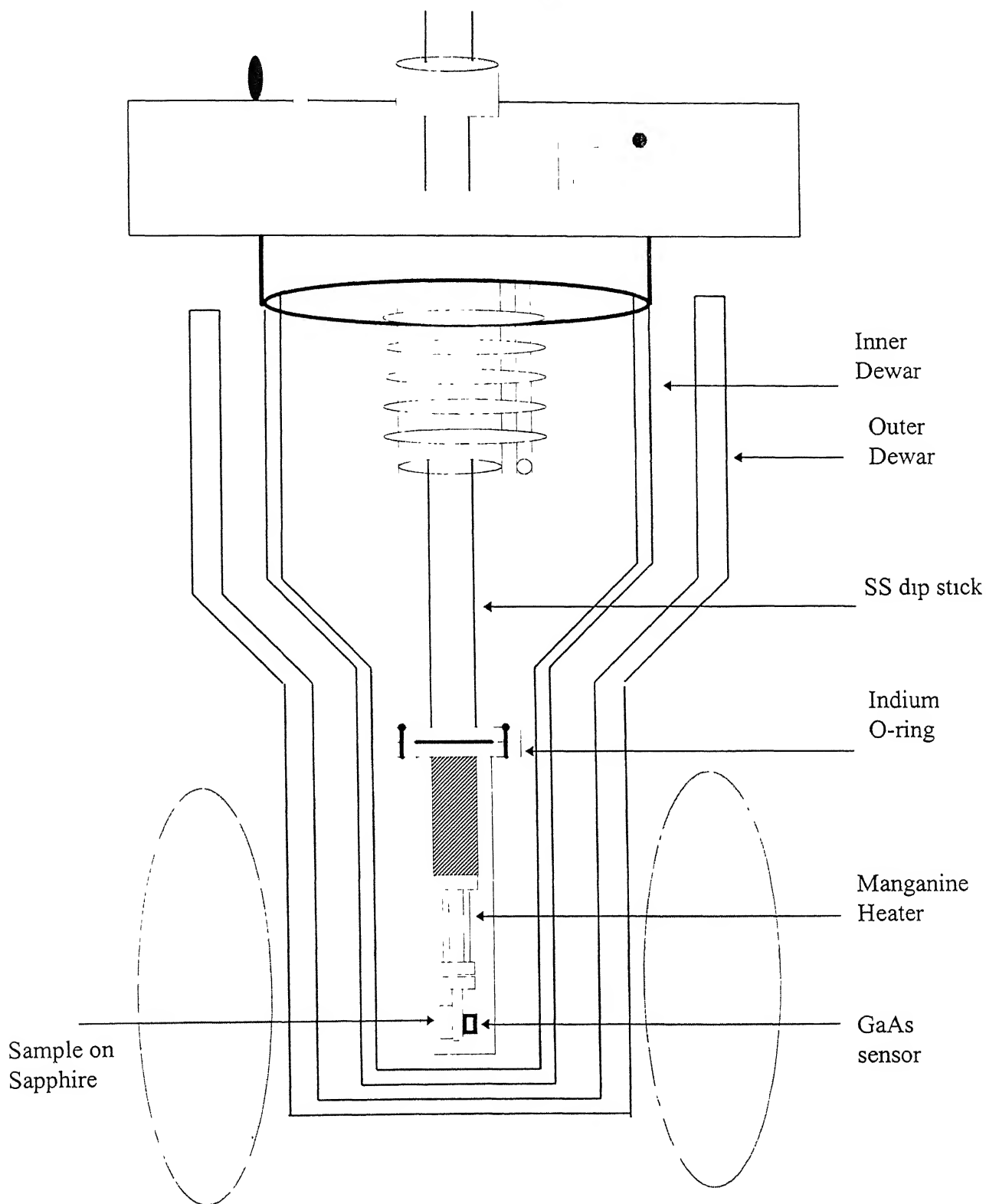


Figure 2.14 Transport experiments setup for Flux Transformer measurements.

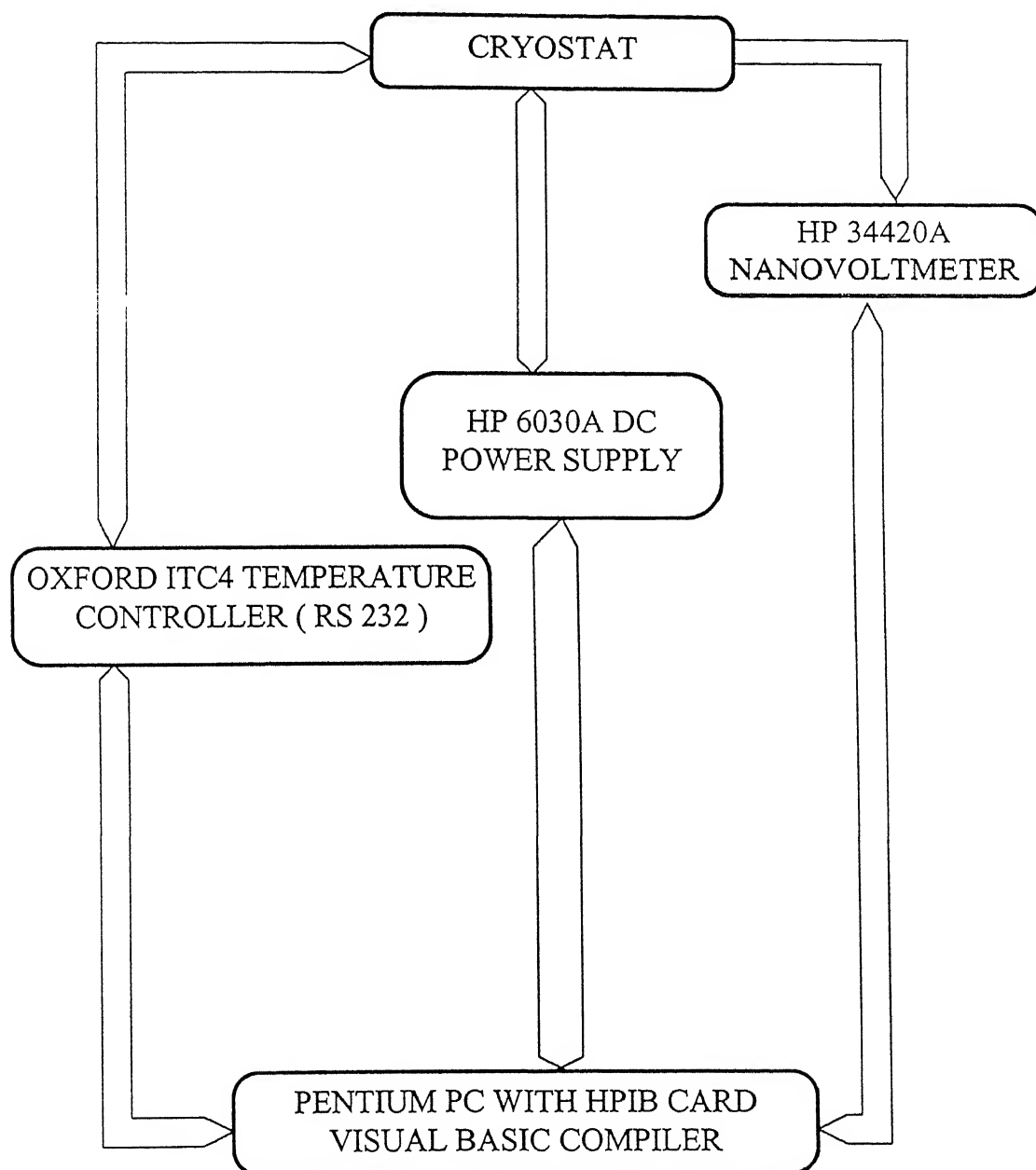


Figure 2.15 Block diagram of interfacing for transport measurements.

The measurements were made using a HP 34420A Nano Voltmeter, Oxford ITC4 temperature controller and HP E3631A Current Source. The magnetic field was applied parallel to c-axis. The temperature was ramped at a constant rate in the dynamic mode. The block diagram of the Visual Basic interfacing scheme is shown in Fig. 2.15.

Chapter 3

Pinning and Flux Flow properties of Bi-2223 tapes

3.1 Introduction

The severe thermally activated vortex dynamics in BiSCCO superconductors is the prime hindrance for their potential engineering applications at liquid nitrogen temperature. This highly dissipative mixed state over a broad range of temperature is the result of intrinsic and extrinsic factors such as; i) structural anisotropy, ii) short coherence length, hence small pinning energies, iii) granularity and weak link behavior, and iv) lack of pinning centers in the bulk of material. Unlike YBCO, where twin planes and secondary phase precipitates act as effective pinning centers, the dislocations and stacking faults in BiSCCO tapes do not render sufficient pinning ability at high temperatures. But both in YBCO [9] and in Bi-2212 [8] single crystals manifold increase in critical current density has been achieved by introducing columnar defects through heavy ion irradiation. In this chapter, we present our measurement of pinning and Flux flow properties in Bi-2223 tapes using the rf penetration depth technique. The measurements have been

done on as grown as well as heavy ion irradiated samples. For the dc field aligned perpendicular to the plane of the platelet (Predominantly $\mathbf{H} \parallel \mathbf{c}$ configuration), three distinct regimes of field variation of $\delta f (H, T)$ (equivalently $\delta \lambda (H, T)$) are identified which correspond respectively to flux flow in grain boundary/weak link region, intragrain pinning and intragrain flux-flow with the increasing field. The pinning force constant (Labush parameter) is evaluated and compared for the unirradiated and heavy ion irradiated Bi-2223 tapes.

Measurements of the shift in resonant frequency of the tunnel diode oscillator were made at fixed temperature and orientation of the sample while the magnetic field was ramped in steps. Some measurements have also been made as a function of temperature for fixed field values. However, in this case the data had to be corrected for temperature variations in the resonant frequency ' f ' of the empty coil. The ' f ' of the coil on the other hand does not vary with field as long as the temperature is held constant. Since the frequency shift δf is directly proportional to the change in rf penetration depth $\delta \lambda$, the relative changes in sample response due to temperature and field variation is adequately represented by either of them. The graphs are plotted either in terms of $\delta \lambda$ or δf . Unless otherwise mentioned they represent the modulus of the effective change. Throughout this thesis H is equivalent to external dc field H_{dc} .

The data are analyzed in the framework of the theories for rf penetration depth in type II superconductors. As discussed in Section 1.1.2.1a, in the dilute limit of flux density and fluxon motion subjected to a periodic pinning potential, both Campbell penetration depth λ_c and flux flow penetration depth λ_f vary as \sqrt{B} , and therefore it is possible to infer k_p and η from the measurement of rf penetration depth provided the pinning dominated and flux flow dominated regimes of vortex dynamics could be established in the data.

3.2 Results of unirradiated Bi-2223 platelets

3.2.1 Temperature dependence of rf penetration depth

Fig. 3.1 shows the temperature dependence of the frequency shift for the measurements performed at zero-field and at 1 and 2 kG field oriented perpendicular to the plane of the tape. In these measurements the sample was cooled in zero field (with the sample stage shielded with μ -metal) to the lowest temperature (10 K) and the data were taken in the warmingup cycle. The frequency shift δf after background correction is defined as;

$$\delta f(H, T) = | f(H, T) - f(0, 10\text{ K}) | \quad (3.1)$$

From the data taken at zero-field we note that the onset of superconductivity occurs at 112.1 K and 50% screening is achieved in the temperature interval of ~ 3 K. In the presence of the dc field, the onset of screening shifts to lower temperatures. Further, the frequency shift at a given temperature in the mixed state is higher than the δf in the Meissner state. This behavior of δf is reminiscent of the behavior of flux flow resistivity in highly layered cuprates [73-75].

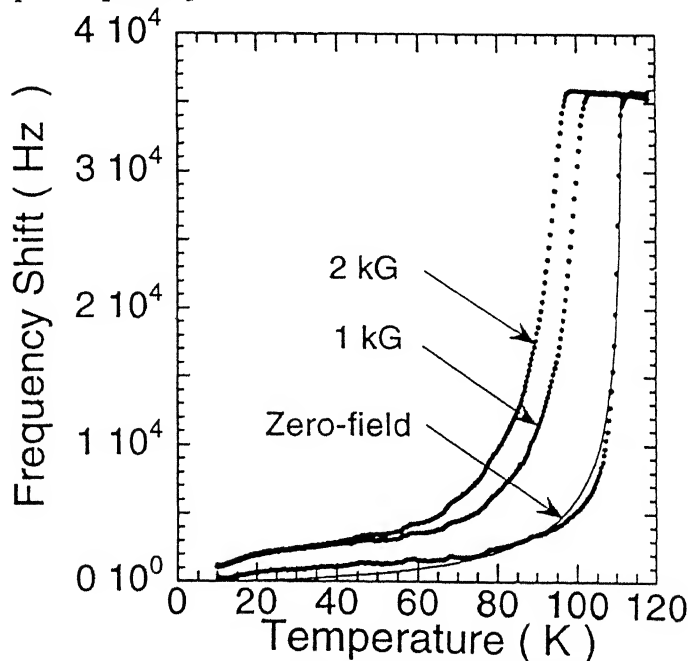


Figure 3.1 Zero field cooled temperature scan of unirradiated Bi-2223 sample at zero field, 1 kG and 2 kG.

3.2.2 Field dependence for $\mathbf{H} \parallel \mathbf{c}$ -axis

Some typical zero-field-cooled measurements of $\delta f(\mathbf{H}, T)$ at several temperatures for the dc field oriented perpendicular to the plane of the platelets ($\mathbf{H} \parallel \mathbf{c}$ -axis) are shown in Fig. 3.2. The data have been taken in the forward as well as reverse directions of the field. At temperatures closer to T_c , the rapid increase of δf with field signifies a quick penetration of the rf currents into the sample. The δf saturates when the rf field moves into the entire sample. The saturation value of δf is obviously lower the closer we are to T_c . This observation is consistent with the temperature dependence of δf shown in Fig. 3.1. On decreasing the temperature further, the frequency shift does not saturate even at the maximum field (3.2 kG) used in these experiments. The rf field penetration at the maximum applied dc field in fact decreases rapidly as we go to lower and lower temperatures. The other noticeable feature of the data shown in Fig. 3.2 is the negligibly small hysteresis in δf on field reversal. The history effects become strong in measurements performed below ~ 45 K

As we have outlined in sections 1.1.2.1 and 3.1, the change in complex penetration depth in the mixed state is dominated overwhelmingly by the vortex contribution. In the pinning and flux flow dominated regime it is expressed as;

$$(\delta\lambda)^2 = B\phi_0 / \mu_0 k_p \quad (3.2)$$

$$\text{and, } (\delta\lambda)^2 = 2B\phi_0 / \mu_0 \eta \omega \quad (3.3)$$

respectively. In Fig. 3.3. we have plotted the variation of $\delta f(\mathbf{H}, T)$ as a function of the dc magnetic field ($\mathbf{H} \parallel \mathbf{c}$) at several temperatures in the range of 103 K to 25 K. At temperatures $T < 90$ K, the frequency shift shown in Fig. 3.3 has three distinct regimes of field variation. To emphasize this point, in Fig. 3.4a and 3.4b we show δf^2 as a function of applied field for measurements performed at 60 K and 80 K respectively. In both the cases three distinct field regimes exist, and in the two low - field regimes a δf^2 Vs H relationship is followed. The fields at which a change of behaviour is observed

is defined as H_1^* (T) and H_2^* (T). It is found that the critical fields show a systematic decrease for measurements performed at higher and higher temperatures.

In view of the known microstructure of the Bi-2223 tapes, it can be safely argued that the field regime below H_1^* corresponds to the penetration of the rf field into grain boundaries via the motion of quasi Josephson type intergranular vortices. The oscillating currents of the rf field applied along the breadth of the specimen would move these Josephson vortices along the length of the grain boundaries. This is manifested by a sharp rise of δf at the lower values of the field. A dc magnetization measurement in this geometry is less likely to show this effect as it samples steady currents induced in the ab-plane. Indeed, the magnetization data do not reflect the granular character, and scale with the size of the sample [37,40,41]. The response of such weak links is generally not seen in a transport measurement either because the self-fields in such measurements are relatively large compared to the decoupling fields. A significantly lower value of the transport J_c as compared to the J_c deduced from the critical state model applied to magnetization however, does indicate the presence of decoupled grains in high current transport measurements.

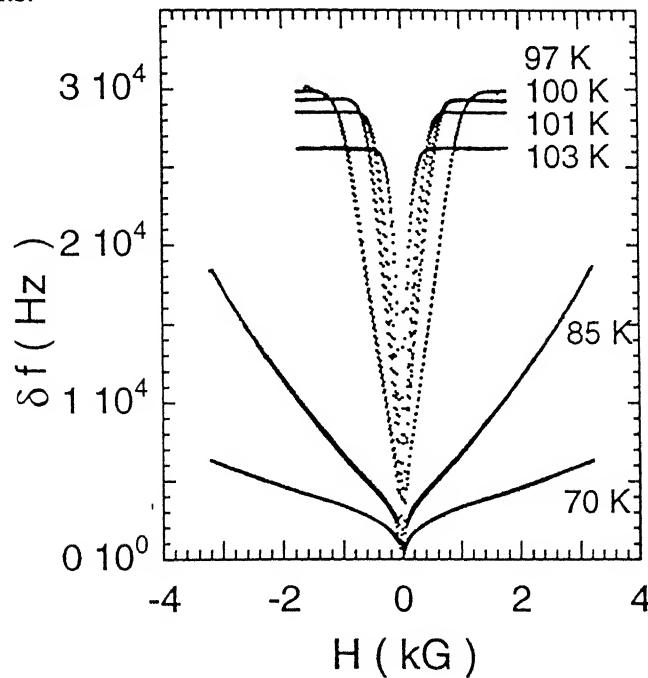


Figure 3.2 The frequency shift $\delta f [= |f(H, T) - f(0, T)|]$ as the external dc magnetic field which is oriented perpendicular to the tape plane is cycled in the positive and negative directions.

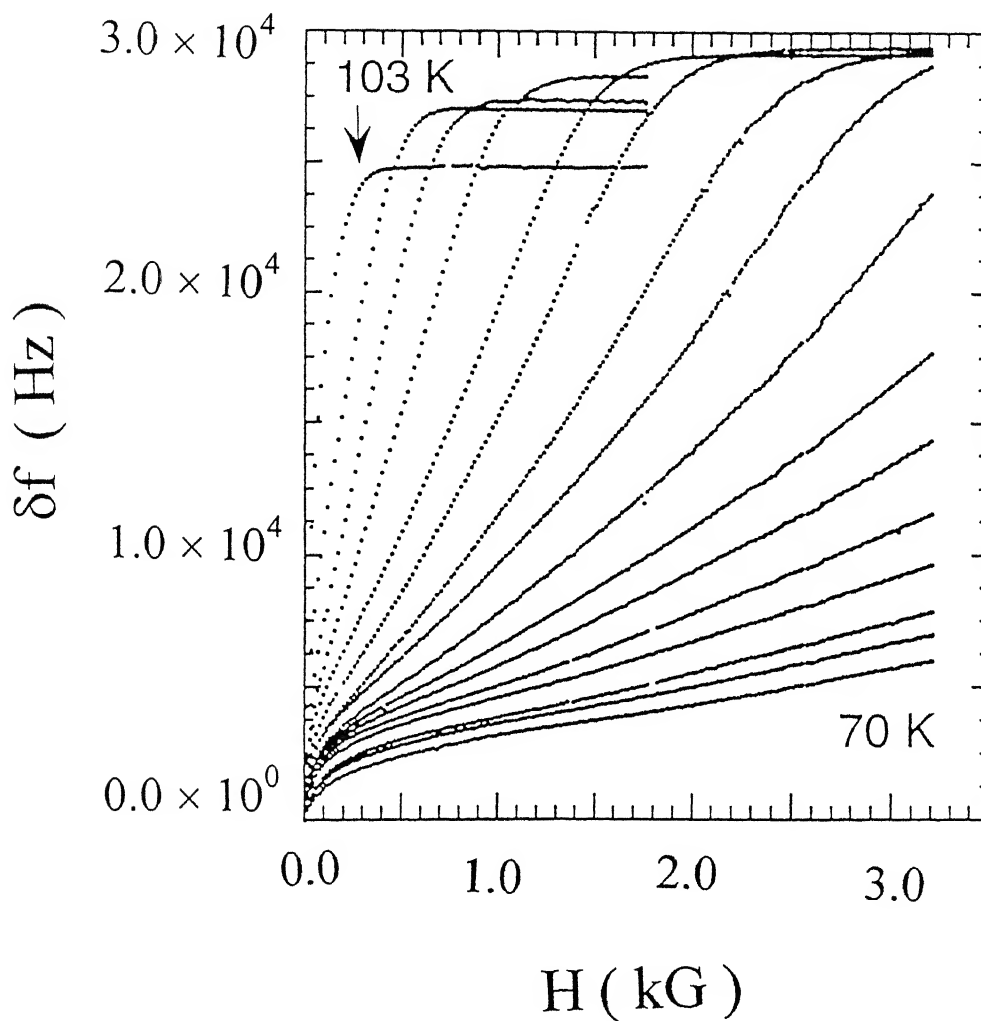


Figure 3.3 Variation of frequency shift δf as the external magnetic field oriented perpendicular to the plane of the tape is increased from zero to 3200 Gauss. Curves shown in the Figure have been obtained from frequency measurements done at 70, 72.5, 75, 77.5, 80, 82.5, 85, 87, 89, 91, 93, 95, 97, 99, 101 and 103 K.

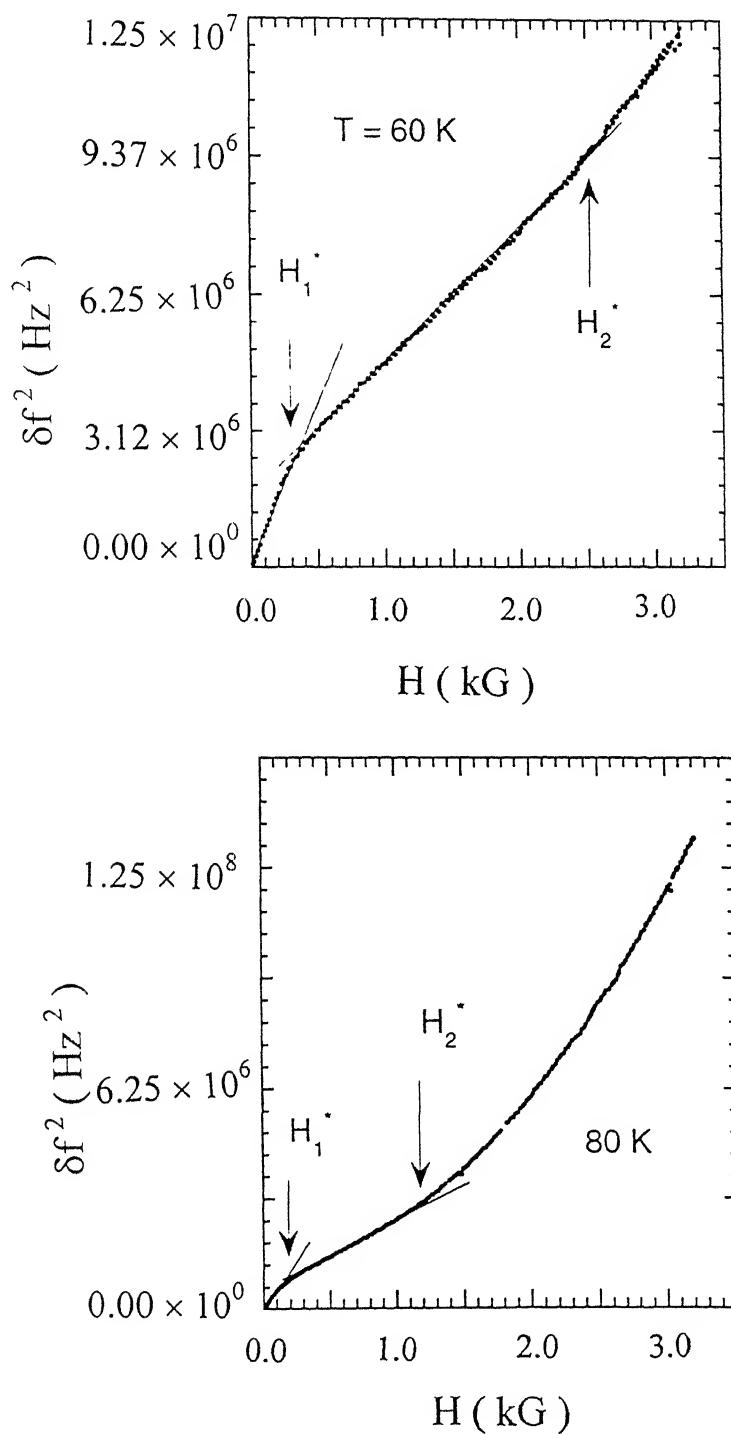


Figure 3.4 (a) $(\delta f)^2$ Vs. H at 60 K and, (b); $(\delta f)^2$ Vs H at 80 K. The external dc magnetic field H , was perpendicular to the plane of the tape in both cases. The range of field over which a $(\delta f)^2 \sim H$ dependence is followed is shown and the critical fields H_1^* and H_2^* are marked (see text)

For fields $H < H_1^*$ the vortices are localized at the grain boundaries. From the slope of the δf^2 Vs H curves for fields $H < H_1^*$ and if we assume Campbell type of field penetration, we can calculate the pinning force constant for the vortices localized at the grain boundaries. The force constant k_p^g drops from a value of $\sim 3 \times 10^2 \text{ N/m}^2$ at 60 K to $\sim 30 \text{ N/m}^2$ at 80 K. The rapid drop of k_p^g with increasing temperature shows that the grain boundary pinning is extremely weak. A further increase in field beyond $H_1^*(T)$ would lead to flux penetration into the grains. The penetration of the rf field into the specimen as H increases above $H_1^*(T)$ is much slower. This is the regime where flux pinning in the grains dominates the vortex dynamics. The behaviour of the calculated Labush parameter (k_p^\perp) in this regime of intragranular pinning is shown in Fig. 3.5. The inset of Fig. 3.5 shows variation of H_1^* and H_2^* with temperature. Since these two fields signal the threshold for field penetration into the grains and the onset of flux flow respectively, it is suggestive to identify them with H_{c1} and the irreversibility field (H_{irr}) respectively of Bi-2223. The curve for H_2^* in the low-field regime investigated here indeed follows the $H \sim (1-t)^{3/2}$ dependence of the H_{irr} seen in $\text{YBa}_2\text{Cu}_3\text{O}_7$ [76-78]. The irreversibility field of Bi-2223 tapes deduced from transport J_c measurements by Matsushita et al. [79] also shows a dependence of the type $H \sim (1-t)^n$ with $n = 1.5$ for tapes of similar J_c as used here.

The critical field H_2^* is also similar to the crossover field H^* at which the dynamics changes from pinning dominated to flow dominated in the case of the layered organic superconductor $(\text{BEDT-TTF})_2\text{Cu}(\text{NCS})_2$ [20]. One can in principle calculate the viscosity coefficient η from the dependence of δf on the applied field for fields $H > H_2^*$. However, in the present case a continuous change of slope of the δf^2 Vs H curves above H_2^* makes the viscosity a field dependent quantity. Since frequency shift for field $H > H_2^*$ also derives contributions from Thermally Activated Flux Flow and the classical skin effect of normal carriers [19,20], there are other factors that are probably responsible for the field dependent slope.

The pinning force constant at 65 K for example calculated from the data is comparable to the reported value of k_p^\perp for YBCO [62,80,81] and higher than for Bi-2212 [82]. The elementary pinning considerations show that the upper limit for the pinning energy U per unit length of a vortex is $(H_c^2/8\pi)\pi\xi^2$. If the range r_p of the pinning potential

CENTRAL LIBRARY
I. I. T., KANPUR

131101

is $\sim \xi$, then $k_p \sim U/r_p^2 = H_c^2/8\pi$. Taking H_c (65K) of 7000 Gauss [46], we infer that k_p^\perp at 65 K is $\sim 6.0 \times 10^5 \text{ N/m}^2$ which is very high compared to the measured value of $\sim 1 \times 10^3 \text{ N/m}^2$. The lower value of measured k_p^\perp indicates that the range r_p of the pinning potential is less than the coherence length ξ . Such pinning centers are presumably due to stacking faults and oxygen related defects in the material. From the estimate of r_p , the range of the pinning force and the force constant k_p^\perp , we can write the maximum pinning force on a single vortex as $\sim k_p^\perp r_p$. Equating this maximum pinning force to the maximum Lorentz force yield the depinning critical current density J_{co} . With $r_p \sim 10 \text{ \AA}$ the value of J_{co} at 65 K for transport along the plane of the platelet is of $\sim 10^5 \text{ A/cm}^2$. This is the upper bound for the intragranular critical current in the material

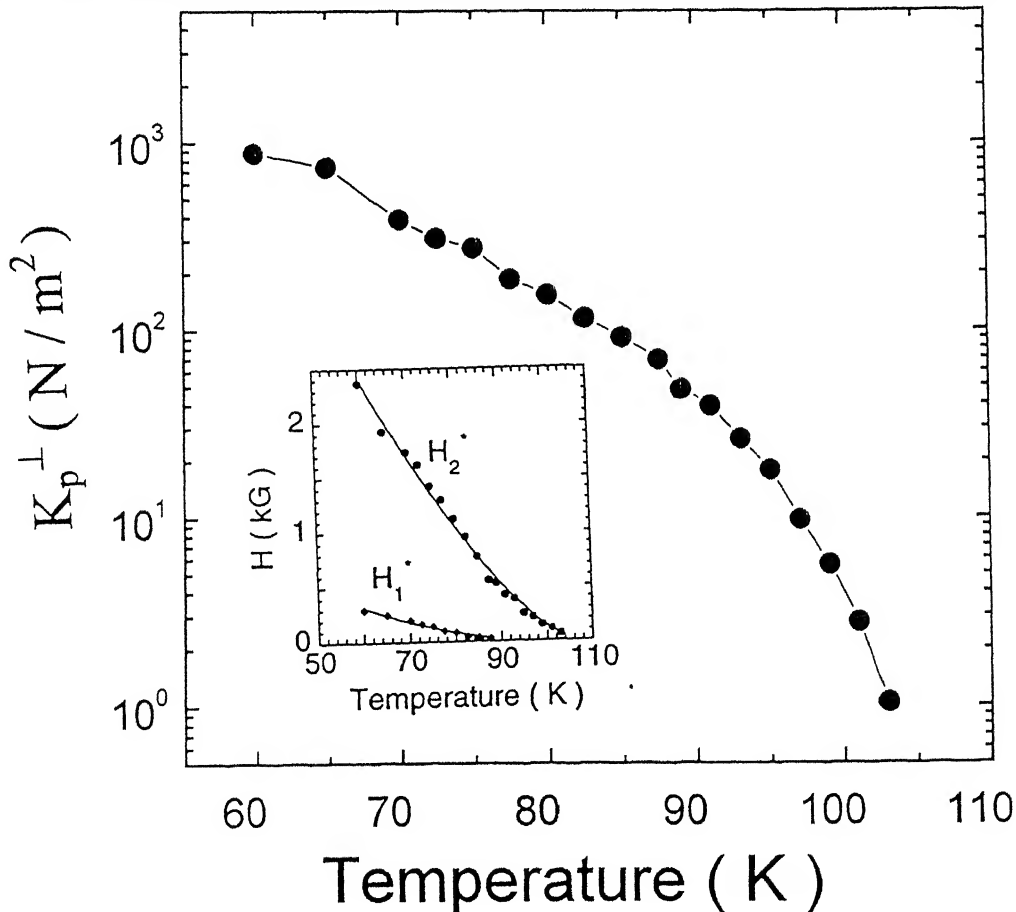


Figure 3.5 The pinning force constant k_p^\perp deduced from δf data between field H_1^* and H_2^* is plotted as a function of temperature. The variation of H_1^* and H_2^* with temperature is shown in the inset. Solid lines through data points are guide to eye.

3.2.3 Field dependence for $H \parallel ab$ plane

The behavior of the frequency shift $\delta f(H, T)$ for the dc field oriented parallel to the plane of the tape is shown in Fig. 3.6. A visual comparison of this data with $H \parallel c$ case (Fig. 3.2) shows some significant differences. For the parallel field case, the shift in frequency ($\sim \delta\lambda$) does not saturate even at a temperature as high as 101 K. While for the same dc field applied parallel to c -axis, the saturation occurs at ~ 89 K. This is analogous to the behaviour of the resistive transition which is much less broader in layered cuprates when the external field is made parallel to the Cu-O planes [73,74]. Further, δf reduces rapidly in this case as we go to lower temperatures. In order to establish the explicit dependence of δf on field, the inset of Fig. 3.7 show the variation of δf^2 with H at 80 K. Unlike the case of $H \parallel c$ where three distinct regimes of H dependence were observed, here only two regimes are seen. The initial rise is attributed to flux penetration into the c -axis twist boundaries, where as the region of constant slope beyond H_1^* corresponds to the regime where flux is trapped between Cu-O planes inside the grains. This intrinsic intragranular pinning being much stronger, we do not observe the crossover to flux flow behavior in the regime of field investigated here. In Fig. 3.7 we show the variation of the pinning force constant k_p^{\parallel} calculated from the slope of δf Vs \sqrt{H} plots. A comparison of this data with Fig. 3.5 shows that at 65 K for example k_p^{\parallel} is approximately an order of magnitude higher than k_p^{\perp} . In a clean Bi-2223 crystal, the parallel field dynamics would be dominated by the response of the Josephson vortices between the Cu-O planes to rf currents which are always in the ab -plane. This is a strong intrinsic pinning configuration and therefore must result in large values of k_p^{\parallel} . In the present case however, there is $(\lambda_{ab}/\lambda_c \sim 1/10)$ [50] and the sample is in a platelet form with the thickness to width ratio $\sim \lambda_{ab}/\lambda_c$. Due to this geometric effect, some penetration of the rf field from the edges of the specimen is expected [83]. The induced screening currents which in this case will be of a Josephson character flowing across the Cu-O planes would slide the vortices between the planes. This is a weak pinning configuration and hence would result in lowering of the overall k_p^{\parallel} . The observed small anisotropy $k_p^{\parallel}/k_p^{\perp}$ is perhaps due to this easy slide of vortices between the planes which is caused by

the penetration of the rf field from the edges of the sample. This effect will be further augmented by the misorientation between the platelets which lowers the anisotropy considerably

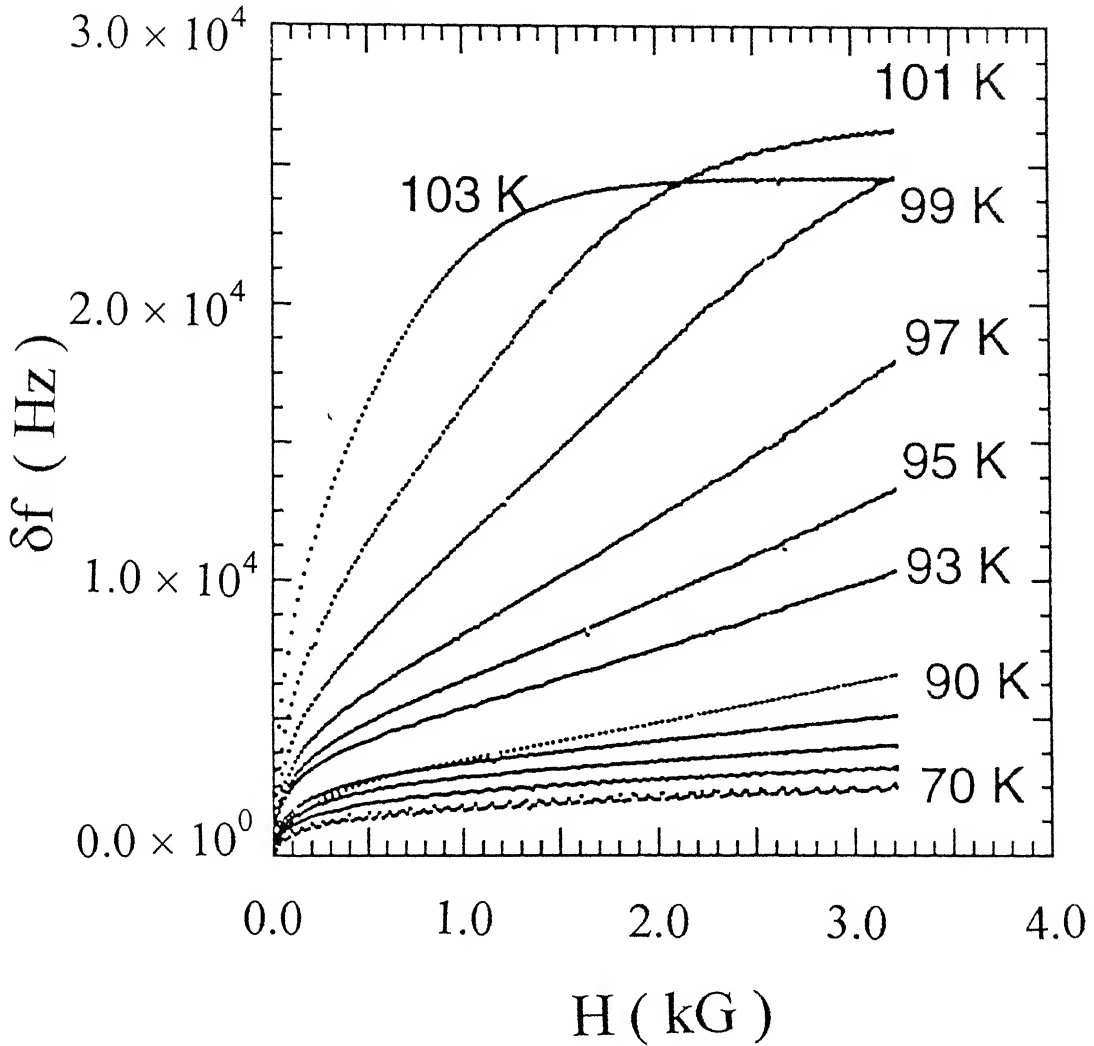


Figure 3.6 Variation of frequency shift δf as the external field (oriented parallel to the plane of the tape) is increased from zero to 3200 Gauss. Temperatures of measurement are listed in the Figures.

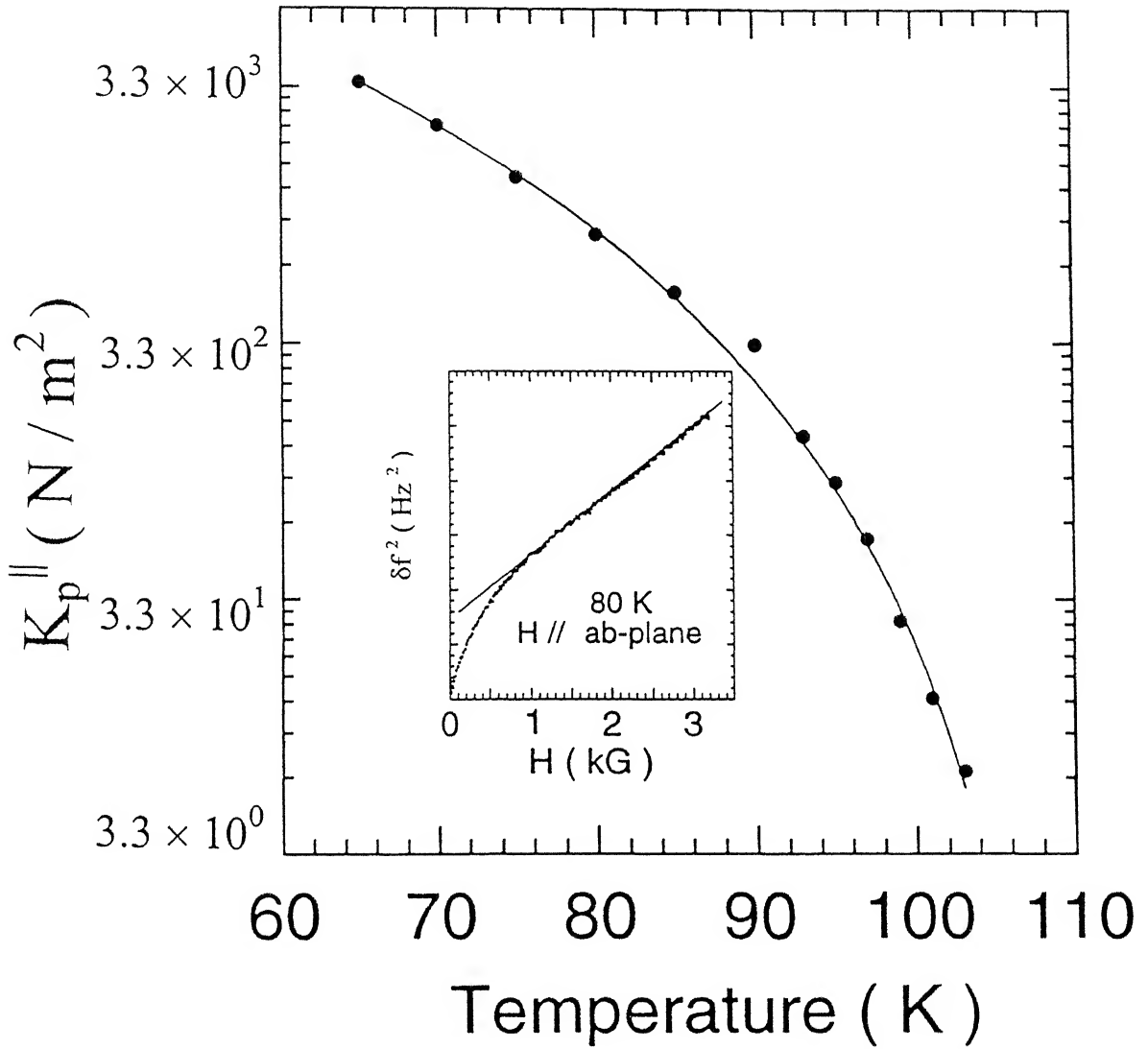


Figure 3.7 The pinning force constant k_p^{\parallel} deduced from the data of Fig. 3.6 is plotted as a function of temperature. Inset shows the range of field over which δf^2 shows a $\sim H_{dc}$ dependence at 80 K.

3.2.4 Angular dependence of the rf response

Fig. 3.8 plots the frequency shift at 85 K when the magnetic field is increased at a fixed orientation with respect to the plane of the tape. The δf at a given field approaches rapidly the value for $\theta = 90^\circ$ ($\mathbf{H} \parallel \mathbf{c}$ configuration) on increasing the orientation of the dc field with respect to the plane of the tape. The data of Fig. 3.8 and similar measurements performed at 95 and 99 K yield the value of $k_p(\theta)$, the pinning constant at a given field orientation θ . Fig. 3.9 shows the variation of $k_p^\perp/k_p(\theta) \sin \theta$, for non-zero values of θ .

The angular dependence of k_p deduced from Fig. 3.9 when incorporated in the expression for the pinning penetration depth leads to,

$$(\delta\lambda(\theta))^2 = \phi_0 B(\theta) / \mu_0 k_p(\theta) \sim (B(\theta) \sin(\theta)) / k_p^\perp \quad (3.4)$$

This shows that the penetration of rf currents at a tilted dc field is essentially decided by the component of the field normal to the ab-plane and the pinning force constant for inplane motion of the vortices. In defect-free single crystals of Bi-2212, flux lockin effects have been seen for small orientations of the field with respect to the ab-plane [84]. In this regime the penetration of the rf field into the sample would be entirely due to the oscillatory motion of the Josephson vortices. At higher tilts, when the lock-in state is destroyed, one would expect the normal component of the field to control the dynamics. The response of the system such as J_c , susceptibility, magnetization, power dissipation etc. scale with the normal component of the field. The present result is not only consistent with this picture, it also shows directly that the pinning force on the vortices formed on the Cu-O planes (2D pancake vortices) controls the dynamics of the system.

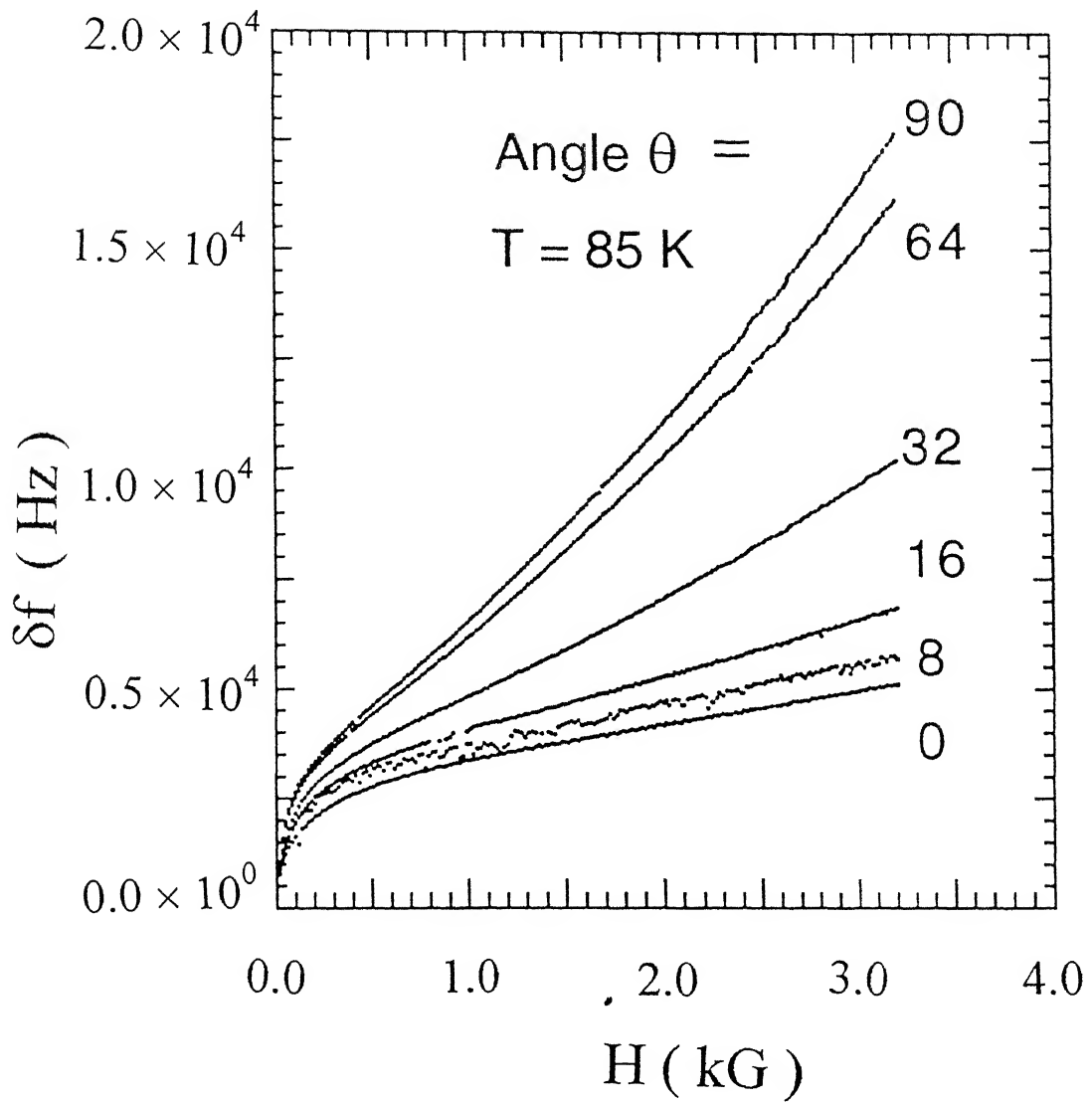


Figure 3.8 Magnetic field dependence of the penetration depth measured at 85 K for different value of the angle (θ) between the dc field direction and the plane of the tape.

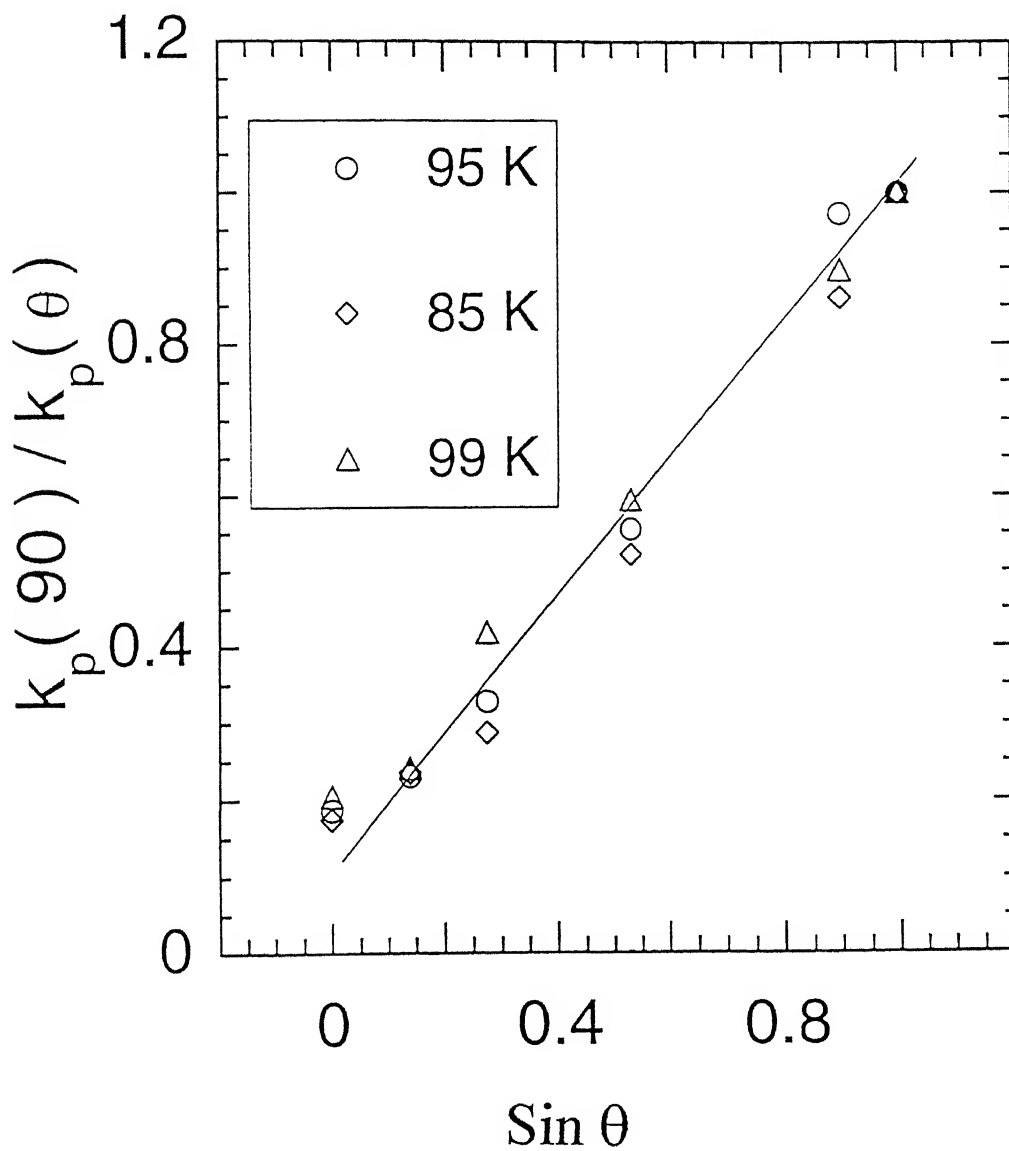


Figure 3.9 Variation of $k_p^\perp/k_p(\theta)$ with $\sin \theta$ for measurements performed at 85, 95 and 99 K. Solid line in the Fig. is a guide to the eye.

3.3 Pinning enhancement with heavy ion irradiation

3.3.1 Temperature dependence of the frequency shift

Fig. 3.10 compares the temperature dependence of the resonant frequency, after background correction, for an unirradiated sample and two samples irradiated at the field equivalent fluence of 0.5 Tesla and 3 Tesla. We note that the transition temperature T_c , defined as the temperature at which δf is 50 % of its normal state value, for the unirradiated and 0.5 T irradiated samples is the same (112.1 K). However, the T_c of the 3 T irradiated sample is decreased to 107.5 K. This is a consequence of radiation damage of the superconducting material at the higher values of fluence. It has been found that the depression of T_c is related with fluence ϕ as; $\Delta T_c / \phi = 3 \times 10^{-11} \text{ K (ions / cm}^2 \text{)}^{-1}$. The observed drop of T_c is consistent with this result [85]. In the inset of Fig. 3.10 we show the influence of a dc field on the temperature dependence of frequency shift in the unirradiated and 0.5 T irradiated samples. At 1 kG field applied normal to the plane of the sample, the onset of T_c is lowered by ~ 20 K for the unirradiated sample. In the 0.5 T sample however, the shift of T_c is only 7.5 K. This is a clear indication of strong flux pinning introduced by columnar defects.

3.3.2 Field dependence of frequency shift

Fig. 3.11a and 3.11b show some typical field scans for the 0.5 T and 3 T samples respectively at various temperatures with the dc field oriented perpendicular to the plane of the platelet. The y-axis of the Figures has been normalized by dividing δf (H, T) with the maximum zero-field frequency shift between 10 K and 120 K. Only the data taken during increasing field sweeps are shown for clarity. This normalization procedure has been adopted to take into account slight variation in the volume of the unirradiated and irradiated samples.

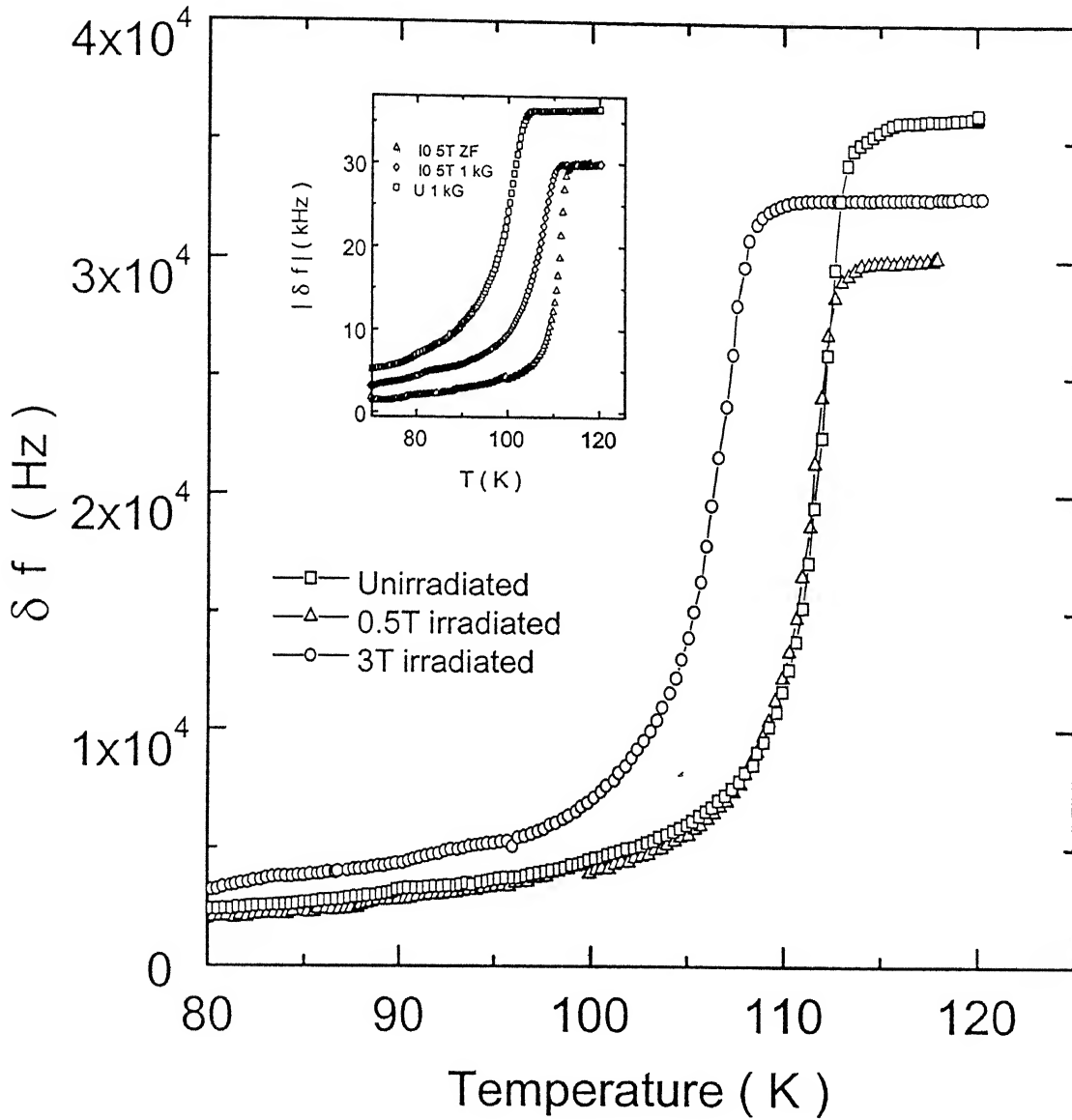


Figure 3.10 Frequency shift δf plotted as a function of temperature at zero field for the unirradiated, 0.5 T and 3 T irradiated samples. Inset shows broadening of the transition when 1 kG field is applied perpendicular to the plane of the 0.5 T irradiated sample and the unirradiated sample.

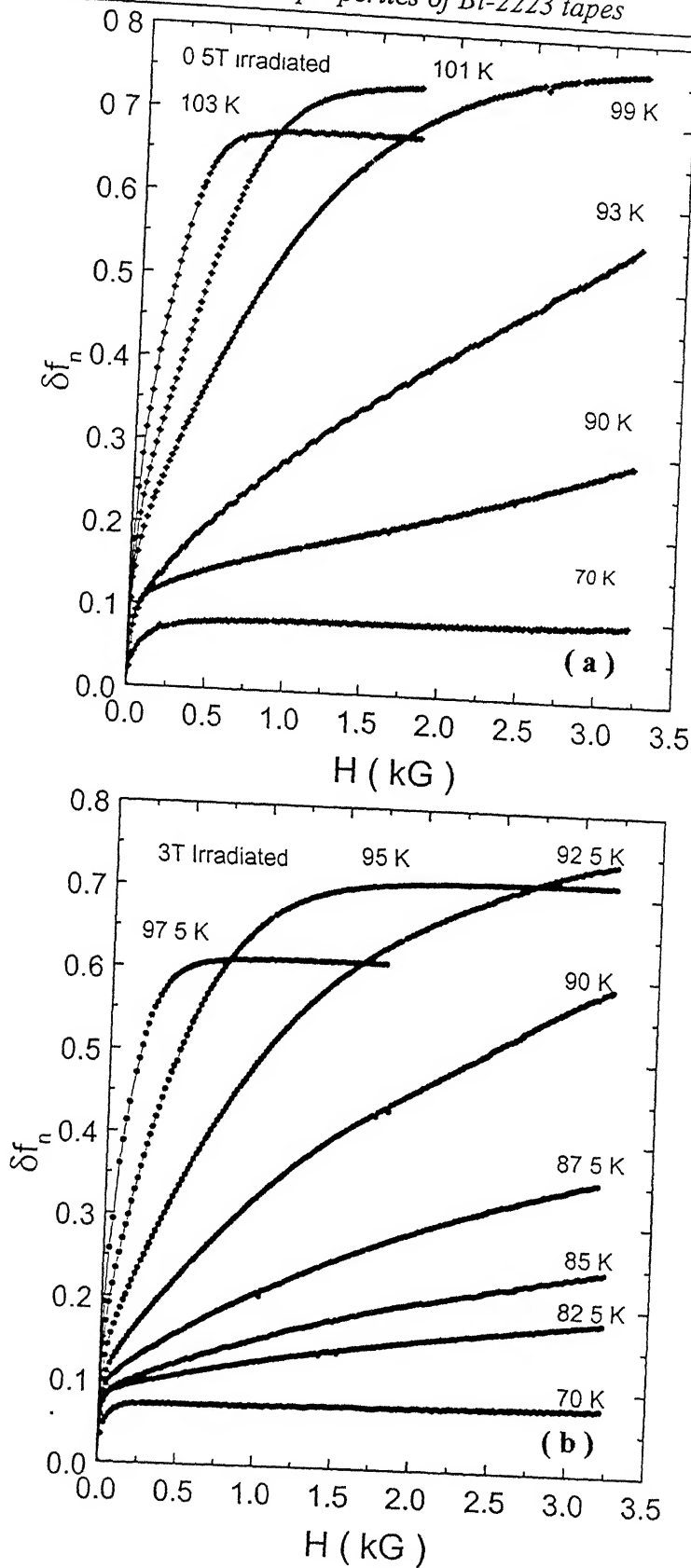


Figure 3.11 (a, b) The normalized frequency shift $\delta f_n = (f(H,T) - f(0,T)) / (f(0,T_c) - f(0,10\text{ K}))$ Vs. the external dc magnetic field applied perpendicular to the plane of the platelet; a) 0.5 T irradiated sample b) 3 T irradiated sample.

The shape of the curves reveals the extent of rf field penetration into the sample at several temperatures. As in the case of the unirradiated samples, the sharp rise of $\delta f(H, T)$ with increasing field at temperatures closer to T_c marks a quick penetration of the rf field into the sample. The saturation of δf in scans taken at $T \geq 92.5$ K for the maximum dc field of 3.2 kG indicates full penetration of the rf field. At lower temperatures however, the δf does not saturate. It is clear that at these temperatures and fields, the rf currents enter only partially into the volume of the sample.

In Fig. 3.12, we plot $\delta\lambda$ vs. \sqrt{H} at 80 K for the unirradiated, 0.5 T irradiated and 3 T irradiated samples assuming the calibrated value for $G = 2.2 \text{ \AA/Hz}$. It is noticed that for the same value of temperature, maximum dc field and the nearly identical sample volume, the total $\delta\lambda$ in the unirradiated sample is an order of magnitude higher. This shows the effects of strong flux pinning at the columnar defects in the irradiated samples that limits the penetration of rf field into the sample. As in the case of unirradiated samples, the rf response of the samples with columnar defects also shows three distinct regimes of field penetration. Further, samples with columnar defects show an anomalous hysteresis characterized by a higher $\delta\lambda$ in the field increasing branch of the curve. Moreover the hysteresis appears at the field H_2^* which we have identified as the irreversible field. The inverted hysteresis seen here signifies a deeper penetration of the rf field into the sample while increasing the dc field as compared to the situation when the dc field is being brought back to zero. Similar hysteretic effects have been seen earlier in the measurements of microwave losses in granular samples of $\text{YBa}_2\text{Cu}_3\text{O}_7$ and Bi-2212 superconductors [22,86]. The hysteretic aspects will be discussed in detail in Chapter 5.

While there is no detectable hysteresis in the 80 K data for the unirradiated sample, a clearly identifiable H_2^* does suggest some semblance of weak pinning in the intragranular regions. The intragranular pinning gains strength on lowering the temperature and, indeed, the field scans for unirradiated samples at $T \leq 45$ K show a distinct hysteresis. The observation of hysteretic effects in irradiated samples at temperature as high as 80 K indicate strong flux pinning effects of the columnar defects. The other manifestations of pinning in the irradiated sample are a considerably lower value of the total frequency shift, the higher H_2^* and a lower slope between H_1^* and H_2^* as compared to the unirradiated sample. It is however, important to note that these

parameters do not change significantly when we compare the 0.5 T and 3 T irradiated samples

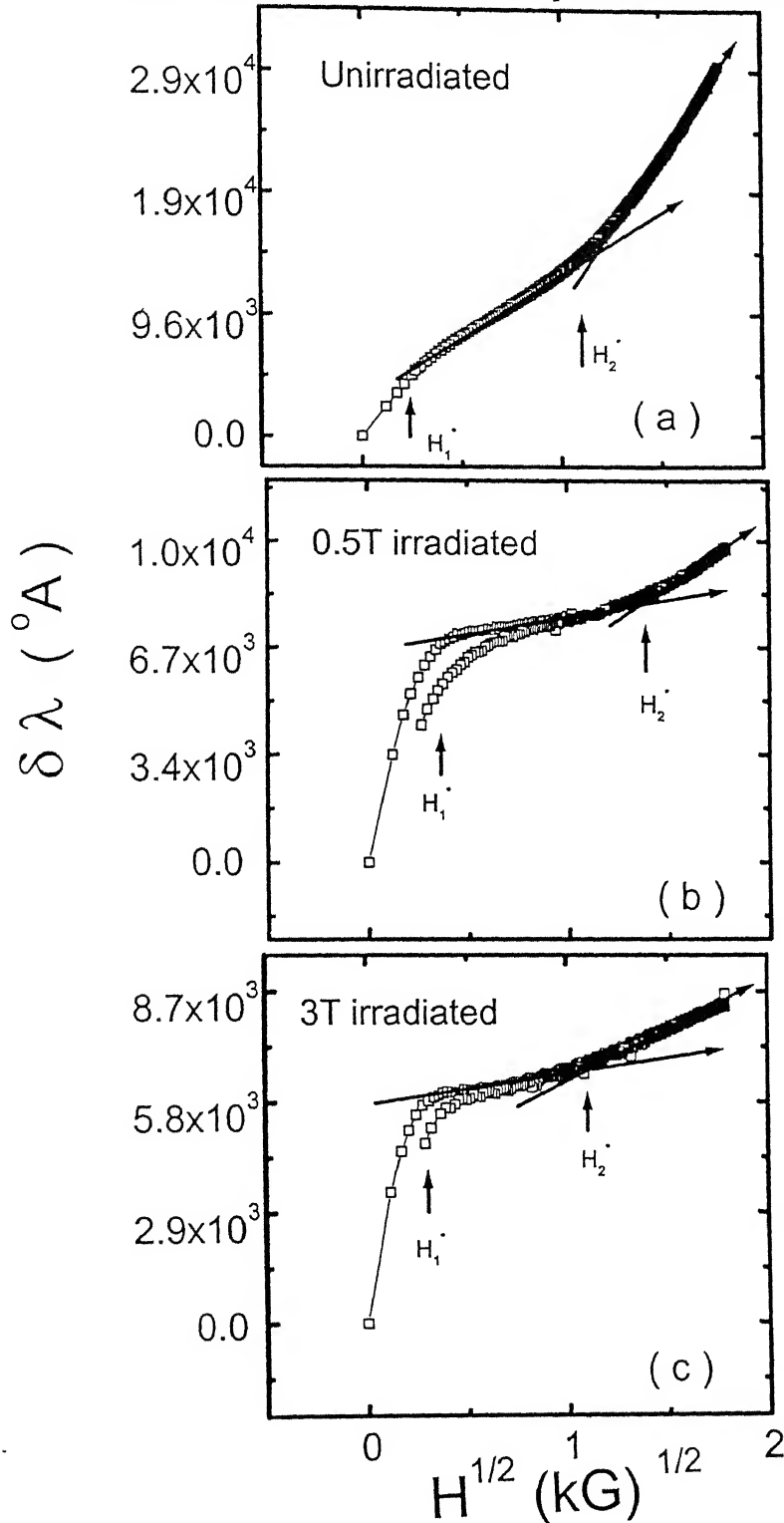


Figure 3.12 (a, b, c) $\delta\lambda$ Vs. $\sqrt{H_{dc}}$ at 80 K for the a) unirradiated , b) 0.5 T irradiated and c) 3 T irradiated samples. The magnetic field, H_{dc} , is perpendicular to the plane of the platelet in all cases. The change in slope is marked by critical fields H_1^* and H_2^* (see text).

The angular dependence of frequency shift during field scans at 80 K and 90 K for the 0.5 T irradiated sample are shown in Fig. 3.13a and 3.13b respectively. We notice that at 80 K the penetration depth for $\theta = 90^\circ$ is lower than the penetration depth when $\theta = 54^\circ$ since for $\theta = 90^\circ$, the flux lines become parallel to the axis of the columnar defects. This is a clear indication of anisotropic pinning at the columnar defect sites. However at 90 K, thermal fluctuations dominate over anisotropic pinning and the localization of vortices at the defect sites is suppressed. The data in Fig. 3.13 supports the interpretation that magnetic vortices behave as 3D lines at elevated temperatures due to correlated disorder. These aspects are discussed in chapter 4 by angular scan experiments.

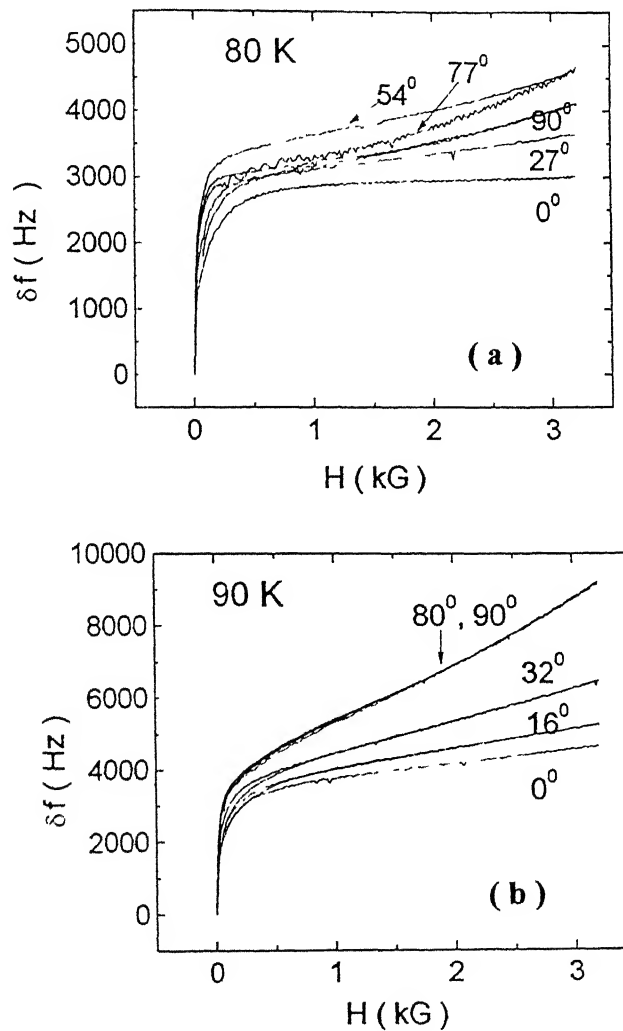


Figure 3.13 (a, b) Field scans at various angles with respect to ab plane for the 0.5 T irradiated sample at a) 80 K and b) 90 K.

The intergranular and intragranular parts of $\delta\lambda$, and the flux flow regimes are well separated by H_1^* and H_2^* respectively. Therefore the intragranular pinning force constant k_p and the viscosity coefficient η can be calculated from the data. The absolute values of these quantities, however, depend sensitively on the choice of the constant G which couples δf and $\delta\lambda$. In order to avoid possible errors in the calculation of η and k_p due to the uncertainty in G , the relative changes in these parameters as a result of pinning due to the CDs are calculated. The relative changes are independent of G because all samples had nearly the same shape and volume. Moreover, all measurements were done using the same coil.

The variation of intragranular pinning constant k_p normalized with respect to G^2 for unirradiated sample and the samples irradiated at 0.5 T and 3 T fluence is shown in Fig. 3.14. A significant enhancement in pinning is seen in the two irradiated samples. At a reduced temperature of ~ 0.75 , the k_p value is higher by an order of magnitude when compared with the k_p of the pristine specimen. Fig. 3.14 also shows a higher pinning force constant for 0.5 T sample compared to 3 T irradiated sample. The ratio of the J_{co} for heavy ion irradiated (J_{co}^{CD}) and unirradiated (J_{co}^{UN}) is given as $(k_p^{CD} / k_p^{UN}) \times (r_p^{CD} / r_p^{UN})$. If we assume that r_p^{CD} is the diameter of the columnar defects ($\sim 70 \text{ \AA}$) [6], and r_p^{UN} the diameter of oxygen vacancy related defects ($\leq 10 \text{ \AA}$), an enhancement of \sim two orders of magnitude is expected in J_{co} after irradiation. This compares well with the typical increase in the transport J_c of heavy ion irradiated tapes seen in this range of temperature and field [56].

In Fig. 3.15, we show the variation of the coefficient of viscosity for the three samples discussed above. The flux flow viscosity η of these samples show a behaviour similar to that of k_p before irradiation and after irradiation. However, at our measurement frequency (3.2 MHz) which is much too small compared to the depinning frequency ($> 50 \text{ GHz}$), some of the enhancement in η after irradiation could be attributed to the stronger flux pinning in samples with the CDs.

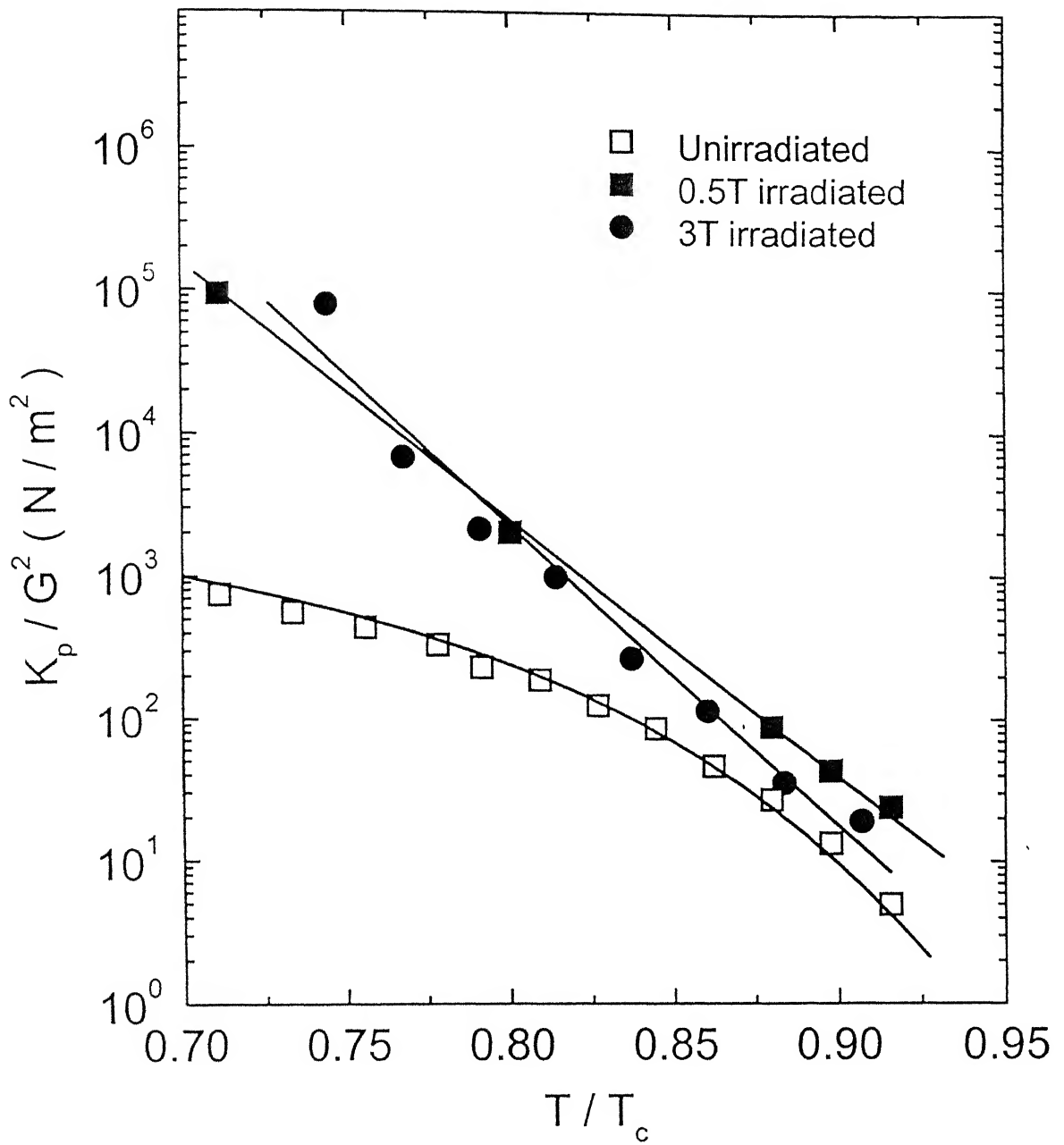


Figure 3.14 The pinning force constant k_p / G^2 deduced from $\delta\lambda$ Vs. $\sqrt{H_{dc}}$ data between field H_1^* and H_2^* is plotted as a function of reduced temperature for the unirradiated and two irradiated samples.

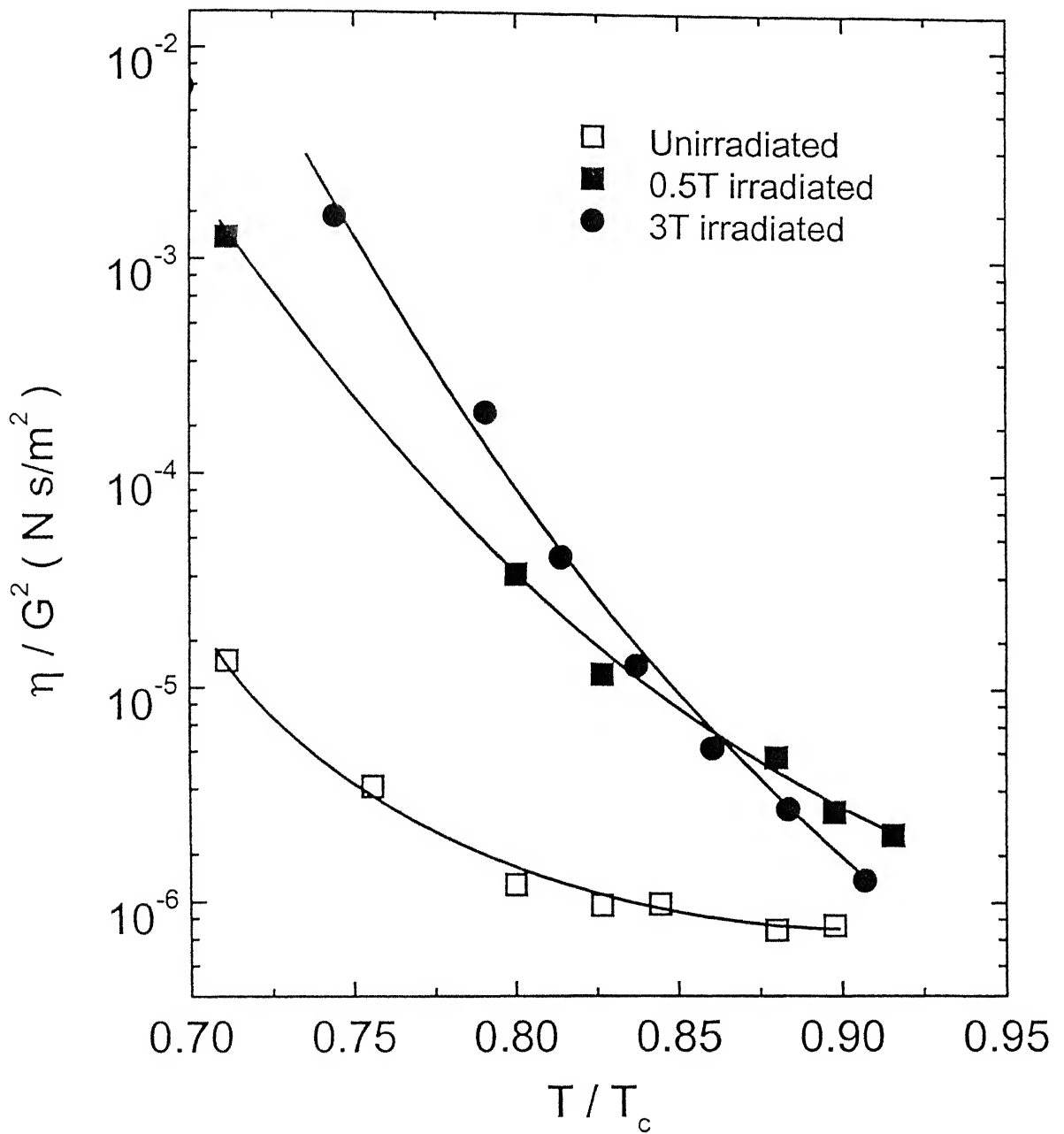


Figure 3.15 The coefficient of viscosity η / G^2 is plotted Vs. Temperature.

3.4 Summary

The measurements of rf penetration depth in the unirradiated platelets of Ag-sheathed Bi-2223 superconductor performed as a function of magnetic field, temperature and the orientation between field and plane of the platelet distinctly establish the granularity of these samples. At higher temperatures, three distinct regimes of field exist where the response changes from grain boundary - to - intragrain - to - flux flow dominated with the increasing field strength. The pinning force constant k_p^\perp , k_p^\parallel and $k_p(\theta)$ for dc field oriented \perp , \parallel and at angle θ with respect to the plane of the platelet respectively have been calculated. The angular dependence of the k_p explicitly shows that for $\theta > 0$, the penetration of the rf field into the grains is essentially controlled by the motion of 2D pancake vortices. The pinning force constants for H perpendicular and H parallel to ab plane show significant increase with heavy ion irradiation. The experiments confirm anisotropic pinning at fields much smaller than matching field B_ϕ . Even in the low field single vortex regime where the vortex - vortex interaction is negligible, the Labush parameter does not follow an angular dependence of the type $k_p^\perp \sim k_p(\phi) \sin \phi$ implying 3D vortices parallel to linear defect direction at temperature as high as 80K for the 0.5 T irradiated sample.

Chapter 4

Angle selective vortex dynamics in HfBi-2223

4.1 Introduction

In the previous chapter we noted that the temperature dependence of rf field penetration resembles the behaviour of flux flow resistivity in layered superconductors. A considerable attention has been devoted to the angular dependence of flux flow resistivity and critical current density in anisotropic superconductors. Above the irreversibility line, the resistivity shows a sharp drop when the field is brought into alignment with the layers [87]. Similar reduction has also been observed when the external field is made parallel to the twin planes or the heavy ion irradiation induced damaged tracks [88-94]. The reason for the maximum suppression of flux flow resistivity at parallel alignment is the largest gain in the pinning energy. Confining ourselves to the case of pinning by linear tracks and twin planes (correlated disorder), it is noticed that the onset of anisotropic pinning on cooling the system through the flux liquid state depends sensitively on the relative number of defects and vortices and is most pronounced when

$B \leq B_\phi$. While the flux flow resistivity becomes zero below the irreversibility temperature, the presence of anisotropic pinning at lower temperature can be seen through the measurements of critical current density. In YBCO, where the Cu-O superconducting planes are much more coupled compared to bismuth and thallium based compounds, it is seen at very low temperatures. Recent study by Hardy et al. confirms that in the case of YBCO, the J_c enhancement for the field direction parallel to the columnar tracks is always greater than the enhancement perpendicular to the track for $T > 30$ K [93]. Magnetization measurements by Civalc et al. on YBCO also showed unidirectional enhancement in J_c for temperature as low as 5 K [9]. Similar studies were undertaken by Thompson et al. in heavy ion irradiated Bi-2212 crystals. Although a large increase in pinning energy was found between the unirradiated and irradiated crystals, the increase was primarily isotropic [91]. It was concluded that extremely weak interlayer coupling between the CuO_2 planes leads to pancake like vortices with negligible line tension and this is the reason for lack of directionality in the angular dependence of J_c . Similar conclusion were drawn by Budhani et al. from transport measurement on heavy ion irradiated Tl-2212 thin films [89].

We have seen in Chapter 1 that the rf response in the mixed state is directly related to pinning and flux flow properties. In this Chapter we present our results of precision angle dependent measurement of rf response on unirradiated and heavy ion irradiated Bi-2223 tapes. The angular variation of ac penetration depth in BiSCCO tapes derives its contribution from the misorientation of platelets in addition to the factors related to the interlayer coupling between the CuO_2 planes. The rf response shows the characteristic cusp associated with anisotropic pinning down to $T \simeq 60$ K for the 0.5 T irradiated sample. However, in the vortex liquid state close to T_c , a threshold field is required to see the cusp. We interpret these results in the framework of the Bose glass theory [12] applied to highly anisotropic superconductors such as Bi-2212 [95].

4.2 Results and discussion

4.2.1 Angular studies on unirradiated sample

We first discuss the angular dependence of rf response in unirradiated Bi-2223 samples. Fig. 4.1 shows the frequency shift δf as a function of the orientation between the dc field and ab plane of the platelet while the temperature and field strength were held constant. All the scans are taken in the dynamic mode by rotating the dc magnet in steps. Here,

$$\delta\lambda = G |(f(H, T, \theta) - f(H, T, \theta = 0^\circ))| \quad (4.1)$$

Such measurements performed at several temperatures reveal that the minima at 0° and 180° become sharper at higher temperatures and stronger fields. At very low temperatures (~ 15 K) this feature is significantly suppressed and no reproducible data could be obtained due to dominance of history effects. In a clean single crystal sample, the width of the peak at parallel configuration is linked to the strength of Josephson coupling between the layers. At low temperature the interlayer coupling becomes stronger and the anisotropy is reduced. On the other hand at high temperature and strong fields, the coupling is suppressed and the angular scan displays strong anisotropy. In a tape sample, however, the extent of misorientation between the platelets will tend to reduce the anisotropy. A perfectly random polycrystalline sample will of course show an isotropic angular dependence. The pronounced minima for $\theta = 0^\circ$ and 180° in the case of the Bi-2223 tape samples (Fig. 4.1), suggest that the platelets are well oriented. The observation is consistent with X-ray diffraction measurement of inplane alignment.

To elucidate this point more clearly, Figure 4.2 displays a comparison between unirradiated Bi-2212 and Bi-2223 at 70 K and 1.750 kG. The intrinsic pinning peak for Bi-2212 is very sharp and assuming misorientation between the platelets to be same for both Bi-2212 and Bi-2223, this result reflects the higher anisotropy and lower coupling between the superconducting layers in Bi-2212.

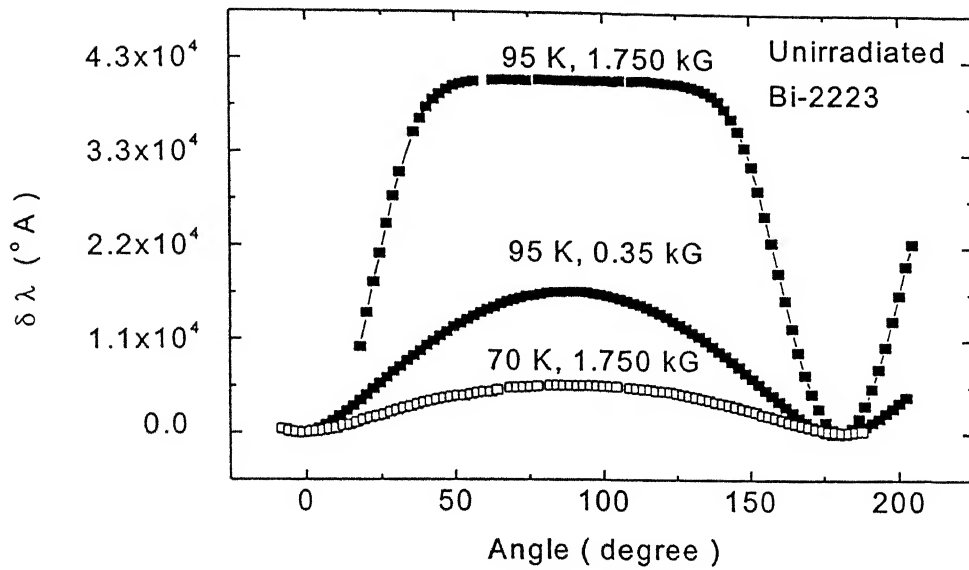


Figure 4.1 Angular scans for unirradiated Bi-2223 showing superior pinning characteristics when the external field is parallel to the planes. The effect is most prominent at high temperature and strong fields.

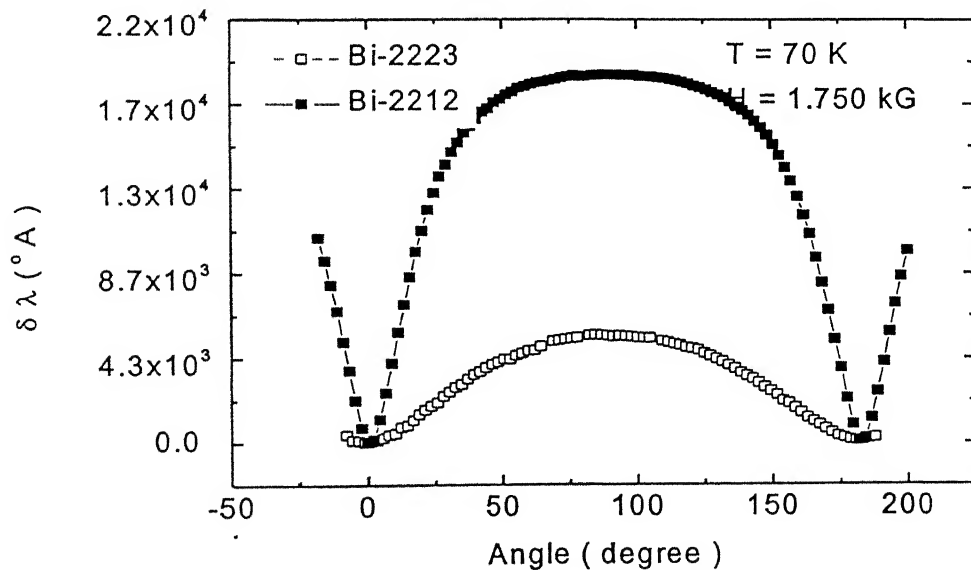


Figure 4.2 A comparison between Bi-2212 and Bi-2223. The temperature and external magnetic field are held constant at 70 K and 1.75 kG. A sharper peak at 0° and 180° for Bi-2212 shows that the peak width is essentially dependent on interlayer coupling.

4.2.2 Angular studies on 0.5 T irradiated sample

The rf measurements on the irradiated samples show a strong suppression of the penetration depth when the external dc field is brought into alignment with the columnar defects. This behaviour is similar to the resistivity minima seen in heavy ion irradiated epitaxial thin films of $\text{Ti}_2\text{Ba}_2\text{CaCu}_2\text{O}_8$ superconductors [89]. Figure 4.3 shows the angular scans of rf penetration depth for the 0.5 Tesla irradiated sample at several temperatures. The data taken at 90 K show a distinct dip in $\delta\lambda$ when the angle between the direction of dc field and the axis of CDs is zero that is $\theta = 90^\circ$ with respect to ab plane. In addition to this feature, we see two pronounced minima at $\theta = 0^\circ$ and 180° . These correspond to the situation when the external magnetic field becomes parallel to the Cu-O planes. The behaviour of the dip at angle parallel to defects has many similarities with the data on Tl-2212 films and $\text{Bi}_2\text{Sr}_2\text{CaCu}_2\text{O}_8$ crystals. On lowering the temperature, it first grows and then broadens suggesting an increase in the accommodation angle for columnar defect pinning at lower temperatures. This distinctive feature of pinning by CDs finally disappears at temperature $T < 60$ K. A comparison of this result with $\theta = 90^\circ$ field scans taken at several temperatures suggests that the angular selectivity is strictly a feature of the temperature regime where J_c is low. This observation compares well with the angular dependence of J_c in Tl-2212 films where a J_c enhancement at $\theta = 0$ was seen only when the overall critical current was low [96].

Another illuminating feature of the angular dependence of $\delta\lambda$ emerges when the temperature is held constant and angular scans are taken at several values of the applied dc field. The results of such measurements at 80 K on 0.5 T sample are shown in Figure 4.4. At 100 G field, when defects outnumber vortices by a significant margin, and no dip in $\delta\lambda$ at $\theta = 90^\circ$ is seen. On increasing the field to 500 G, a chaotic behaviour is seen near $\theta = 90^\circ$ which seems to be a precursor to the development of a well-defined cusp at 1 kG field. The cusp then continues to appear at 1.5 and 2.5 kG fields.

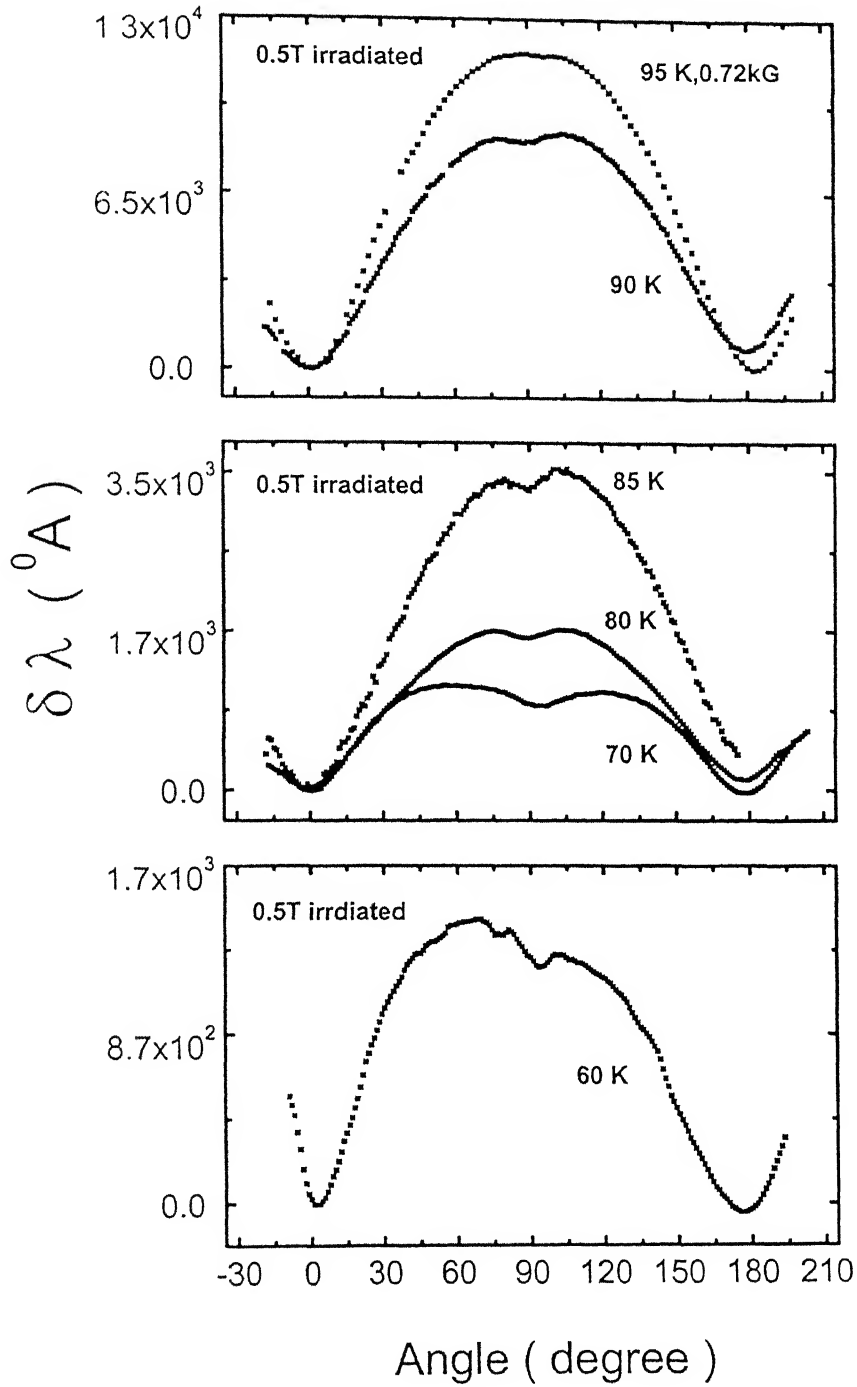


Figure 4.3 Angular scan of $\delta\lambda$ for the 0.5 T irradiated sample with $H = 2$ kG at several temperature except at 95 K where $H_{dc} = 0.72$ kG. The dip at $\theta = 90^{\circ}$ marks anisotropic pinning due to columnar defects.

While the angle dependent response shown in Figure 4.3 and Figure 4.4 is a manifestation of the statistics and dynamics of vortices in this highly layered superconductor, the data also allow to comment on the degree of misorientation between the platelets of these tape samples. For a fixed angle of irradiation, the randomness in the orientation of platelets translates into a randomness between orientation of columnar defects and crystallographic c-axis. The net effect of this would be a much larger accommodation angle for the tape samples. Experimentally this is determined as the half of the angular width between the rf field penetration maxima. Figure 4.5 shows θ_a for the 0.5 T irradiated sample as a function of normalized temperature. The accommodation angle is nearly same as that of Bi-2212 [94]. This observation indicates a well oriented platelet sample. The accommodation angle reflects the maximum field tilt angle at which columnar defect pinning is effective. At low temperatures, the accommodation angle is very large and at still lower temperatures the angular selectivity gives way to isotropic pinning enhancement.

This disappearance of the anisotropic pinning feature at high temperatures and low - field has a different origin. It appears that in this regime of temperature and field, the liquid of pancake vortices remains decoupled. A coupling between the pancakes sets in only when the field exceeds a threshold value. Such a transition from a decoupled pancake vortex liquid to a coupled pancake vortex liquid on increasing the field has been seen in Josephson plasma resonance measurements on heavy ion irradiated Bi - 2212 single crystals. This issue is discussed in section 7.5 where we discuss the effect of heavy ion irradiation on more anisotropic Bi-2212 tapes.

4.2.3 Angular studies on 3 T irradiated sample

It is important to know how would the unidirectional anisotropy seen in the previous section change in the extremely dilute limit of flux density ($B \ll B_\phi$). The higher defect density alters the scenario mainly in three ways; i) the creep rate would increase because under the Bose glass scenario the existence of many unoccupied defects promotes variable range hopping of vortex segments, ii) the high density of defects also reduces

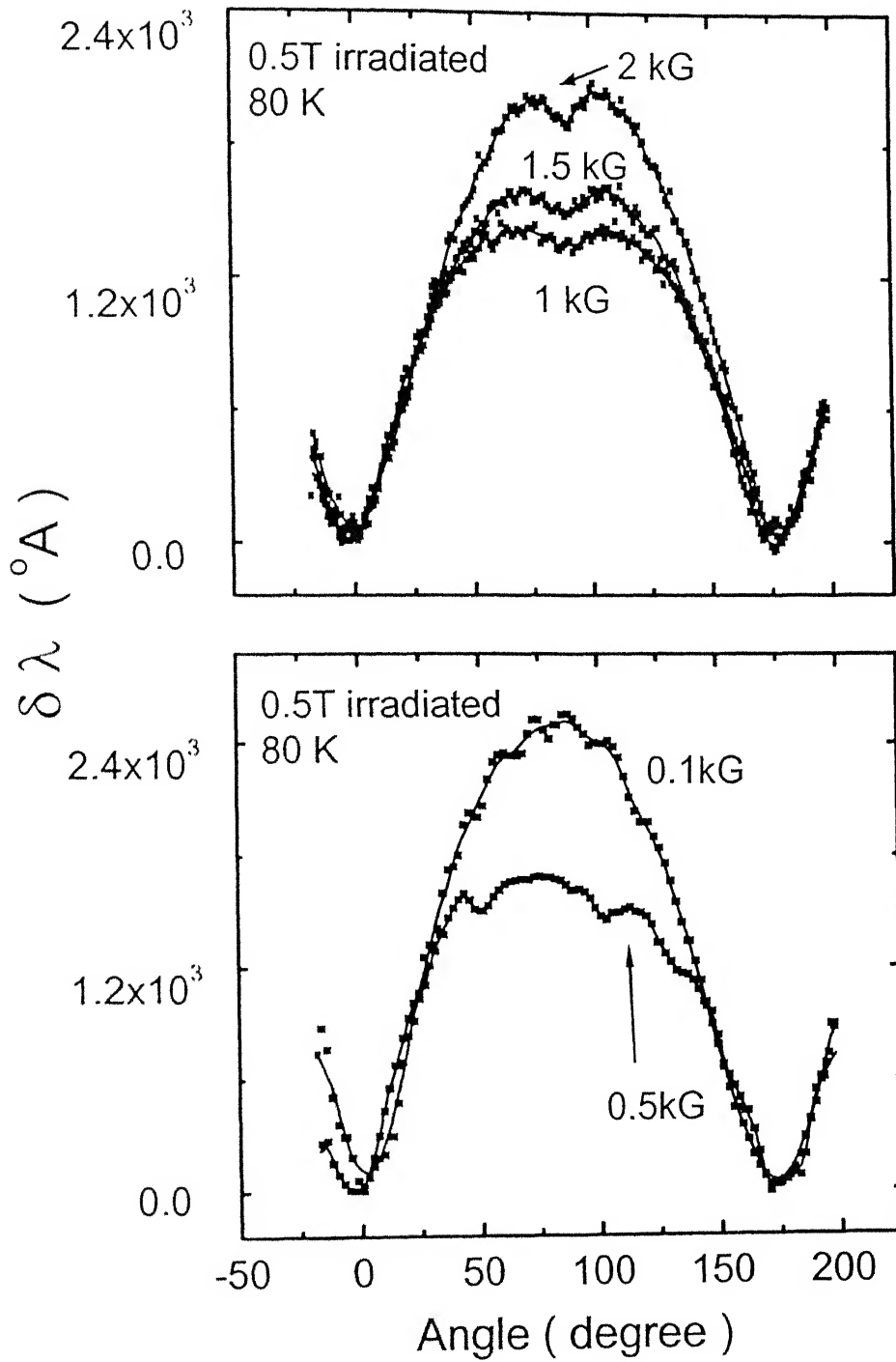


Figure 4.4 Angular scan of $\delta\lambda$ for the 0.5 T irradiated sample at 80 K for several dc field values. The dip at $\theta = 90^{\circ}$ is not present at 100 G. Only at field greater than 500 G, strong pinning at defect sites is observed.

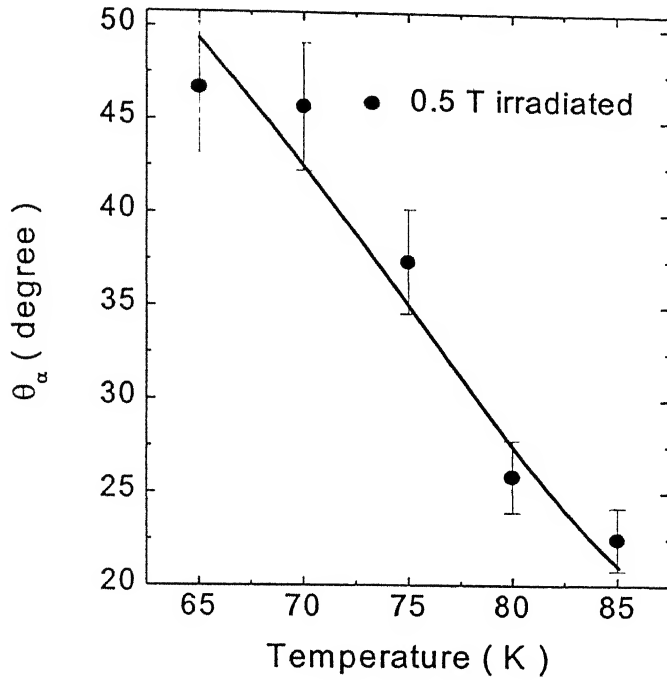


Figure 4.5 Variation of accommodation angle with respect to temperature for the 0.5 T irradiated sample. The data reflects negligible misorientation between the platelets.

the T_c due to radiation damage of the superconductor as compared to the 0.5 T case and iii) the accommodation angle is enhanced when the vortices are outnumbered by defects. While a quantitative comparison between the 0.5 T and the 3 T irradiated sample is difficult because of the possible difference in sample volume, in the following we highlight some distinctive features of vortex dynamics in 3 T irradiated sample.

The interplay of intrinsic and extrinsic pinning, as the temperature is decreased, is displayed in Fig. 4.6a-f. At low temperatures (< 45 K), like the 0.5 T irradiated case, the penetration depth in the vicinity of $\theta = 90^\circ$ does not show a cusp (Fig. 4.6a). Also the penetration depth at $\theta = 0^\circ$ and $\theta = 180^\circ$ is not the same. While the absence of cusp indicates that there is no anisotropic pinning, the second effect is due to the fact that the magnetic state of the sample at $\theta = 0^\circ$ and $\theta = 180^\circ$ is not the same due to history effects.

As shown in Fig. 4.6a the decrease in rf field penetration at 45 K occurs at $\theta \sim 60^\circ$ even though the cusp at $\theta = 90^\circ$ is absent. This means that pinning due to the defect site is present at 45 K for the 3 T irradiated sample and the accommodation angle is $\sim 30^\circ$. At low temperature, the vortex line tension is large and we can expect strong lock in effects at the defect sites. As the field angle deviates from the parallel to defect direction configuration, the vortices do not track the external field and this is a possible explanation for the absence of the cusp and the shift of the peak to $\theta \sim 60^\circ$. As the temperature is increased to 55 K a competition between weakening interlayer coupling and lock-in properties take place. The onset of unidirectional pinning can be observed at angles parallel to defect direction. This means that for the 3 T irradiated sample, anisotropic pinning at the columnar sites is not absent at 45 K and therefore we conclude that the pancake defect interaction in Bi-2223 is intermediate between YBCO and Bi-2212.

In a narrow window of temperature around 70 K a situation develops where the minimum due to columnar defects is lower than the two minima due to the intrinsic interlayer coupling. This type of behaviour is not seen 0.5 T irradiated sample and the result is directly related to the difference in accommodation angle for the two samples. It has been shown by Budhani et al. that θ_a is large for the case where vortices are outnumbered by defect sites. This is the situation for the 3 T sample in our field regime. A larger accommodation angle implies the dominance of defect sites even at orientations very close to the ab plane. Therefore the dip due to intrinsic pinning is restricted only to a small angular zone. As the temperature increases further, the accommodation angle decreases and the expected $\sin\theta$ dependence for intrinsic pinning is observed. This result suggests greater suppression of anisotropy at the higher density of defect sites. Lastly, Fig. 4.7 shows the angular scan at $T \geq 90$ K for the 3 T irradiated sample. At $T = 95$ K T_c is less by 5 K compared to 0.5 T sample) and 1.75 kG the cusp is still observed unlike the case for the 0.5 T irradiated sample.

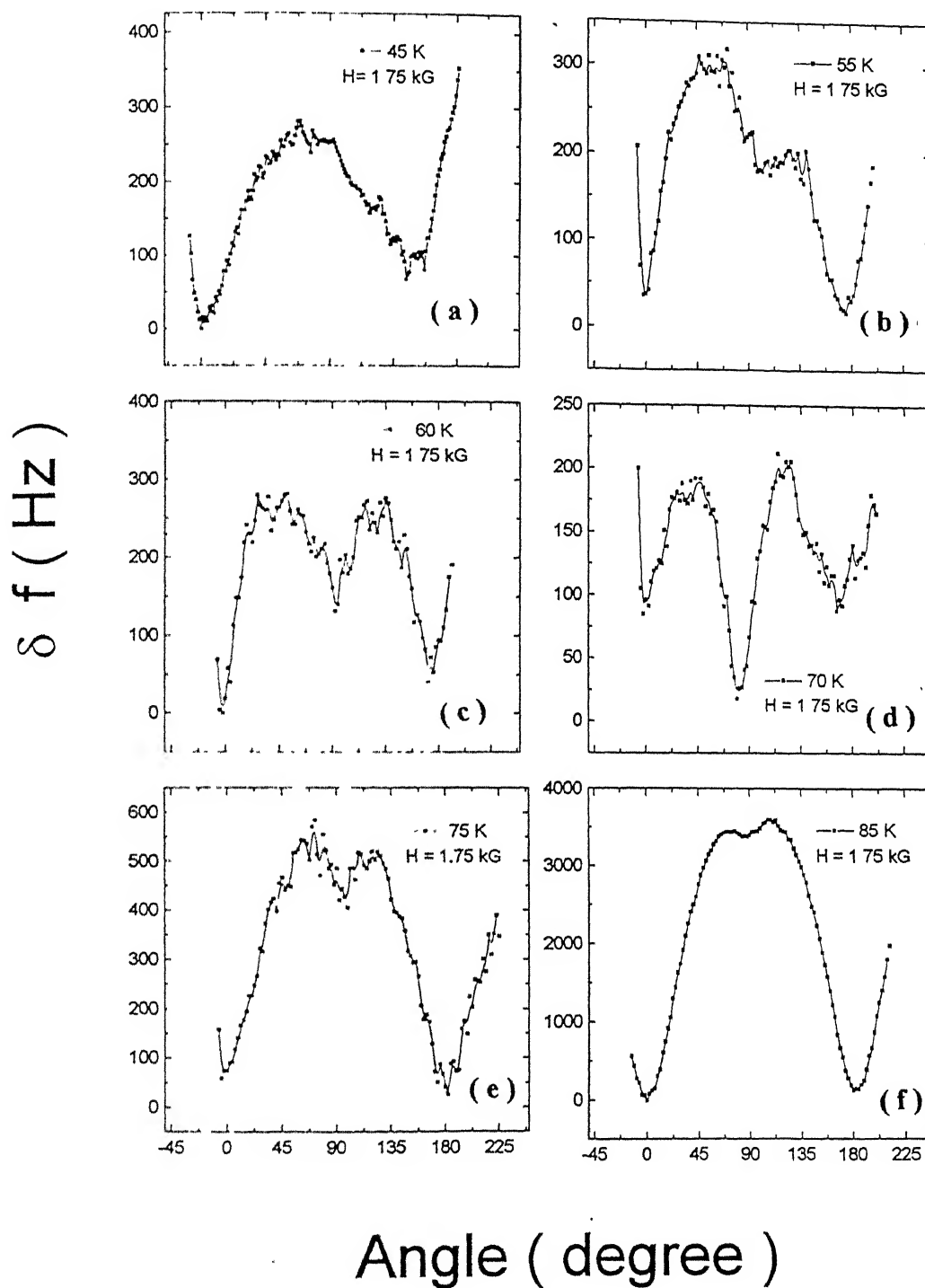


Figure 4. 6 (a-f) Angular scans of 3 T irradiated sample at different temperatures. The dc field is 1.750 kG for all the scans.

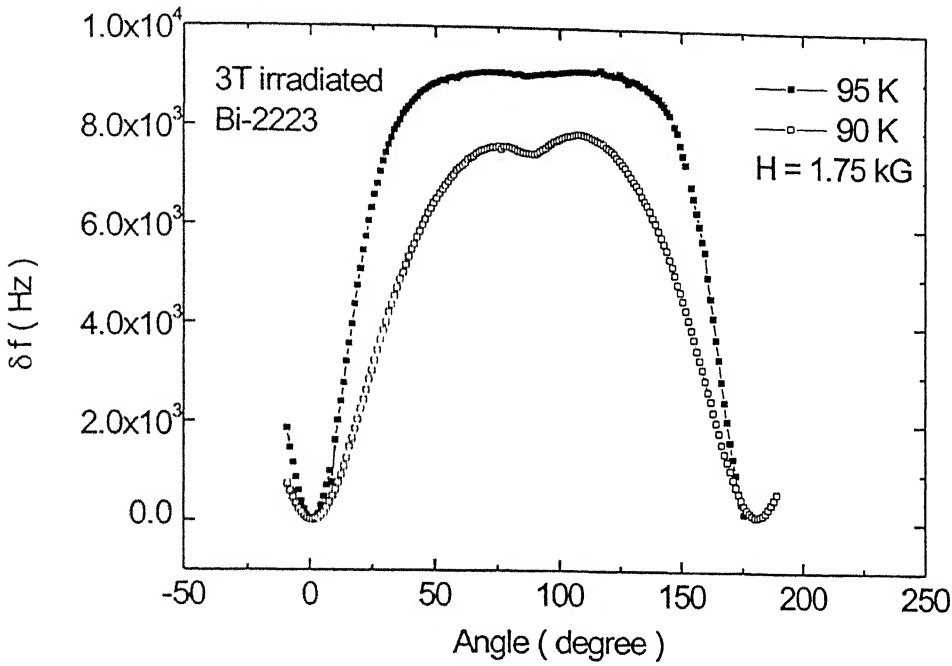


Figure 4.7 Angular scan of 3 T irradiated sample at high temperature.

4.3 Models for angular selectivity in HfBi anisotropic superconductors

The important question is how the interlayer coupling between pancake vortices is improved by the presence of columnar defects in the high temperature regime and the apparent loss of selectivity at lower temperatures. The fluctuation of Josephson - coupled pancake vortices in layered superconductors in the presence of columnar defects have been analyzed by Koshlev, Le Doussal and Vinokur [95] under the framework of the Bose glass theory (KLV). The magnetic field and defect density regime investigated in the present case corresponds to the dilute limit of KLV where intraplane interaction between the pancake vortices are negligible. KLV argue that the localization effects of columnar defects are governed by the effective pinning potential which is characterized by a large dip in close vicinity of the column and a $1 / r^2$ tail far from the defect. While

the small distance dip dominates the dynamics at lower temperatures, the large distance tail is relevant at higher temperatures. At low temperatures, the critical nucleus for vortex activation is a single pancake where as in the regime where long distance tail of the interaction becomes relevant, the delocalized vortex is a string of coupled pancakes. Thus, there exist two crossover temperatures T^* and T^{**} ($T^* < T^{**}$) which characterize the temperatures above which single pancakes and strings of pancakes respectively are delocalized by thermal activation. It is clear that in the regime of string delocalization one would see anisotropic pinning characterized by a cusp in the rf response when the dc field is made parallel to the defect. The regime of single pancake activation, on the other hand, will be isotropic. For Bi - 2212, the estimated values of T^* / T_c and T^{**} / T_c are 0.64 and 0.7 respectively. Since the Ginzburg - Landau mass anisotropy in Bi-2223 is lower compared to Bi-2212, it is expected that the string like behaviour in this compound will evolve at lower temperatures as seen in much less anisotropic compound $\text{YBa}_2\text{Cu}_3\text{O}_7$.

Two alternative explanations for the angular selectivity of the response are also available in the literature. Hardy et al. argue that the anisotropic pinning due to the columnar defects disappears due to a significant enhancement in pinning of pancakes at lower temperatures [93]. Such rigidly pinned pancakes do not track the direction of the external field when it is rotated towards the CD. Fukumoto et al. conclude from their J_c measurements on irradiated tapes of Bi-2223 that the loss of angular selectivity is due to the enhanced pinning by irradiation induced point defects [56]. Drost and Coworkers [97] have conducted torque and SQUID magnetometry on HII Bi-2212 single crystals to find out whether a redistribution of pancakes over columnar defects which ultimately destroys the angular selectivity occurs with the increasing pinning strength of the columns. Their measurements, however, show that as the field is tilted away from the c-axis direction, which is also the direction of columns, the perpendicular field component H_z and hence the number of pancake vortices decreases monotonically. This observation rules out any redistribution of pancakes over columnar defects. The contribution of point defects to isotropic pinning at lower temperatures can be significant. Irradiation of Bi-2212 tapes with 120 MeV O^{7+} ions which produce point defects results in an order of magnitude isotropic enhancement in critical current density at 20 K [17]. However, the number density of point defects produced by heavy ion irradiation depends sensitively on

the energy of the projectile. Whether 6 GeV lead ions would produce enough point defects is not clear yet.

4.4 Summary

The isothermal angular scans at constant dc field bring forth many interesting aspects of vortex localization and defect-vortex interaction in Bi-2223 through the rf penetration depth experiment. The interactions between weakly coupled pancake vortices and columnar defects in this technologically important layered superconductor show that the response is intermediate between that of YBCO and Bi-2212 which represent two extreme limits of anisotropy in cuprate superconductors of $T_c > 77$ K. In the 0.5 T irradiated platelets, anisotropic pinning at the columnar defect site is not observed for $T \leq 60$ K. At temperature very close to the transition temperature, the unidirectional pinning is not observed in the irradiated samples below some threshold field value. The results are understood in terms of the KLV theory [95] and the model proposed by Hardy et al. [93].

Chapter 5

Granularity and hysteresis in Bi-2223 tapes

5.1 Introduction

The silver sheathed bismuth based cuprates provide the model systems to study the dynamic behaviour of magnetic vortices in granular superconductors over a wide range of temperature. In this chapter, the granularity and the resulting anomalous hysteretic behaviour of the rf penetration depth in the Bi-2223 tape samples are discussed. It is important to note that these effects are not seen in dc magnetization measurements where the magnetization shows a normal hysteretic behavior and scales with the size of the sample suggesting a uniform flow of screening currents in the material [37,40,41,98,99]. The data from our experiments, however, bear similarity with the irreversibility seen in microwave loss data on bulk polycrystalline samples of $\text{YBa}_2\text{Cu}_3\text{O}_7$ and $\text{Bi}_2\text{Sr}_2\text{CaCu}_2\text{O}_8$ superconductors [22,23,25]. There are two anomalous features in the data i) the penetration depth in the decreasing field branch is lower than in the increasing branch

and μ), a minimum in $\delta\lambda$ is seen before H goes to zero. The anomalous hysteresis in $\delta\lambda$ is understood to be due to the high mobility of the magnetic flux trapped at the grain boundaries in these otherwise highly c-axis oriented samples. At low temperatures, the viscosity of the magnetic flux in the intergranular fluxon regions is orders of magnitude smaller than the viscosity in the grains and consequently the high frequency response is primarily due to flux-flow like behaviour in the intergranular regions. The range of temperature over which the hysteresis is seen depends on the strength of intragranular pinning. While in the as grown samples it is confined to $T \leq 0.4 T_c$, samples with columnar defects show the anomaly upto $T \cong 0.8 T_c$. The observed behaviour has been understood quantitatively on the basis of the two-level critical state model of Ji, Rzechowski, Anand and Tinkham proposed by them for microwave field penetration in inhomogeneous superconductors.

5.2 Results and discussion

5.2.1 Hysteresis in Unirradiated Bi-2223

In Fig. 5.1 we show the rf penetration depth $\delta\lambda$ when the external dc field oriented perpendicular to the plane of the platelet is swept at a constant rate from zero to 3.2 kG and then brought back to zero for the unirradiated Bi-2223 sample. At temperatures $T > 0.6 T_c$ ($T_c \sim 112$ K), the forward and reverse branches of the curve superimpose, thus indicating a reversible behaviour. For $0.4 T_c \leq T \leq 0.6 T_c$, the rf response is reversible in the high field region and shows a small irreversibility below a critical field. However, for $T < 0.4 T_c$, the response is purely irreversible. The hysteresis observed here has two characteristic features; first it is opposite in sign to the hysteresis seen in magnetization measurements, and secondly, the rf penetration depth $\delta\lambda$ in the decreasing field branch goes through a minimum at a well defined field H_{mr} , and then crosses the increasing field branch and finally results in a non-zero remanence.

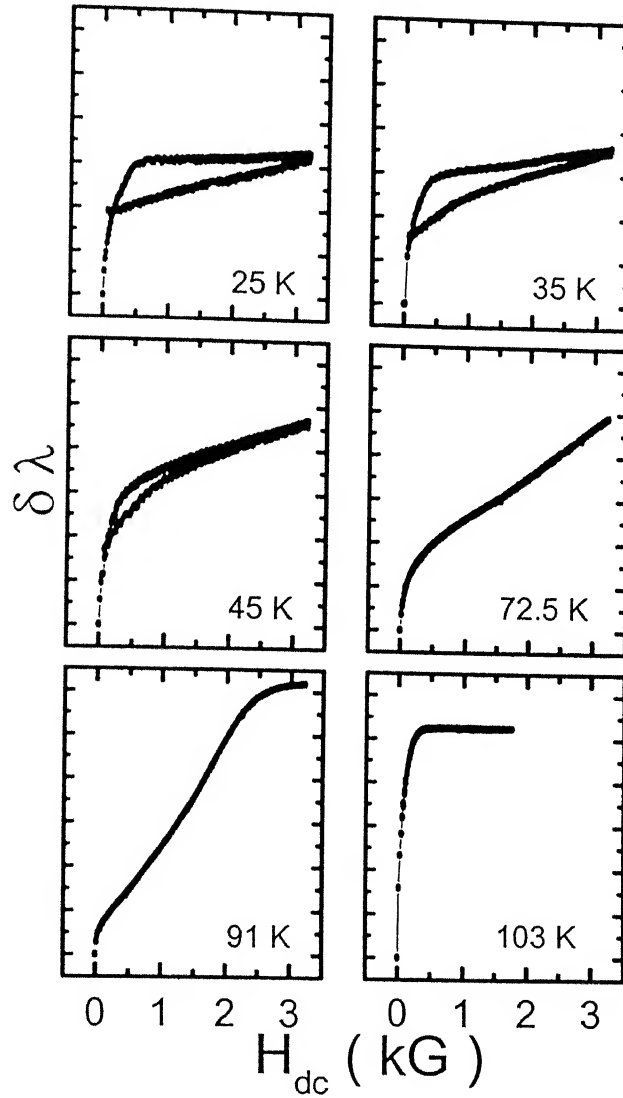


Figure 5.1 The rf penetration depth $\delta\lambda$ Vs. H_{dc} for the unirradiated sample at several temperatures. The y - axis varies from 0 to 7150 Å ($\delta f = 3250 \text{ Hz} = n$) for 25 K and 35 K data. The scans at 45 K, 72.5 K, 91 K and 103 K are scaled by 2n, 3n, 10n and 10n respectively.

These features are clearly demonstrated in Fig. 5.2 where we plot the variation of the rf frequency shift as the external field is cycled between zero and a given field $\pm H_{\max}$ at 15 K. Several loops have been traced by increasing H_{\max} to 3200 Gauss. A hysteretic phenomenon of similar nature has also been seen in the measurements of transport J_c on Bi-2223 tapes [100]. This anomalous hysteresis characterized by a butterfly like shape and large remanence is a typical feature of granular superconductors and has its origin in the relative mobility of intergranular and intragranular vortices.

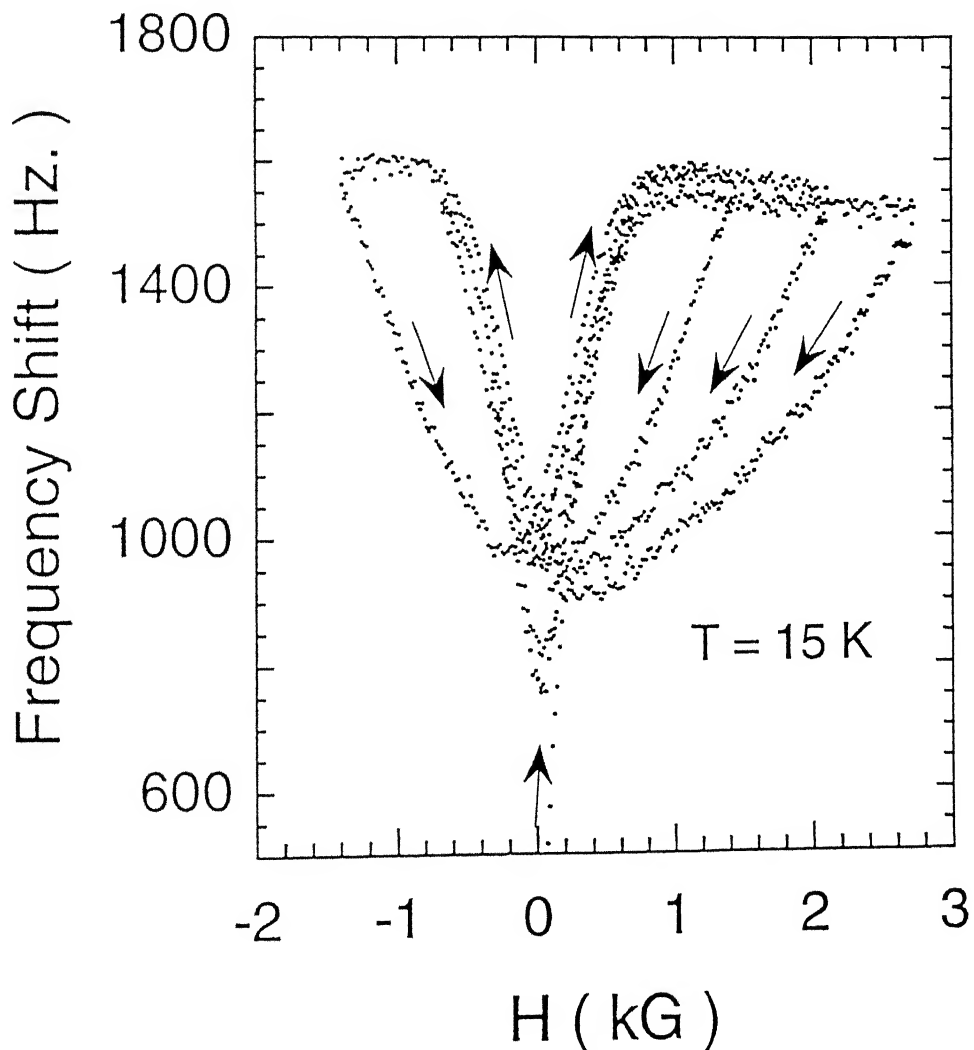


Figure 5.2 Anomalous behaviour of the hysteresis in the measurement of frequency shift Vs. H_{dc} for the unirradiated sample. Data have been shown for both increasing and decreasing field sweeps for lower values of H_{\max} and only the positive side for $H_{\max} = 2$ kG and 2.7 kG. Direction of the magnetic field was perpendicular to the plane of the tape.

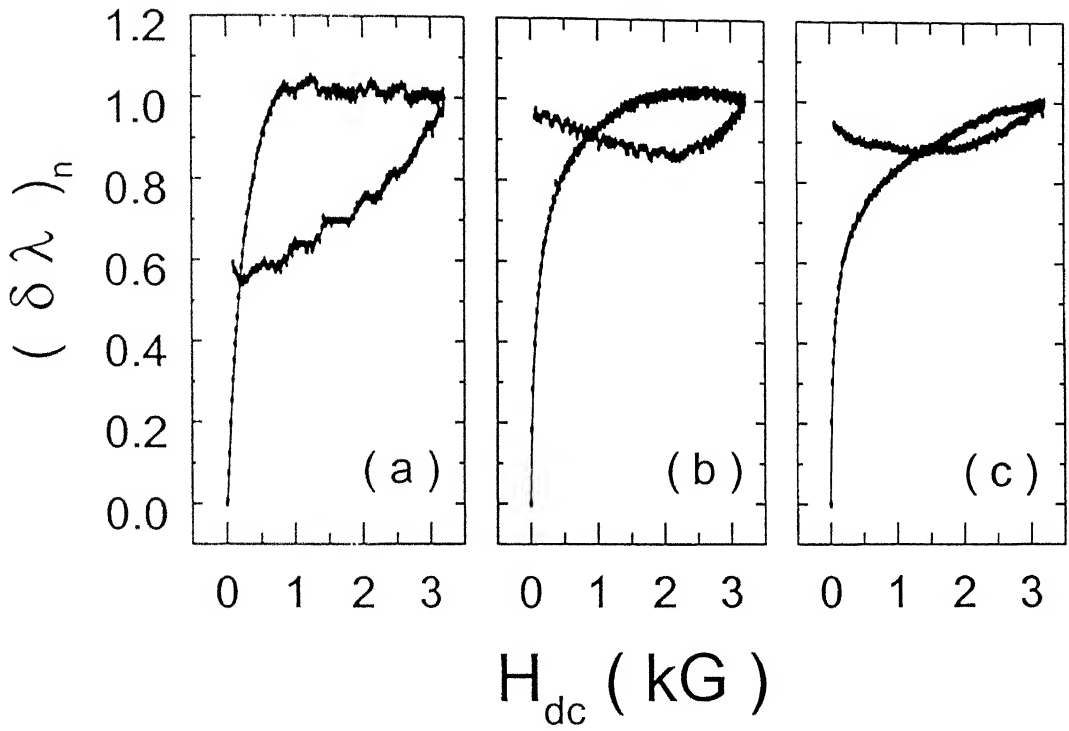


Figure 5.3 The normalized rf penetration depth $(\delta\lambda)_n$ Vs. H_{dc} for (a) unirradiated, (b) 0.5 T irradiated and (c) 3 T irradiated sample at 15 K and H_{dc} perpendicular to the plane of tape.

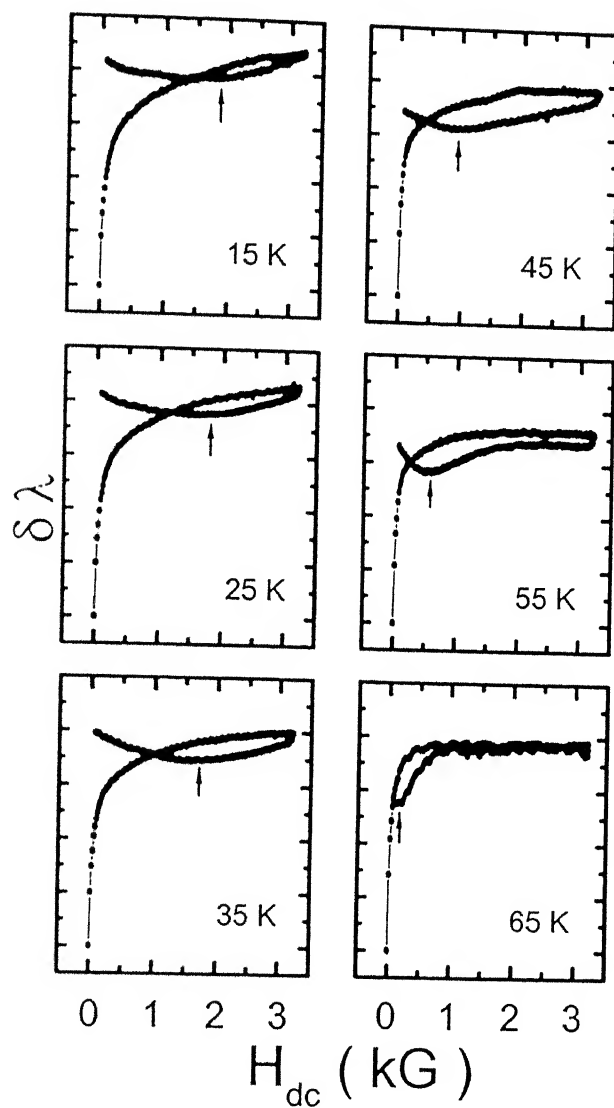


Figure 5.4 The hysteresis of the 3 T irradiated sample at several temperatures. The external field is perpendicular to tape plane. For all the plots y - axis varies from 0 to 5500 Å.

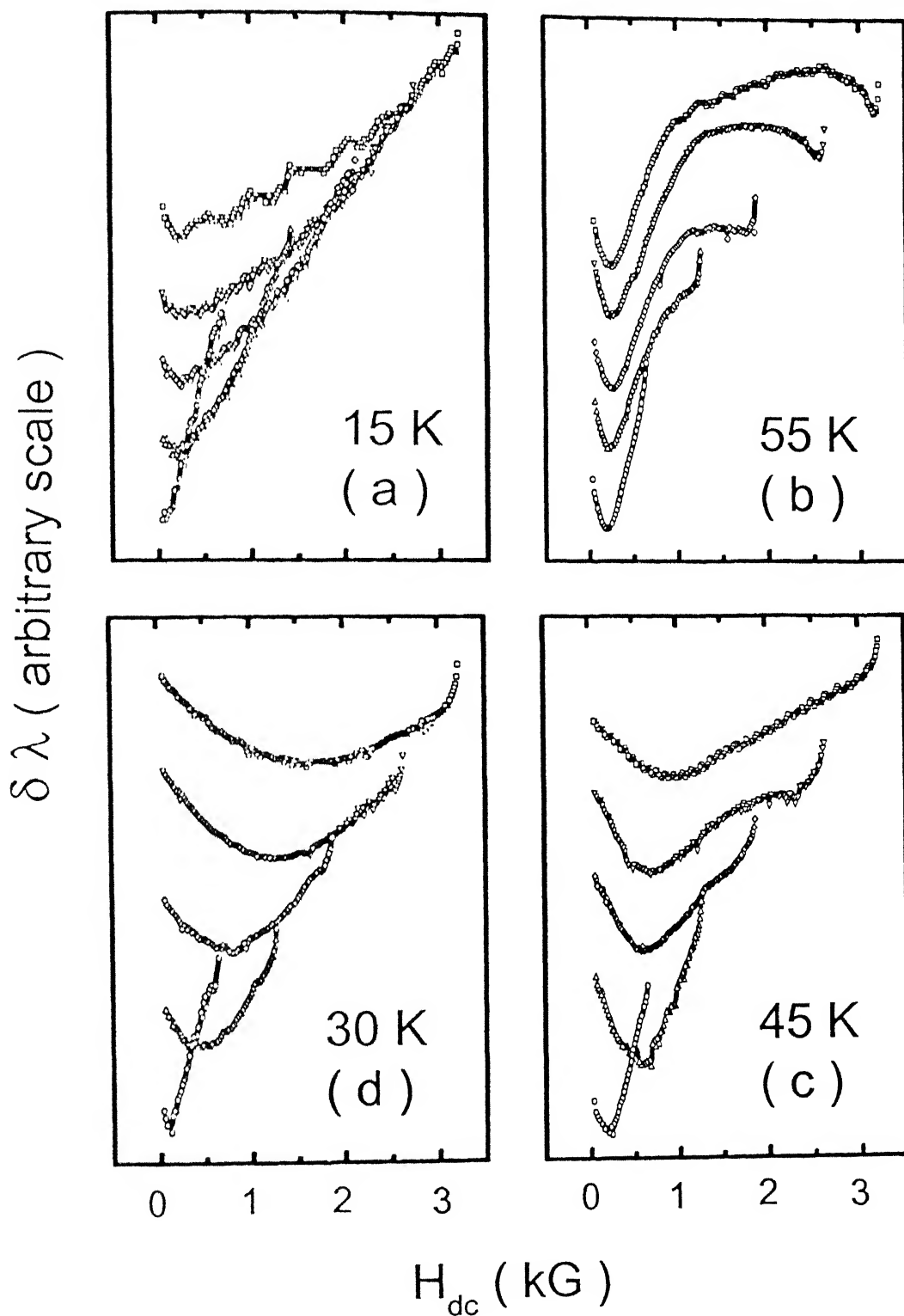


Figure 5.5 Reverse branch of hysteresis for successive values of maximum external dc field. (a) unirradiated sample at 15 K, and (b), (c), and (d) for 3 T irradiated sample measured at 55, 45 and 30 K respectively.

5.2.3 Ji, Rzchowski, Anand and Tinkham (JRAT)model

The penetration of a dc field in a homogeneous type - II superconductor with pinning can be understood in the framework of Bean Critical State model [101]. The model assumes a field independent macroscopic peak current density (J_c) that flows in the superconductor in order to screen the field. In an ac magnetization experiment the current density can take only $\pm J_c$ value in the flux penetrated region and zero everywhere else. Drawing analogy from the response of a ferromagnetic material, the flux profiles in the Bean model lead to hysteretic losses due to trapped vortices during a field cycle. Figuratively this is shown in Fig. 5.6a.

Granular materials, however, are characterized by two distinct critical current densities; a large J_{cg} inside the grains and a much weaker J_{cj} in the grain boundary region. This leads to a large difference in the mobility of intergrain and intragrain vortices. In fact, the irreversibility seen in our rf measurement is analogous to the behaviour of microwave losses in granular samples of $YBa_2Cu_3O_7$ and $Bi_2Sr_2CaCu_2O_8$. Ji, Rzchowski, Anand and Tinkham (JRAT) [25] have analyzed microwave losses in $YBa_2Cu_3O_7$ ceramics and a model granular structure consisting of Nb-Cu-Nb proximity junction arrays in the framework of a two - level critical state model. The basis of this model is a large difference in the mobility of intergrain and intragrain vortices. The mobility of intergranular vortices being higher by orders of magnitude, the microwave loss at low fields in granular superconductors is mainly due to the flux flow in the intergranular regions. The Bi-2223 silver sheathed tapes have a unique granular microstructure consisting of c-axis oriented colonies of platelets [37,39,98]. The dominant Josephson links in the structure are; (a) the (001) twist boundaries and (b) the a and b-axis boundaries which are formed at the interface between to platelets. In the following, we examine the applicability of the JRAT model to the rf penetration depth of Bi-2223 platelets in the weak and strong pinning regimes.

The rf penetration depth $\delta\lambda$, in general, derives contributions from depairing effects on superconducting carriers and the dynamic vortex response which leads to pinning and flux flow penetration depths [19]. However in a maximum Lorentz force configuration ($J_{rf} \perp H_{dc}$) as used here, the vortex contribution is expected to dominate

the response. Further, in the flux flow regime, the rf penetration depth can be associated directly with the flux flow resistivity [20,24]. It is therefore reasonable to apply the JRAT model to the present case. In this framework, the anomalous hysteresis develops because the freely moving grain boundary fluxons are influenced by the grain pinned fluxons through demagnetization effect. When the field increases from zero, the local field in the weak link region is more than the external field because of flux expulsion by the diamagnetic grains. The high mobility of the intergranular flux leads to a sharp rise in microwave absorption. As the external field exceeds H_{c1} of the grains, the intragranular part of absorption starts to develop and the intergranular absorption saturates. The latter may even decrease slightly as some of the excess intergranular flux will have a tendency to enter the grains because of the lowering of the diamagnetic barrier. When the field is retraced, fluxons easily move out from the weak links and the local field in the intergrain region becomes lower than the field during the increasing cycle. Therefore, the reduced rf absorption leading to anomalous hysteresis.

The broad features of the hysteresis for the unirradiated sample are consistent with this picture. The sharp rise and subsequent saturation of $\delta\lambda$ in Fig. 5.1 is indicative of a rapid penetration of magnetic flux into the grain boundaries. The boundaries may even get oversaturated due to the demagnetization effects of the grains. However, once the flux starts penetrating the grains, the change in rf penetration depth is decided essentially by the mobility of intragranular vortices which being much smaller at low temperatures, does not change $\delta\lambda$ significantly. In fact a discernible negative slope of the curve (see Fig. 5.3, curve 'a') suggests diffusion of the excess flux from the intergranular regions into the grains as discussed above. The saturation effects are, however, gradual in the intermediate temperature range and not seen for $T > 25$ K due to a sharp rise in the mobility of intragranular vortices as well. In the case of irradiated samples, the behavior of $\delta\lambda$ suggests a delayed saturation of grain boundaries (Fig. 5.3). This could occur either due to a lower mobility of the grain boundary fluxons or due to a lower H_{c1} of grains which allows flux penetration at a stage when the grain boundaries are not yet saturated. We feel that the first case will hold as the columnar defects may cause some steric hindrance to a free movement of vortices between the grains.

5.2.4 Quantitative analysis using the JRAT model

For a quantitative discussion on rf field penetration in Bi-2223 tapes, we apply the JRAT model in its ordered limit in view of the known brickwall type microstructure of Bi-2223 platelets [37,38]. The model defines two types of fluxon ; i) those pinned by pinning centers within the grains (h_p) and, ii) the fluxons that are confined to the grain boundaries (h_l). The grains and the grain boundaries have different flux density gradients and consequent different local critical states (Fig. 5.6e-f). But due to macroscopic granularity, the maximum grain boundary flux density $h_{f,max}$ is assumed to be constant in the intergrain region. Further, the field retracing field minima H_{mr} , $h_{f,max}$ and the Bean field H_g^* for full penetration of grains, are related for three limits of flux penetration as;

$$H_{mr} = s_p h_{f,max}^2 / 4H_g^*, \text{ for } h_{f,max} < H_g^* \quad (5.1),$$

$$H_{mr} = s_p (H_g^* / 2 - ((h_{f,max} - 2H_g^*)^2 / 4 H_g^*)), \text{ for } H_g^* \leq h_{f,max} < 2 H_g^* \quad (5.2),$$

$$H_{mr} = s_p H_g^* / 2, \quad \text{for } h_{f,max} \geq 2H_g^* \quad (5.3)$$

where s_p is the ratio between the cross-sectional area of the grain and area inclusive of weak boundary regions. For Bi-2223 platelets, the area fraction is estimated to be 0.9 [25]. The field H_g^* is equal to $\mu_0 J_{cg} d/2$ where d is the lateral dimension of the platelet and J_{cg} the intragranular critical current density. A further analysis of JRAT shows that H_{mr} increases with the maximum value of the applied field H_{max} if $h_{f,max}$ is smaller than $2H_g^*$ in the following manner,

$$H_{mr} = 2.72 \times 10^{-3} H_g^* ((1 + 40 H_{max})^{0.5} - 1)^2, \text{ for } h_{f,max} < H_g^* \quad (5.4)$$

$$H_{mr} = 0.225 (3.1 H_{max} - (H_{max}^2 / H_g^*) - 0.4 H_g^*), \text{ for } H_g^* \leq h_{f,max} < 2 H_g^* \quad (5.5)$$

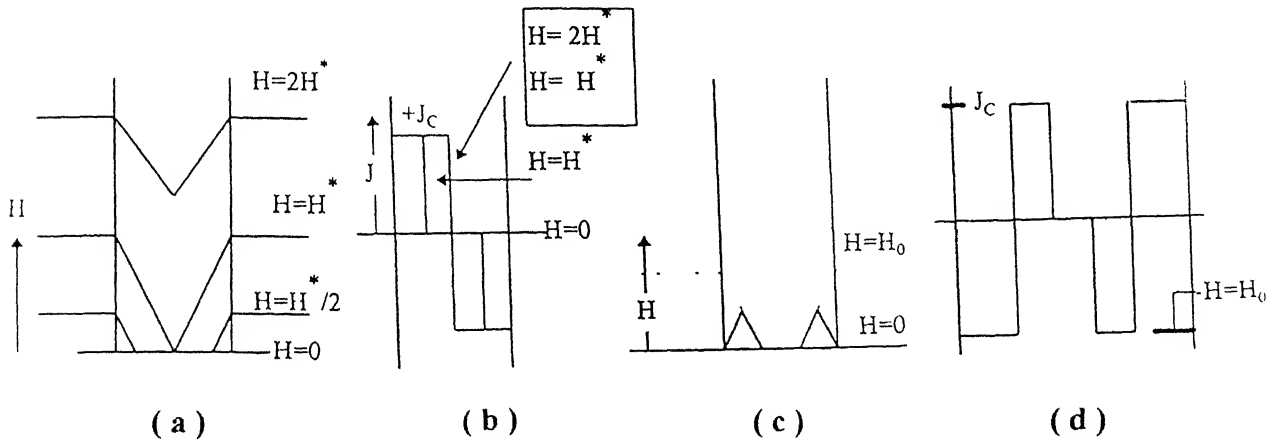


Figure 5.6 (a,b,c,d) A plot of local field current density, in Bean Critical state model for different external field values. The Bean critical field H_g^* corresponds to flux penetration into the entire width of the sample. (a) local field gradients, (b) critical current density for constant external field (c) and (d) represent the case when the external field is removed. The trapped flux gives rise to hysteresis. (From Ref. [101]).

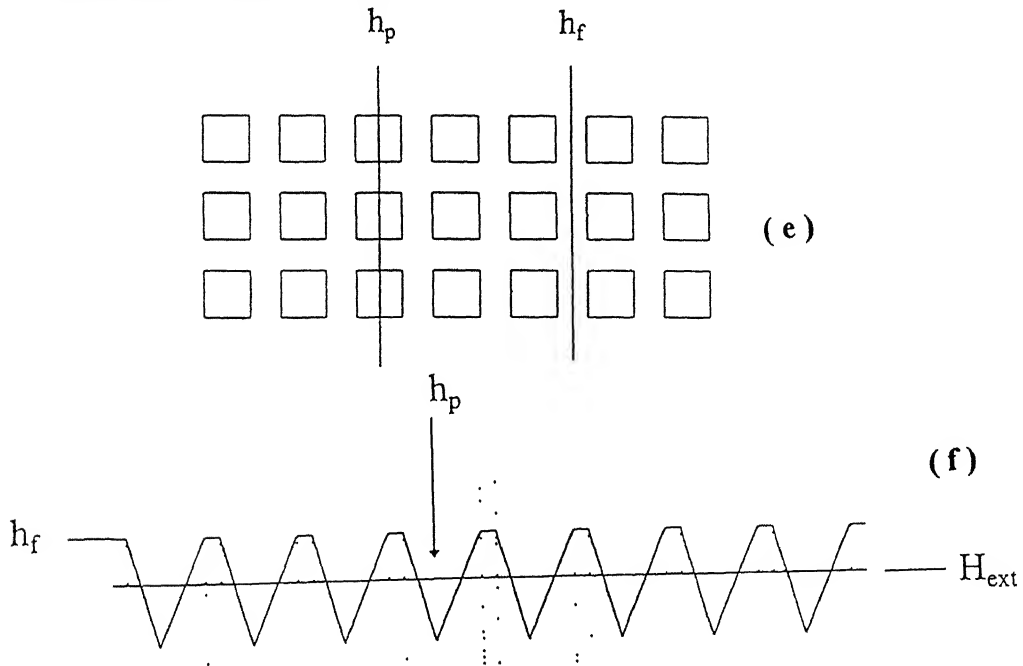


Figure 5.6 (e, f) (e) Examples of grain boundary (h_f) and grain pinned fluxon (h_p) in JRAT model in the ordered case. The cubes represent superconducting grains (f) The flux profile in the two level critical state. The dotted lines enclose the grain boundaries. (From Ref. [25]).

For $h_{f,max} > 2H_g^*$, the field at which a minimum is seen becomes independent of H_{max} (see Eq. 5.3).

We now turn to temperature and H_{max} dependence (Fig. 5.1 and Fig. 5.5) of H_{mr} in the unirradiated sample. As seen in Fig. 5.5, H_{mr} at 15 K is independent of the maximum field used in the hysteresis cycle. Using the JRAT model in the limit of $h_{f,max} > 2H_g^*$, a grain size d of 20 μm and the measured H_{mr} of 230 G, we infer an intragrain critical current density $J_{cg} \sim 4 \times 10^5$ A/cm². For temperatures above 35 K, no H_{mr} is observed because of a dramatic decrease in J_{cg} value above 35 K in the unirradiated sample which is universal in this material.

The remarkable effects of heavy ion irradiation on the behavior of hysteresis must have their origin on flux pinning at columnar defects as nothing else has changed in the experiment. For both 0.5 Tesla and 3.0 Tesla irradiated samples we have observed a minimum in $\delta\lambda$ as the external field was brought into alignment with the columnar defects (Fig. 4.4 and Fig 4.6). Having established that this cusp like manifestation of strong pinning first seen in the flux flow resistivity of heavy ion irradiated Tl-2212 films [89], is present even in these MHz frequency measurements, we discuss the shape of the hysteresis and its variation with temperature, defect density and H_{max} . First of all the saturation of $\delta\lambda$ at a given temperature shifts to higher fields on increasing the linear defect density (Fig. 5.3). This behavior is suggestive of a lower mobility of intergranular vortices due to a steric hindrance by the columnar defects. The minimum point (H_{mr}) of the hysteresis increases with H_{max} in these samples. The JRAT model predicts this type of behavior as long as the flux density in the intergranular region is lower than the critical field for full penetration H_g^* . With increasing H_{max} , the intergranular field will eventually become greater than H_g^* and H_{mr} will cease to shift. The saturation value of H_{mr} is then $s_p H_g^*/2$. The H_g^* depends on temperature through the temperature dependence of J_{cg} . The behavior of H_{mr} for the 3 T sample at 30, 45 and 55 K is shown in Fig. 5.7 along with the data for the unirradiated sample at 15 K. While the H_{mr} for 3 T irradiated remains independent of H_{max} at 55K, for measurement at $T < 45$ K the H_{mr} does not reach saturation even at the maximum field (3.2 kG).

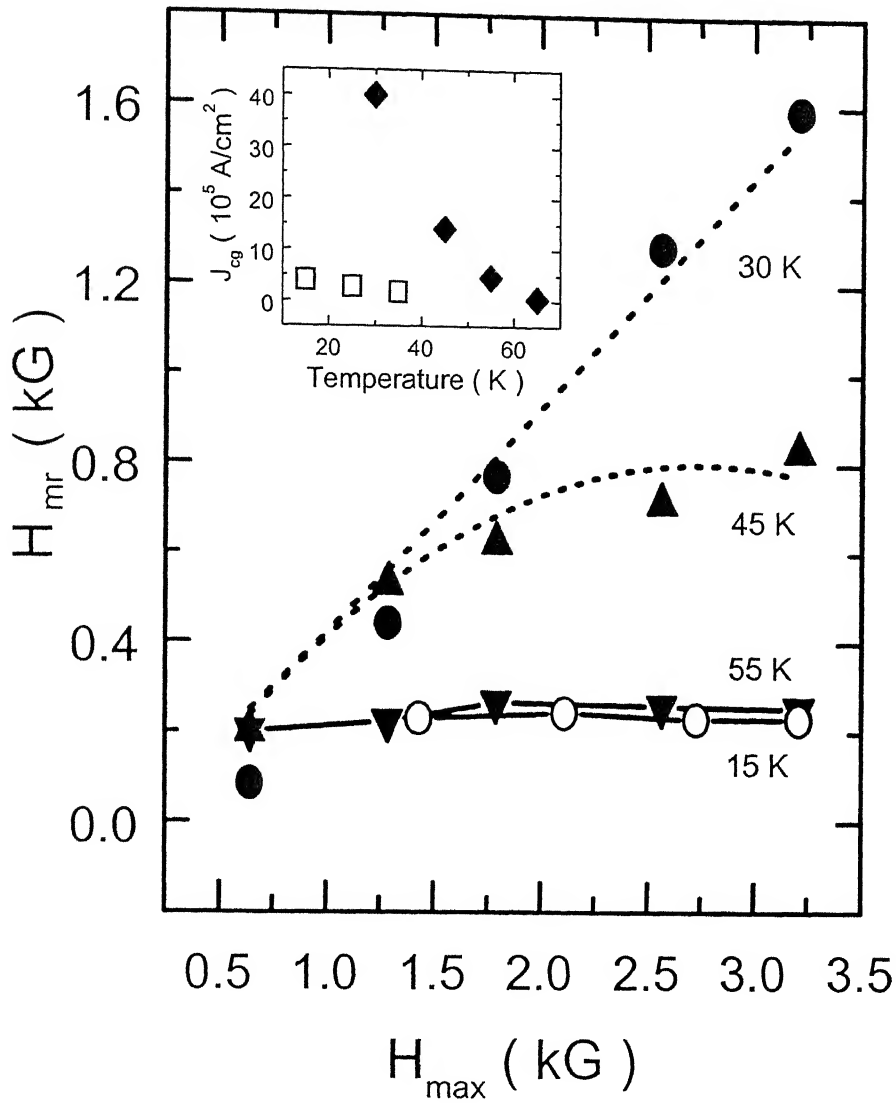


Figure 5.7 Variation of H_{mr} Vs H_{max} at different temperatures. Open symbols are for the unirradiated sample measured at 15 K, and closed symbols are for the 3 T irradiated sample. Inset shows the variation of J_{cg} with temperature for the unirradiated (\square) and 3 T irradiated sample (\blacklozenge). Dotted lines show fit of Eqs. 5.4 and 5.5 to 30 K and 45 K data respectively (see text).

This is indicative of only a partial penetration of flux into the grains due to a high value of J_{cg} at lower temperatures. We have fitted the H_{mr} Vs. H_{max} data at 30 K and 45 K to Eqs. 5.4, and 5.5 both, which correspond respectively to condition $h_{f,max} < H_g^*$ and $H_g^* \leq h_{f,max} < 2 H_g^*$. It is seen that the best fit at 30 K and 45 K are obtained with Eqs. 5.4 and 5.5 respectively. The H_g^* extracted from the fits yields the J_{cg} . The low field intragranular critical current density J_{cg} for the unirradiated and 3 T irradiated samples extracted from the fits is shown in the inset of Fig. 5.6. The large enhancement of J_{cg} after heavy ion irradiation is evident in this Figure. A point of further interest is the behavior of H_{mr} in samples with a field equivalent defect density of 0.5 Tesla. Here the inverted hysteresis is seen at temperatures as high as 85 K and the saturation of H_{mr} for the H_{max} of ~ 3.2 kG is seen only above 55 K. Both these observations are indicative of a higher J_{cg} in this sample as compared to the one irradiated at 3 T. This is yet another manifestation of a well established prediction of the Nelson - Vinokur Bose glass theory [12] wherein a one-to-one mapping between columnar defects and vortices is ideal for maximum pinning. In the field regime investigated here, the mapping is better realized in 0.5 Tesla irradiated sample.

5.3 Summary

We have identified an anomaly in the behavior of the rf penetration depth of Bi-2223 platelets. The observed hysteresis is intimately related to the characteristic granularity in silver sheathed tapes of this quasi-2D superconductor. The two level critical state approach of Ji, Rzechowski, Anand and Tinkham [25] successfully explains the anomalous response and allows extraction of the intragrain critical current density. To our knowledge this is the first study of rf vortex dynamics in Bi-2223 silver sheathed tapes in strong and weak pinning regimes.

Chapter 6

Flux Transformer experiment and vortex phases in Bi-2223 tapes

6.1 Introduction

The equilibrium and non - equilibrium behavior of vortex phases in the mixed state of high temperature superconductors has been the focus of numerous recent experimental and theoretical investigations. The role of thermal fluctuations, anisotropy and disorder vis-à-vis the magnetic phase diagram of the cuprate superconductors are well established [3]. However, most of these studies have been carried out on single crystals, whereas the technological applications of these materials crucially depend upon a proper understanding of such effects in samples of composite superconductors for use in magnet and allied technologies. In addition to having the structural and electronic features which affect vortex dynamics in single crystals, composite conductors also have a characteristic granularity, understanding of which is of considerable scientific interest. In this chapter,

we present a set of flux transformer measurements on as grown and heavy ion irradiated Bi-2223 tapes. It is known that this phase of the BiSCCO family of cuprate superconductors is less anisotropic compared to the extensively studied Bi-2212 phase. For the latter case, it is well established that for fields ≤ 600 Gauss, the low temperature vortex phase is essentially a solid consisting of 2D pancake vortices [102-104]. There is sufficient evidence that this lattice undergoes a first order melting transition on increasing the temperature [103-104]. While the melting behaviour of the vortex phase formed at high fields is not understood, the formation of vortex liquid above the irreversibility field for the low as well as high field regimes is well known. The vortex liquid is essentially 2D with no velocity correlations along the direction of the field.

Compared to Bi-2212, the higher T_c of Bi-2223 implies a greater dominance of thermal fluctuations on one hand, and an increased condensate density per set of planes, leading to less crystal anisotropy on the other. A comparative study of reversible magnetization in Bi-2212 crystals and Bi-2223 platelets by Li et. al. [46] does show much less anisotropy in the latter case. The typical brickwall type [37] microstructure of Bi-2223 platelets produced through powder - in - tube method would also tend to renormalize the intrinsic anisotropy of this system. The impact of the microstructure related correlated disorder and the correlated disorder produced by heavy ion irradiation on the liquid phase properties of the vortex state in these samples has not been established.

A simple and yet powerful technique which allows understanding of the vortex dimensionality and how it is affected by intrinsic and extrinsic defects, is the transport measurements in a dc flux transformer (FT) geometry. This technique has been used extensively to study the vortex liquid phase in Bi-2212 [105-107] and YBCO [108] systems. In clean single crystals of these superconductors, the FT measurements reveal no vortex correlation along c-axis in the liquid phase. However, in the crystals having linear defects produced by heavy ion irradiation or planar defects such as twin boundaries, the vortex matter first melts to a liquid phase where the vortices maintain correlation along the direction of the defect and then goes to an uncorrelated liquid state at still higher temperatures. In a flux transformer experiment, the hallmark of this two-step transition is the fact that the top and bottom voltages in the ab -plane, V_T and V_B

respectively, appear before the onset of c-axis voltage V_C [109] while approaching T_c from below. The range of temperature over which V_T and V_B are non - zero but $V_C = 0$, has been argued to be the region of 3D disentangled vortex liquid. For YBCO, the disentangled vortex liquid stabilized by the twin boundary pinning has been shown to freeze into the Bose glass phase at low temperatures [109]. In the case of highly anisotropic Tl-2212 and Bi-2212 superconductors with columnar defects, the disentangled liquid will also go to the Bose glass phase if $B \leq B_\phi$ (where B_ϕ is the matching field) [89,110]. While for a defect free crystal of Bi-2223 we expect a first order melting and the formation of an entangled vortex liquid just as in the case of Bi-2212 and YBCO, the FT response of a composite tape of Bi-2223 will be greatly altered by the growth related defects in the sample. Transport measurements on the composite samples of Bi-2223 have shown a vortex glass behaviour at lower temperatures [52]. There are also two reports of anisotropic current flow measurements in Bi-2223. Cho et. al. [50] have seen very small anisotropy (~ 10) for current flow in the ab-plane and perpendicular to the plane of the tape. An evidence of disentangled vortex liquid and the ensuing non - local response similar to the one seen in YBCO crystals with twin boundaries, has been reported by Sun and coworkers [51]. These authors attribute their results to the growth related structural disorder in the samples.

Our studies establish a correlation between V_T and V_B of the samples in their pristine and irradiated states for the first time. Our measurements show a two step resistive transition due to the vortex correlation along the c-axis. The role of columnar defects is to strengthen this correlation which in the unirradiated state emanates from the growth related extended defects. The overall FT response is dramatically different from what is seen in Bi-2212 with and without the CDs.

6.2 Brief overview of results and discussion

6.2.1 The case of unirradiated Bi-2223 tape

In Fig. 6.1a we show the top (V_T) and bottom (V_B) voltages as a function of temperature under zero - field condition and when dc field of different magnitude is

applied perpendicular to the plane of an unirradiated tape. The inset shows the contact configuration

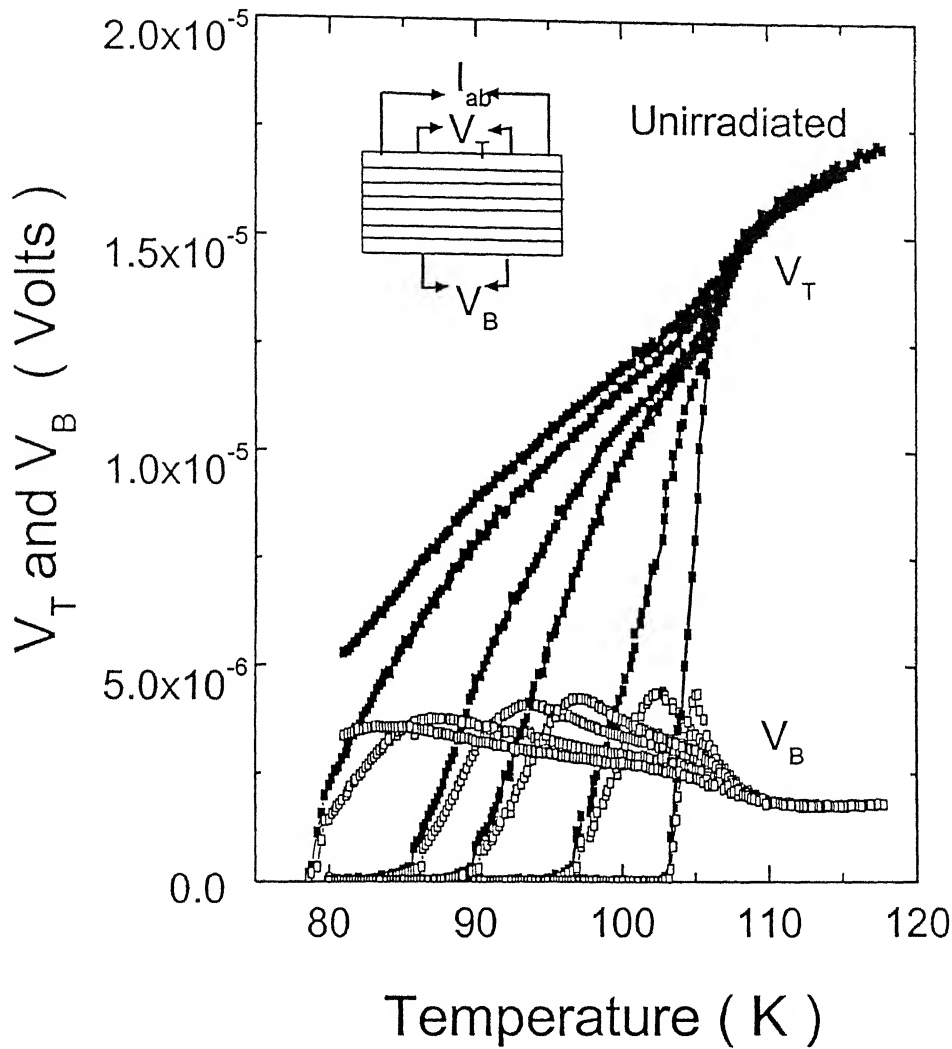


Figure 6.1a. Temperature dependence of the top and bottom voltages (V_T and V_B) as a function of external dc magnetic field for the unirradiated silver sheathed Bi-2223 tape. Solid symbols are for the top voltage and open symbols for bottom voltage. Magnetic fields from right to left are 0 , 0.2 , 1 , 2 , 5 , and 8 kG. The inset shows transformer contact configuration for in plane resistive measurements.

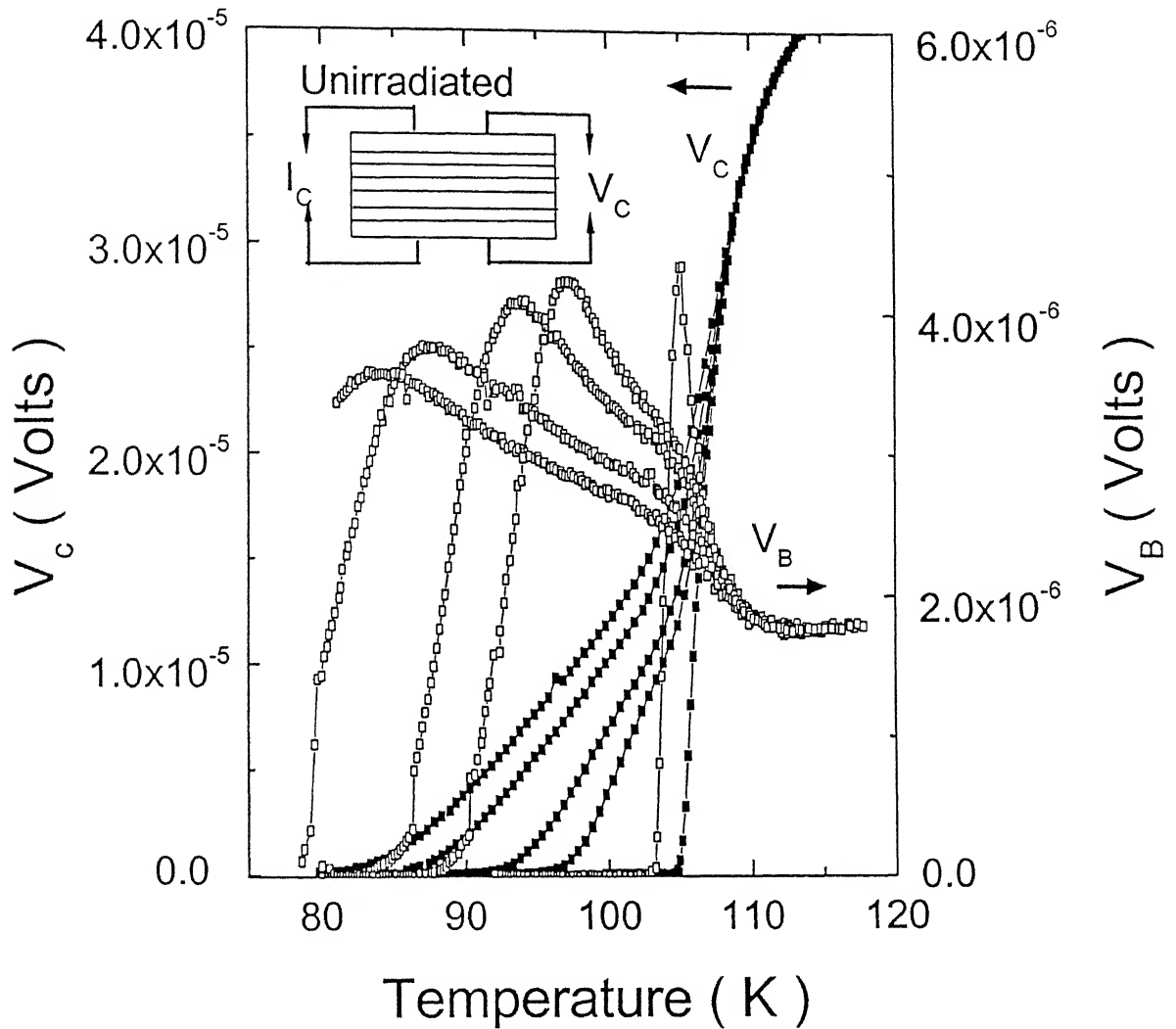


Figure 6.1b. Temperature dependence of bottom (V_B) and c-axis voltage (V_C) at external field 0, 1, 2, 5 and 8 kG (right to left). Notice the two step resistive transition and simultaneous occurrence of onset of c-axis resistivity and the decrease in bottom voltage. The inset shows contact configuration for c-axis resistive measurement.

Shown in Fig. 6.1b is the voltage V_C developed between the top and bottom electrodes (see inset of the Fig. 6.1b) when a current is made to flow along the c-axis of the platelet. In Fig. 6.1b we also show the bottom voltage V_B in order to address the issue of the onset of dissipation in two directions. The first striking feature of the data shown in Fig. 6.1 is the two-step resistive transition where the resistance along the length of the tape appears before the resistance along c-axis on warming the sample from a fully superconducting state. If we define the onset temperatures of the ab-plane and c-axis resistivities as T_c^{ab} and T_c^c respectively, the difference in these temperatures is as high as $\sim 7K$ for the measurement done at 5 kG field. The appearance of V_C at a higher temperature compared to the onset of V_B and V_T has also been seen in twinned YBCO crystals [109]. For YBCO, the range of temperature between T_c^{ab} and T_c^c corresponds to a vortex state where the pinning due to twin boundaries leads to an disentangled flux liquid with no possibility of flux cutting and hence zero V_C . At $T \geq T_c^c$ the pinning due to twin planes becomes weak and the vortex liquid goes from the disentangled to an entangled phase where flux cutting is dominant. Like the case of YBCO, here also the voltages V_T and V_B appear at the same temperature. But unlike twinned YBCO where V_B and V_T overlap over a range of 0 to $\sim 10\%$ of the normal state resistivity, here the value of V_B is always smaller than V_T . On increasing the temperature further, V_B shows a peak behaviour and then decrease gradually on increasing the temperature further. The peak in V_B occurs at the same temperature at which V_C becomes detectable. A careful examination of the data shown in Fig. 6.1b reveals a close correspondence between V_B and V_C . The range of temperature over which V_B drops gradually also corresponds to the range over which V_C rises slowly. At still higher temperatures, V_B shows a rapid drop before reaching a nearly constant value in the normal state. Correspondingly, there is a rapid increase in V_C . This is the regime where the vortices essentially behave as decoupled pancakes due to increased thermal wandering. It is interesting to note that the peak in the bottom voltage is seen even in the zero - field data and the application of a magnetic field makes it broader and also reduces its height. While a similar behaviour of V_T and V_B has been reported by Sun et. al. [51] for silver sheathed Bi-2223 tapes, they did not correlate it with the behaviour of V_C . Further, in their data V_T and V_B are equal uptill the peak in V_B . This suggest a strong renormalization of ρ_{ab} and ρ_c by grain

boundaries and other extended defects in their samples just as in the case of twinned YBCO crystals.

A simple interpretation for the origin of the peak in Fig. 6.1 can be given on the basis of zero c-axis resistivity at low temperature which would allow a uniform flow of current across the thickness of the sample. As ρ_{ab} becomes non - zero due to vortex motion in the plane, correspondingly the bottom voltage would also pick up. A further increase in temperature leads to flux entanglement and cutting, and ensuing non - zero ρ_c . The compound effect of a loss of vortex correlation along c-axis and the inability of current to reach the bottom layers due to non - zero ρ_c is the observed drop in V_B . It is important to print out that this type of peak effect in V_B has also been seen by some groups in Bi-2212 crystals [106,111,112]. However, the observation is not universal [107] suggesting an extrinsic origin, perhaps related to some type of extended defects in the crystals. Fig. 6.1c shows the top, bottom and c-axis voltage as a function of temperature with a dc field of 2 kG applied perpendicular to the ab plane of the unirradiated sample. The general features discussed above are seen more prominently. The plot convincingly establishes the one to one relationship between decrease in bottom voltage V_B and onset of resistive transition along c-axis.

6.2.2 Modifications in the strong pinning regime

To compare the effects of heavy ion irradiation on c-axis correlation, in Fig. 6.2 we show the behaviour of V_T , V_B and V_C in a sample which was irradiated at a field equivalent fluence of 3 Tesla. A comparison of these data with Fig. 6.1 shows a remarkable shift of the onset of c-axis and ab-plane resistivities to higher temperatures in the sample with columnar defects. The effects of strong flux pinning at columnar defects is evident in these data. A closer look at the behaviour of V_T and V_B for a given field (Fig. 6.2a) shows that they appear at the same temperature. The bottom voltage V_B attains a peak value just as in the case of the unirradiated sample and then decreases monotonically till the normal state is reached. The onset temperature (T_c^c) of the c-axis voltage V_C is

higher than T_c^{ab} in the irradiated sample as well. There are three important differences in the behaviour of the unirradiated sample and the sample with CDs.

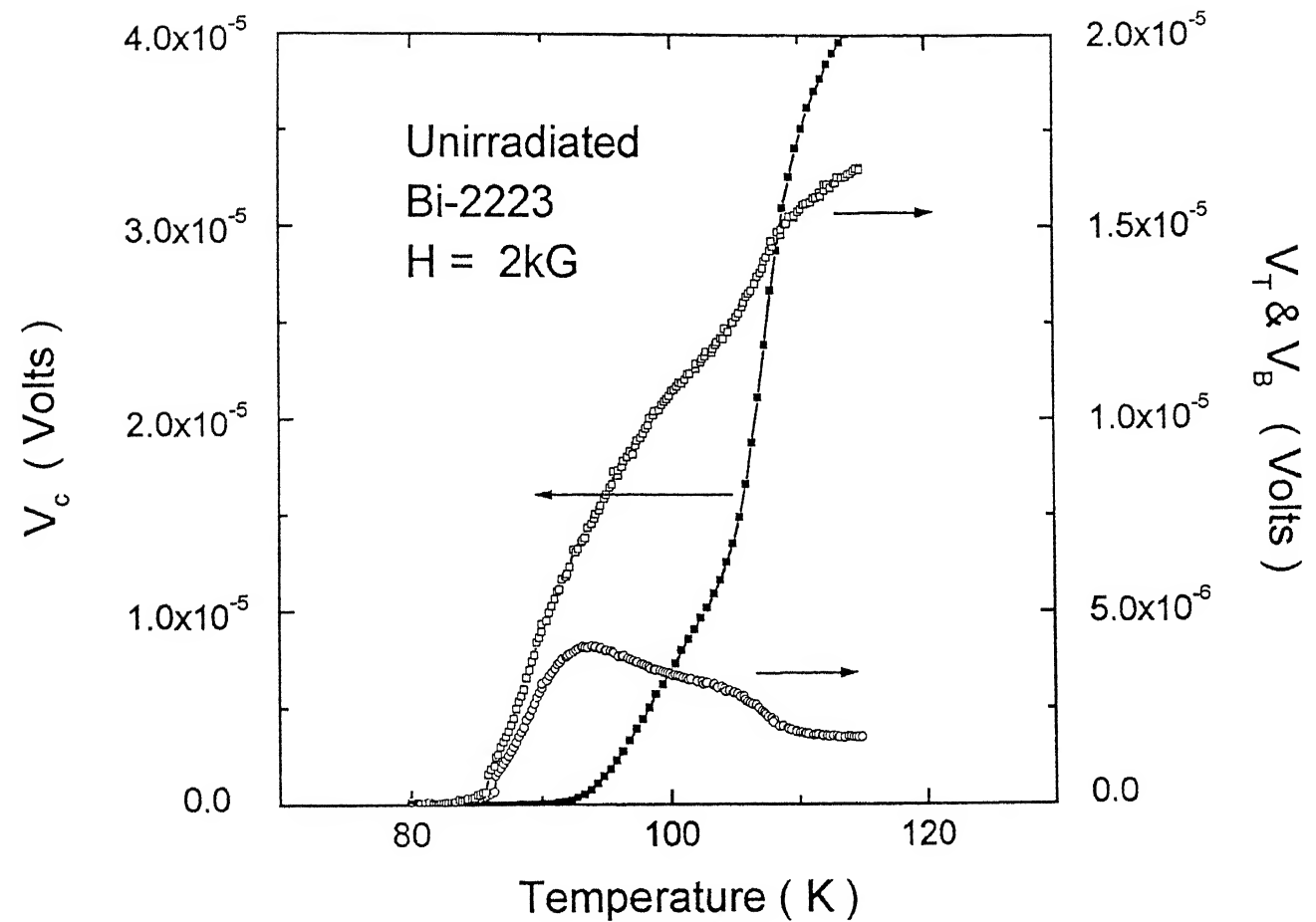


Figure 6.1c Temperature scan of top, bottom and c-axis voltage at 2 kG field applied parallel to C-axis. Onset of c-axis resistivity marks the decrease in bottom voltage. At high temperature the c-axis coupling is further weakened leading to a transition from line liquid to 2D liquid.

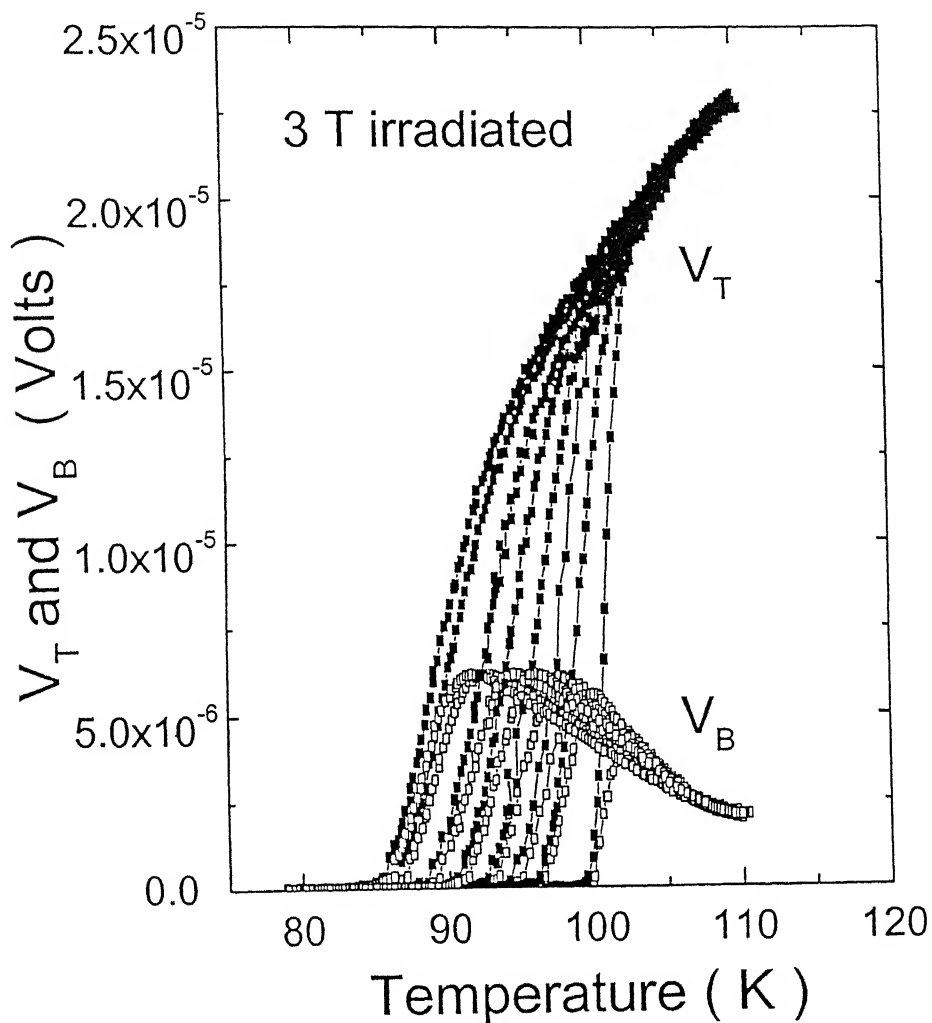


Figure 6.2a In-field temperature scans for the irradiated sample with $B_\phi = 3$ T. The magnetic fields from right to left are 0, 0.075, 0.2, 0.5, 1, 2, 5, and 8 kG.

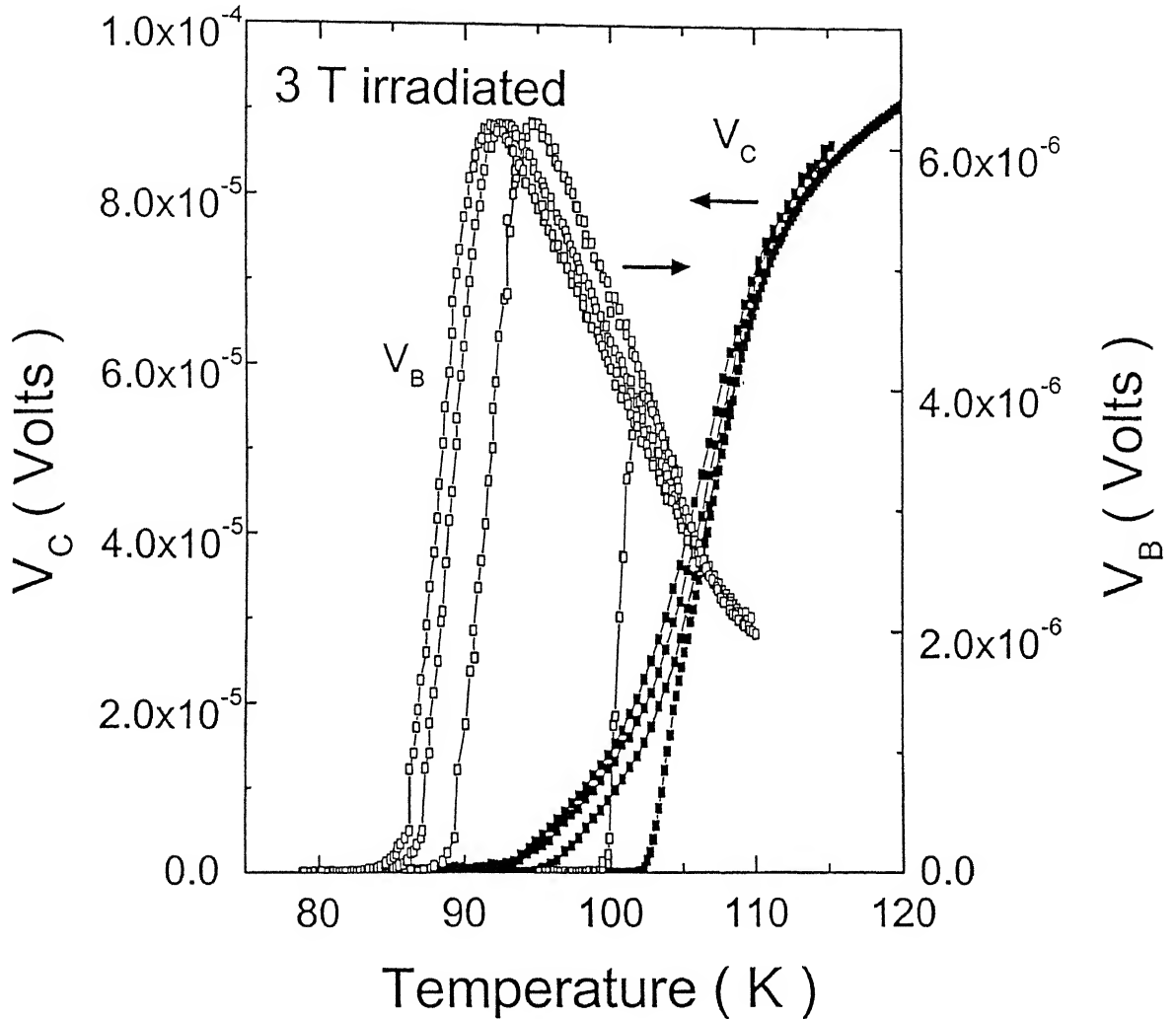


Figure 6.2b. The bottom (V_B) and c-axis (V_C) voltages for the irradiated sample. The shoulder at higher temperature with weaker c-axis correlation is not seen in this case. Also notice that unlike the unirradiated case, the peak of V_B initially increases with field and then attains a saturation value. The external magnetic field values are 0, 2, 5 and 8 kG from right to left.

They are, (i) at temperatures below the peak in V_B , the top and bottom voltages track each other more closely, (ii) the shoulder seen at higher temperatures (close to T_c) in the V_B of unirradiated sample is not seen in this case and, (iii) the peak in V_B first becomes stronger with the increasing field and then attains a saturation value.

Before we discuss these results any further, it remains to be shown that the main features of the data in Fig. 6.1 and Fig. 6.2 indeed reflect the transport in Bi-2223 tape, and are not an artifact of the top and bottom silver layers which share some of the current. In Fig. 6.3 we plot the sample resistance R_s calculated from the measured resistance R_m and the resistance of the silver sheath R_{Ag} assuming a parallel combination of R_s and R_{Ag} . Since the main features of the data after correction remain unchanged, it is reasonable to argue that Fig. 6.1 and Fig. 6.2 reflect the true response of vortices in these samples. From Fig. 6.3 we also obtain the inplane resistivity of the sample in the normal state ($T \sim 115$ K). The ratio of inplane resistivity between the top and bottom contacts obtained from Fig. 6.3 allows us to calculate the resistivity anisotropy in the normal state of the unirradiated and irradiated samples [106]. The calculated value of the anisotropy is only ~ 15 . While in single crystals of Bi-2212 this number is \sim three orders of magnitude higher. The anisotropy of the tapes is in fact comparable to the anisotropy in YBCO [108]. Another interesting outcome of this analysis is fact that ρ_c / ρ_{ab} is smaller in the irradiated sample. This shows that the structural disorder created by ion irradiation renormalizes the anisotropy.

6.2.3 Comparison between irradiated and unirradiated case

From the results shown in Fig. 6.1 and Fig. 6.2 it is apparent that the unirradiated platelets of Bi-2223 behave quite differently from the highly anisotropic Bi-2212 crystals where generally, no evidence of a c-axis correlation between the pancakes is seen in the flux - transformer data [105-107]. The Bi-2223 platelets in fact behave more like twinned YBCO. Just as in the case of YBCO, a close correspondence between V_T and V_B in the tape sample must be related to certain types of defects. The extended defects in the direction of the field are the grain boundaries connecting two platelets on the plane of the tape. Such grain boundaries, if sufficiently clean, can give rise to correlated pinning.

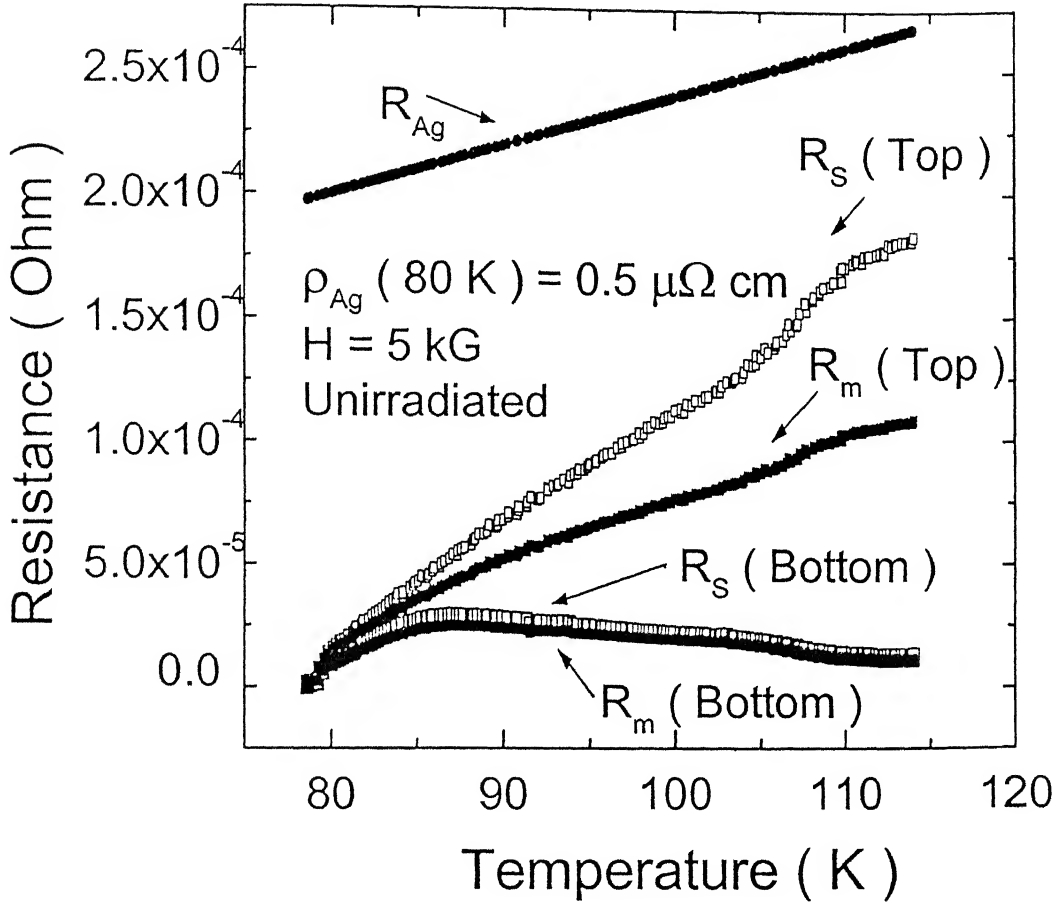


Figure 6.3 The measured (R_m), silver (R_{Ag}), and superconducting core (R_s) resistances as a function of temperature at 5 kG for the unirradiated sample. R_s is calculated assuming the measured resistance to be due to a parallel combination of 25 μm thick silver sheath and superconducting core of thickness 80 μm .

It appears that as against the hypothesis of the brickwall model, some current does flow through the ab-plane boundaries and the motion of grain boundary pinned vortices leads to a close correspondence between V_T and V_B . However, this behaviour is not as striking as in YBCO where V_T and V_B overlap. This is perhaps because the ab-plane grain boundaries are not continuous across the thickness of the sample unlike the twin boundaries in YBCO. By analogy with YBCO, we attribute the temperature regime between T_c^{ab} and T_c^c to a disentangled vortex liquid formed as a result of flux pinning at ab-plane grain boundaries. Above T_c^c and below T_c^s (temperature corresponding to the shoulder in V_B) the vortex liquid retains some correlation along the c-axis and behaves as an entangled liquid as flux cutting does take place to give a non - zero V_C . Finally, above T_c^s we have a fully decoupled vortex liquid.

The heavy ion irradiation leads to the formation of columnar defects along the normal of the tape sample. These predominantly c-axis oriented rectilinear defects act as a backbone to support the stack of pancake vortices. The stack then behaves as a line vortex with a non - zero line tension. In Bi-2212 crystals with CDs , Doyle et al. [107] have reported a novel reentrant behaviour in V_B . They conclude that the columnar defects lead to the formation of a disentangled vortex liquid in the temperature range T_c^{ab} and T_c^P , where T_c^P is the temperature at which V_B attains a peak value. While some of the features of the data on Bi-2223 shown in Fig. 6.2 are similar to the report on Bi-2212 with CDs, in our case the bottom voltage remains non - zero between T_c^P and the normal state where as in Bi-2212 it goes to zero and then reappears. The role of columnar defects in Bi-2223 is only to provide additional correlated pinning which strengthens the entangled liquid state of the unirradiated material in the entire temperature range between T_c^P and the normal state. This is perhaps the reason why we do not see the shoulder in V_B which we had attributed to the onset of decoupled state in the unirradiated sample.

6.2.4 Arrhenius plots and the activation energy

The existence of a substantial difference in current transport in the vortex state of Bi-2212 and Bi-2223 is also seen in the behaviour of the activation energy U_o for ρ_{ab} . We have calculated U_o from the Arrhenius plots of V_T and V_B .

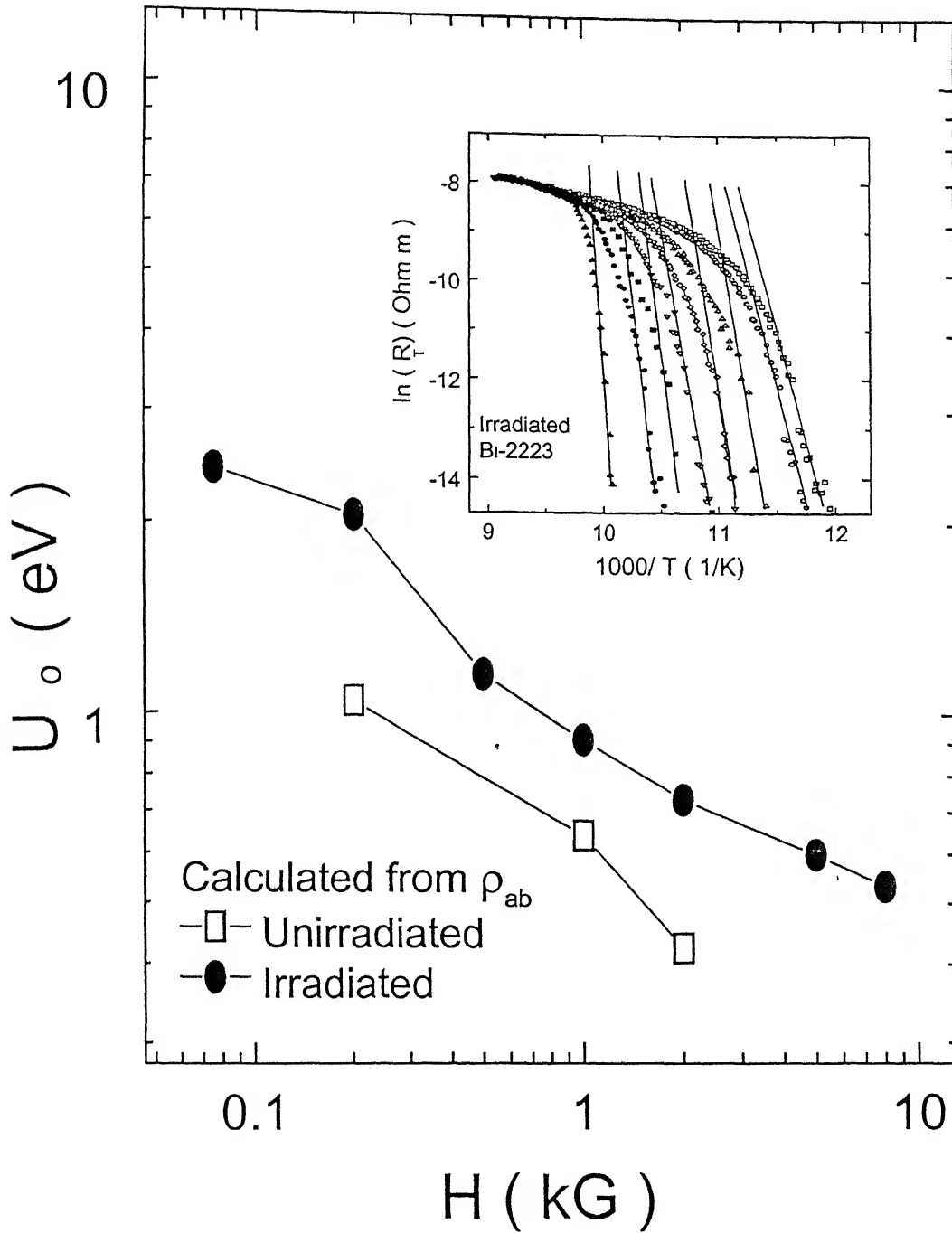


Figure 6.4 The activation energy calculated from the slopes of Arrhenius plots for the unirradiated and 3 T irradiated samples. Inset shows linear fits in the high temperature regime for the irradiated sample. The slopes are calculated from top surface resistance R_T ($= V_T / I$). Similar plots for V_C did not yield straight lines indicating to the fact that the loss mechanism is not thermally activated along c-axis.

Such plots for the irradiated sample after correction for silver are shown in the inset of Fig. 6.4. A distinctly activated behaviour over a range of temperature is clearly seen in the data. In Fig. 6.4 we plot the activation energy for the unirradiated sample and the sample with columnar defects. While the activation energy for clean Bi-2212 crystals at a field of ~ 5 kG is ~ 60 meV [106,113], for the Bi-2223 tapes we get ~ 0.8 eV, a number which is comparable to the reported value by Sun et al. for similar samples [51]. The U_0 after introduction of columnar defects increases by a factor of ~ 2 . It is instructive to compare it with the U_0 of Bi-2212 crystals with CDs where at 5 kG field ($B_\phi = 10$ kG) it is higher by a factor of ~ 4 compared to the unirradiated state [114]. From these observations it is further evident that a distinctly different crystallographic structures of Bi-2223 and the growth related defects and misorientation in silver sheathed tapes of this compound have the compound effect of making it much less anisotropic compared to the Bi-2212 phase.

6.3 Summary

In summary, our measurements of vortex dynamics in silver sheathed platelets of $(\text{Bi-Pb})_2\text{Sr}_2\text{Ca}_2\text{Cu}_3\text{O}_{10}$ in the flux transformer geometry show a behaviour similar to that of twinned $\text{YBa}_2\text{Cu}_3\text{O}_7$ crystals and dramatically different from the response of $\text{Bi}_2\text{Sr}_2\text{CaCu}_2\text{O}_8$. We attribute it to a stronger coupling between Cu-O superconducting planes and the reduction of anisotropy by growth related defects and misorientations. The presence of columnar defects renormalizes this anisotropy further and a distinctly c-axis correlated vortex liquid state is seen in these FT measurements.

Chapter 7

Anisotropy dominated rf vortex dynamics in Bi-2212 tapes

7.1 Introduction

Flexible tape samples of $\text{Bi}_2\text{Sr}_2\text{CaCu}_2\text{O}_8$ superconductor can be made in large quantities using simple and economical techniques such as Doctor blade and dip coating which have not been very successful in the case of Bi-2223 material. Such tapes are promising for high field applications at low temperature (~ 4.2 K) where their properties are not different from those of Bi-2223. The Bi-2212 phase is also interesting from the fundamental view point because it is one of the most anisotropic superconductor. A large part of the vortex phase diagram in this case is occupied by the liquid state and the dominance of thermal fluctuations gives rise to many novel phase transitions. The theory of statics and dynamics of vortices in Bi-2212 has been studied by many workers [3,32,33,115,116]. Since it is fairly easy to grow large single crystals of this compound, experimentally also it is an extensively studied high T_c cuprate [3]. The mixed state of Bi-2212 consists mostly of two - dimensional vortices except at very low fields

(~ 60 mT). The in-plane and out of plane interactions between these vortices in the presence of thermal fluctuations and static disorder lead to many novel phenomena. With this background information on the clean system, the purpose of this study is to look into the fundamental and applied aspects of vortex dynamics and dissipation in Bi-2212 tapes. Like all real samples of technological importance, the silver clad Bi-2212 composite conductors also have defects in the form of grain boundaries, dislocation loops, second phase impurities and misorientation between the grains. In the presence of granularity, it becomes relevant to ask whether the 2D theories of vortex dynamics applied to single crystals would hold for this granular system as well.

In this chapter we report on the granularity and two dimensional aspects of vortex dynamics in Bi-2212 tape samples probed with the rf technique. The rf response in the geometry when the dc field is perpendicular to the tape suggests two distinct regimes of vortex dynamics, one corresponding to a moderately pinned three-dimensional vortex solid and the other a liquid of two- dimensional vortices. This change in dynamics is consistent with published measurements on single crystal samples of Bi-2212. The rf penetration depth in the 3D pinned phase is analyzed in the framework of the theories of single vortex pinning and the behaviour of pinning force constant k_p is discussed. In the pinned phase we see evidence of flux lock-in effect between the Cu-O planes. The angle dependent response in the liquid state scales with the component of dc field parallel to c-axis. The scaling analysis shows some renormalization of the anisotropy due to none-zero deviations from perfect alignment of the grains parallel to the plane of the tape.

7.2 Results and discussion

7.2.1 Temperature dependence of rf penetration depth

As mentioned in Chapter 2, the samples were made by a dip coating technique. Samples for rf penetration depth measurements were prepared by scrapping off the Bi-2212 coating from one side of the tape and then dissolving the silver in H_2O_2 and ammonia solution. Since this etchant does not react with Bi-2212, the other side of the coating is left intact in the form of thin platelets. Six platelets of Bi-2212 material are cut into the size of $\sim 1.8 \times 1.8 \text{ mm}^2$ and stacked on top of each other using GE varnish onto a sapphire

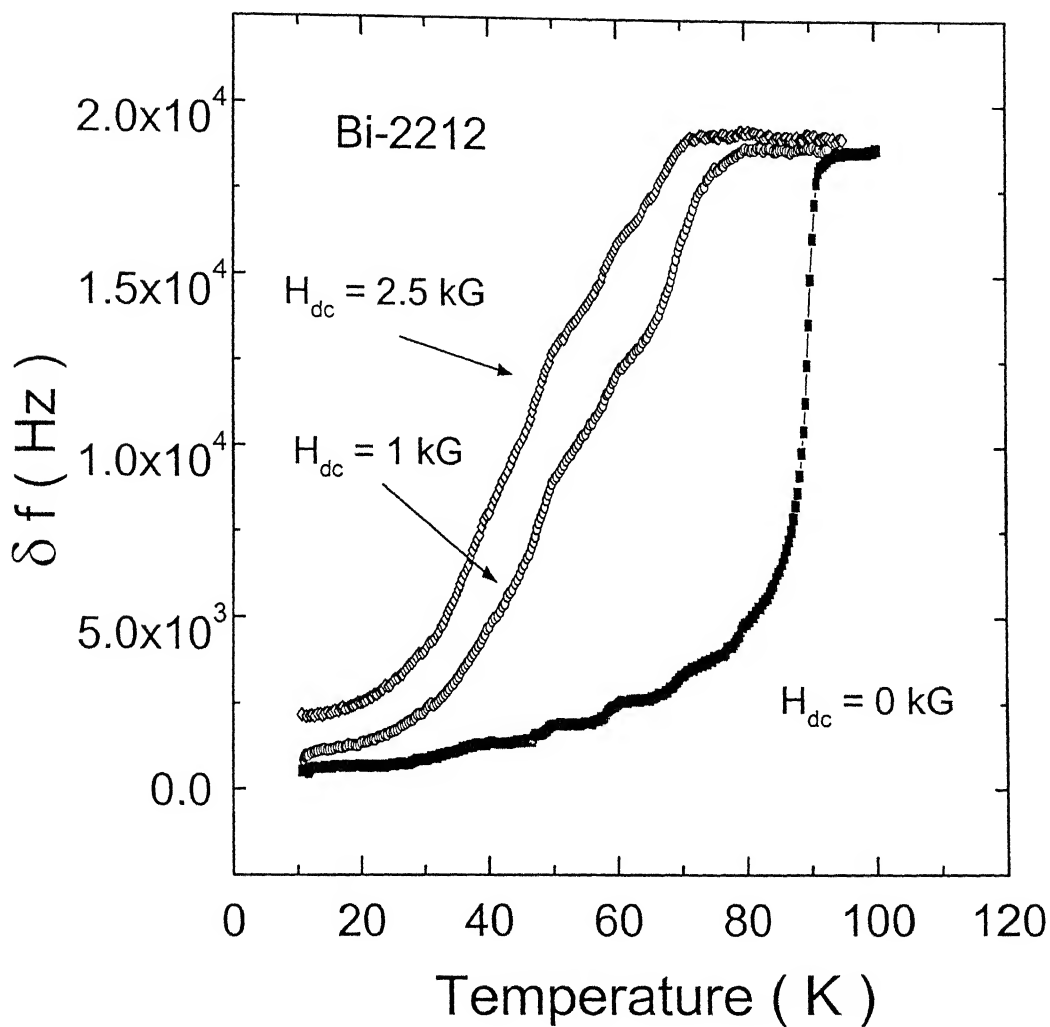


Figure 7.1 Frequency shift δf is plotted as a function of temperature at 0, 1 and 2.5 kG field applied perpendicular to the plane of the tape. Notice the large in-field broadening of inductive transition.

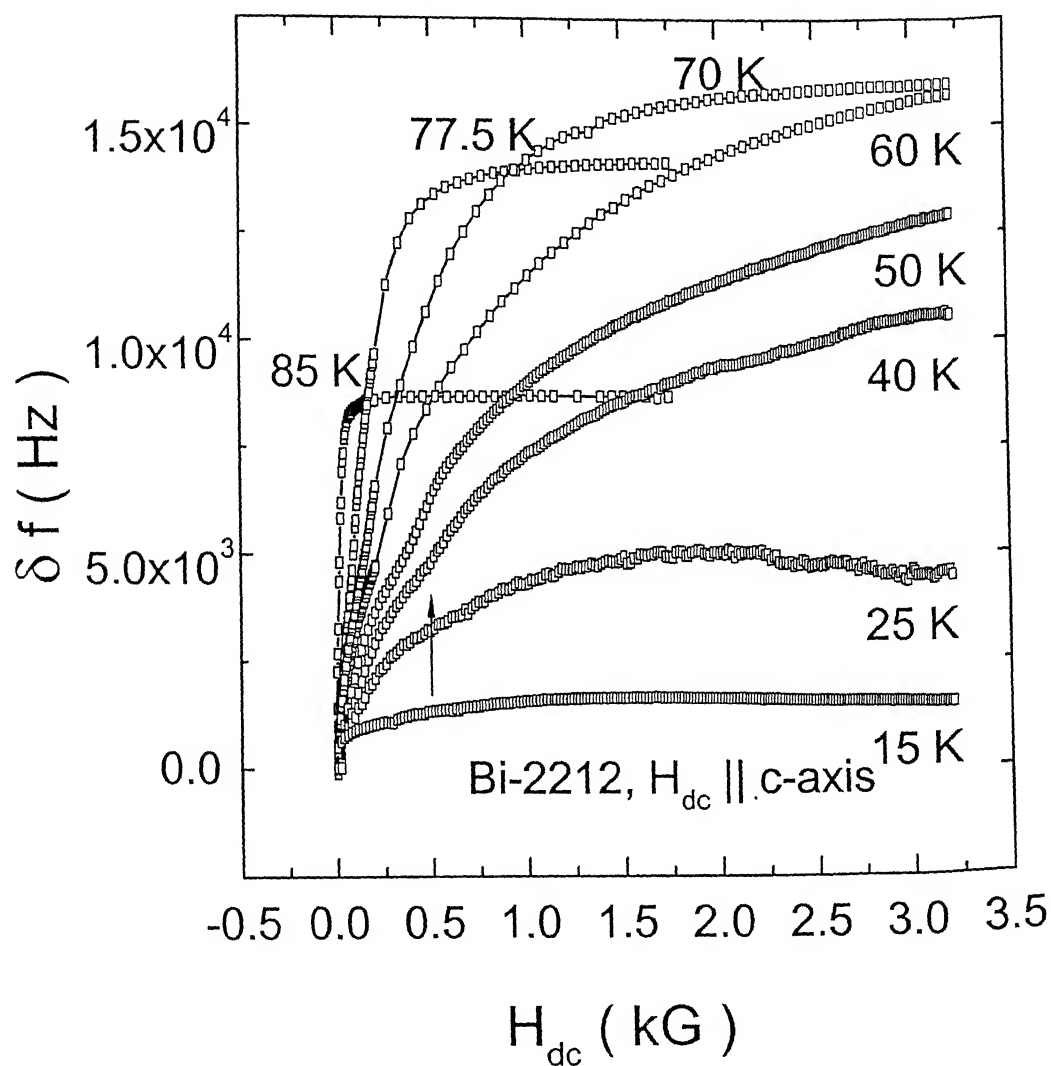


Figure 7.2 The frequency shift δf as the external dc magnetic field which is oriented perpendicular to the tape plane is scanned upto a maximum field of 3.2 kG at various temperatures. The arrow marks the appearance of a shoulder in ac field penetration response in a particular field and temperature regime.

In Fig. 7.2 we also notice that the rapid rise of δf in the field range of 0 to 0.5 kG is truncated by a small but distinct plateau. This feature is clearly visible in the data taken between 70 K and 40 K.

The position of the plateau shifts to higher field on decreasing the temperature. This dampening effect on rf field penetration suggests a change in dynamics of vortex motion which becomes operational in this range of temperature and field. In Fig. 7.3 we show the measurements of frequency shift $\delta f (H, T)$ at several temperatures for the dc field oriented parallel to the plane of the tape. This $H \parallel$ ab-plane configuration does not show the plateau. Infact, our measurements of δf Vs. field at several values of the angle θ reveal that this feature is seen only when the orientation of the dc field is closer to the normal to the tape plane (i.e. parallel to c-axis, $\theta = 90^\circ$). The maximum field upto which the plateau is seen is well within the range where Bi-2212 system is known to form 3D like vortices. This line like nature of vortices in Bi-2212 crystals is well established through neutron diffraction and muon spin rotation experiments [102,103] .

Fig. 7.4 plots the change in oscillator frequency δf as a function of \sqrt{H} . The plot clearly show a square root dependence on the applied magnetic field till the field upto which a plateau is seen in Fig. 7.2. The field at which δf deviates from the \sqrt{H} dependence has been marked by arrows in Fig. 7.4. In Fig. 7.5 we plot these fields as a function of temperature. In the same inset we also plot the 3D vortex melting data of Zeldov et al. [104] and the irreversibility temperature reported by van der Beek and co-workers [117]. The theoretical 3D to 2D vortex lattice melting line is determined by the Lindemann criterion and the transition line is given by a power law [104] , $B_m (T) = B_0 (1 - T/T_c)^\alpha$, where $\alpha \leq 2$ and $B_0 (= 5.6 c_L^4 H_{c2}(0) / Gi)$ is a constant related to Lindermann constant c_L ($\sim 0.1 - 0.4$) and Ginzburg number Gi . The solid line in Fig. 7.5 is a best fit to the experimental data and yields $B_0 = 1086$ G and $\alpha = 1.24$. Assuming $H_{c2}(0) \sim 150$ T and $c_L = 0.1$, we get $Gi = 0.77$. The high value of Ginzburg number, (for comparison in YBCO, $Gi \sim 10^{-2}$) confirms the dominance of thermal fluctuations even in granular tape samples of Bi-2212.

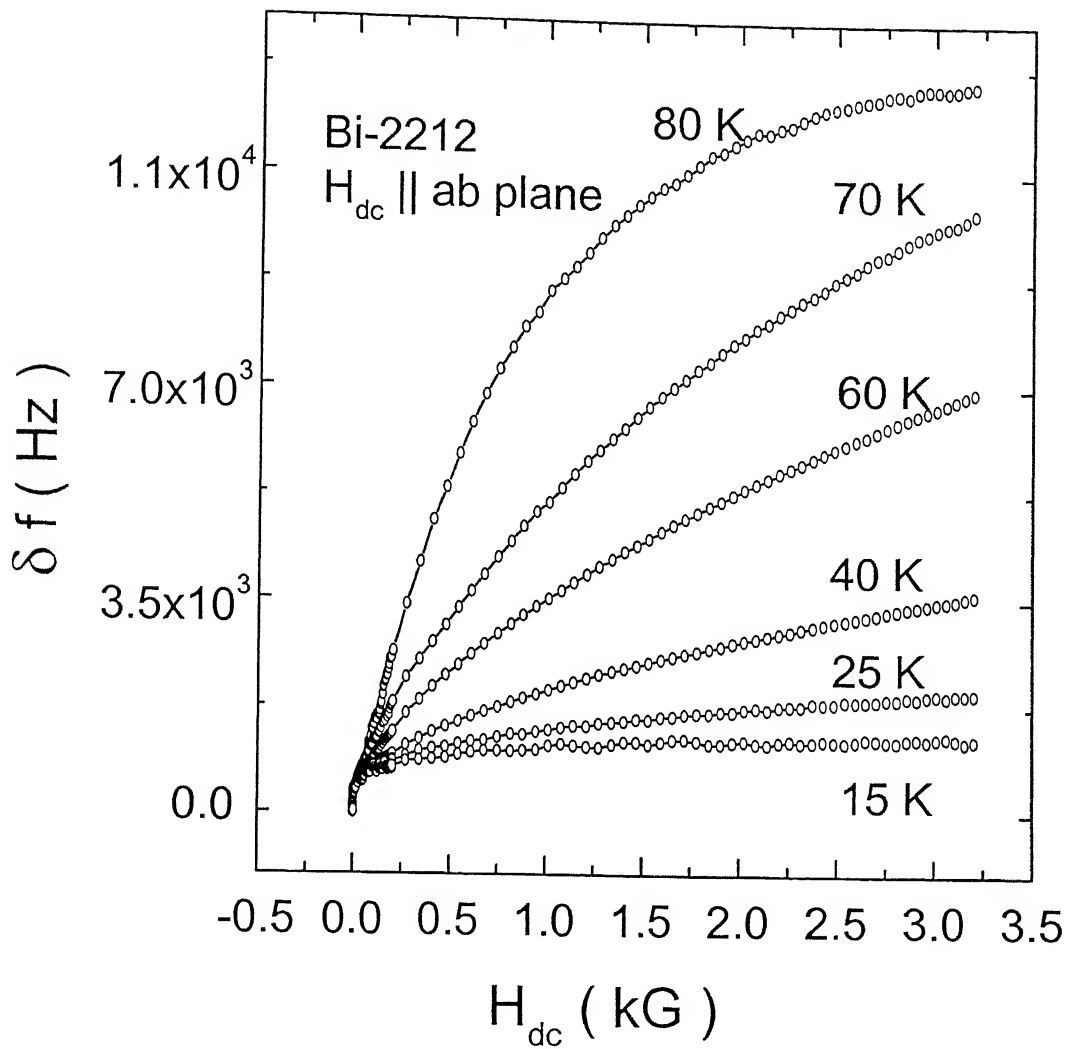


Figure 7.3 The frequency shift δf Vs. H_{dc} when the field is applied parallel to the planes. The shoulder seen in perpendicular orientation is not seen here. Notice also the delayed saturation of ac field penetration as compared to the perpendicular configuration.

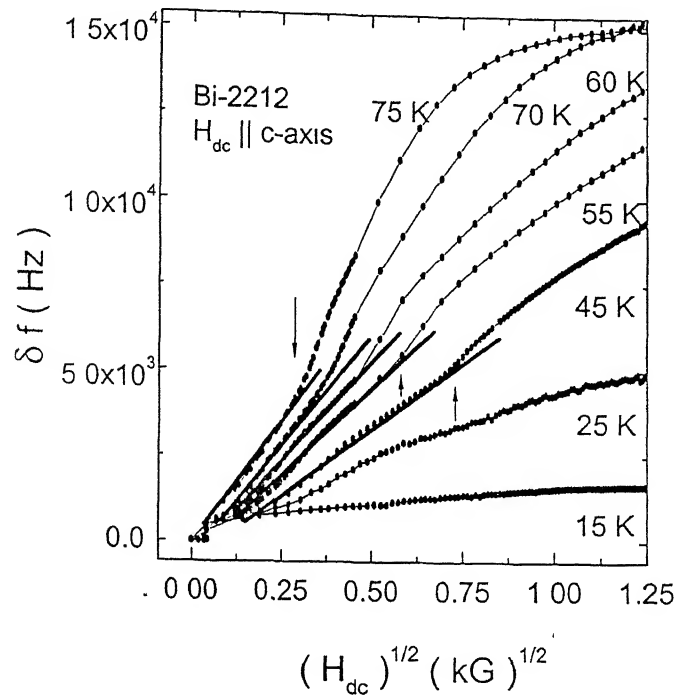


Figure 7.4 δf Vs. $\sqrt{H_{dc}}$ at several temperatures for the field applied perpendicular to the tape plane. At field values less than the point where the shoulder appears, straight lines can be fitted to the data.

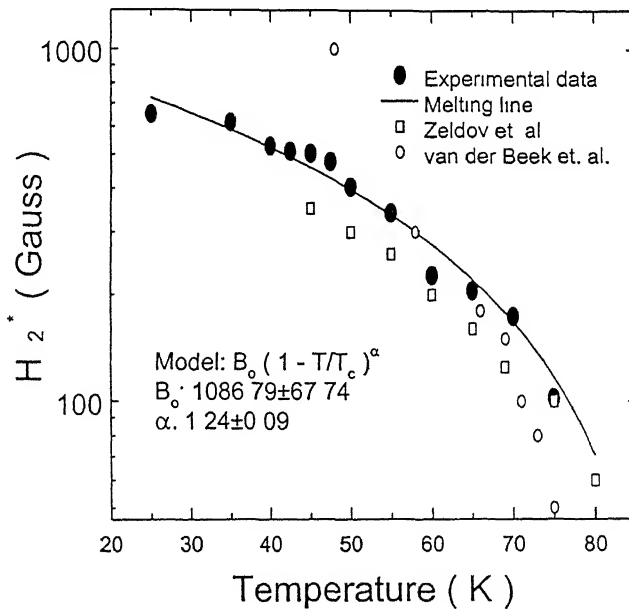


Figure 7.5 The crossover field H_2^* plotted as a function of temperature. The solid line is a best fit for the melting transition. Also shown are experimental results of Zeldov et al. and van der Beek et al. (See text).

While a Bardeen - Stephen type flux flow of 3D vortices should lead to a \sqrt{H} dependence of $\delta\lambda$ albeit with a different slope which is related to η , the fact that we do not see such a behaviour can be attributed to the 2D nature of the flux liquid in Bi-2212 for all values of the applied field. In this regime of the vortex state, the normal fluid component may also contribute to the total change in $\delta\lambda$ and hence a deviation from \sqrt{B} dependence. The picture that emerges is as follows; In the temperature and field regime below the plateau, we have a 3D vortex solid where the crystalline order is perturbed by weak pinning. At higher fields and temperatures this solid phase transforms to a liquid of 2D pancake vortices. We will, in a subsequent discussion, show that the response of the system in this liquid state follows 2D scaling laws. It is interesting to note that similar observations in the rf (44.5 MHz) response of Bi-2212 single crystals have been made by Hanaguri et. al. [82]. A clear change over in the dynamics from pinning dominated to flux flow dominated regime is seen in other layered superconductors as well [20]. The pinning force constant in the 3D state has been inferred from the Campbell formula (Eq 3.2). In Fig. 7.6 we show the behaviour of k_p normalized with respect to k_p (35 K) as a function of temperature. This normalization is necessary to take care of the geometric factor G of the experiment which is critically linked to the shape and size of the sample. In the same Figure we also plot the pinning force constant k_p measured by Hanaguri et al. for Bi-2212 crystals and k_p for silver sheathed Bi-2223 tapes from our experiments. While k_p value for Bi-2212 tape is higher than the data for Bi-2212 single crystals, the pinning for Bi-2223 is evidently stronger .

7.2.3 Angular dependence

In Fig. 7.7 we show the frequency shift δf as a function of the angle between the ab plane and the direction of the dc field. These measurements have been done at 50 K and dc field of 0.5, 1 and 2 kG. The sharp cusp in δf at $\theta = 180^\circ$ when the dc field becomes parallel to the plane of the tape is an indication of excellent c-axis texture of the tapes. The anisotropy observed here is comparable to that seen in single crystal and epitaxial films of Bi-2212. A comparison of these data with similar measurements done on

Bi-2223 tapes (Fig. 4.2) further reveals that the anisotropy is much more pronounced in these samples.

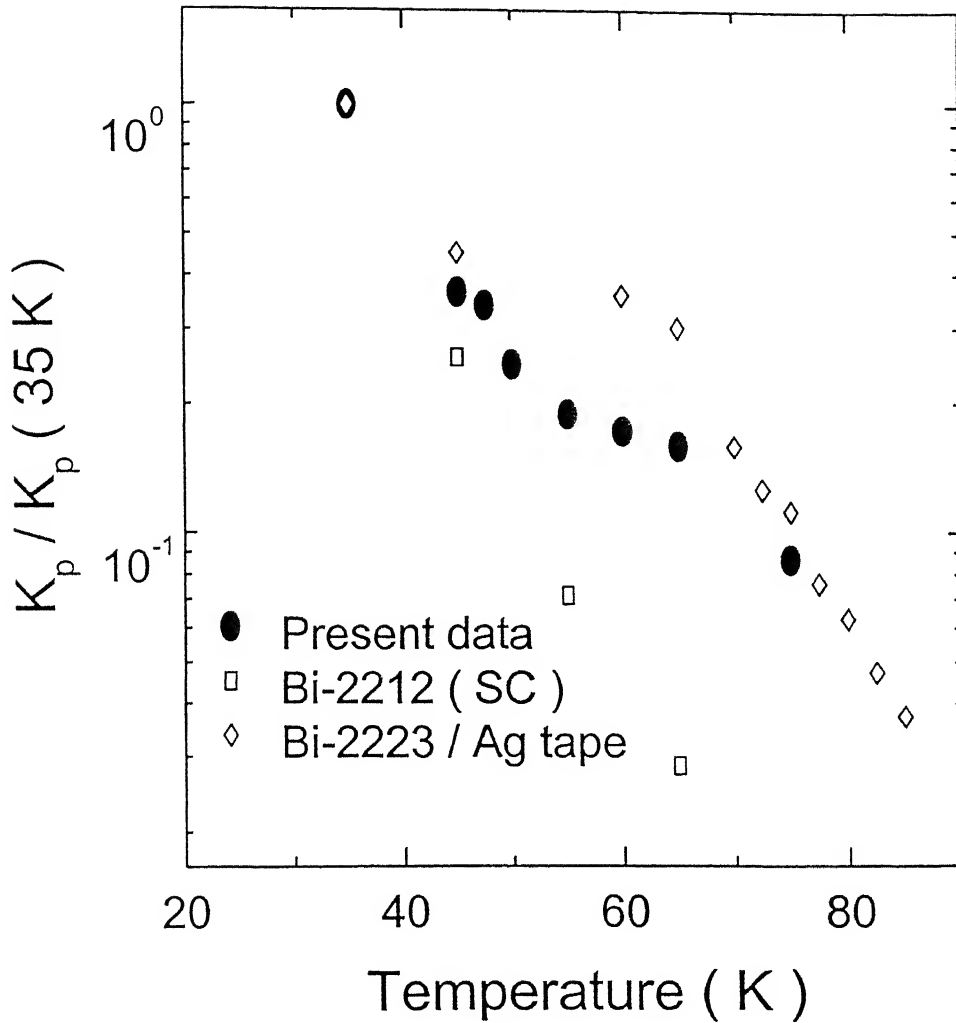


Figure 7.6 The normalized pinning force constants calculated from slopes of δf Vs. $\sqrt{H_{dc}}$ curve is plotted as a function of temperature and is compared with available Bi-2212 single crystal and Bi-2223 data.

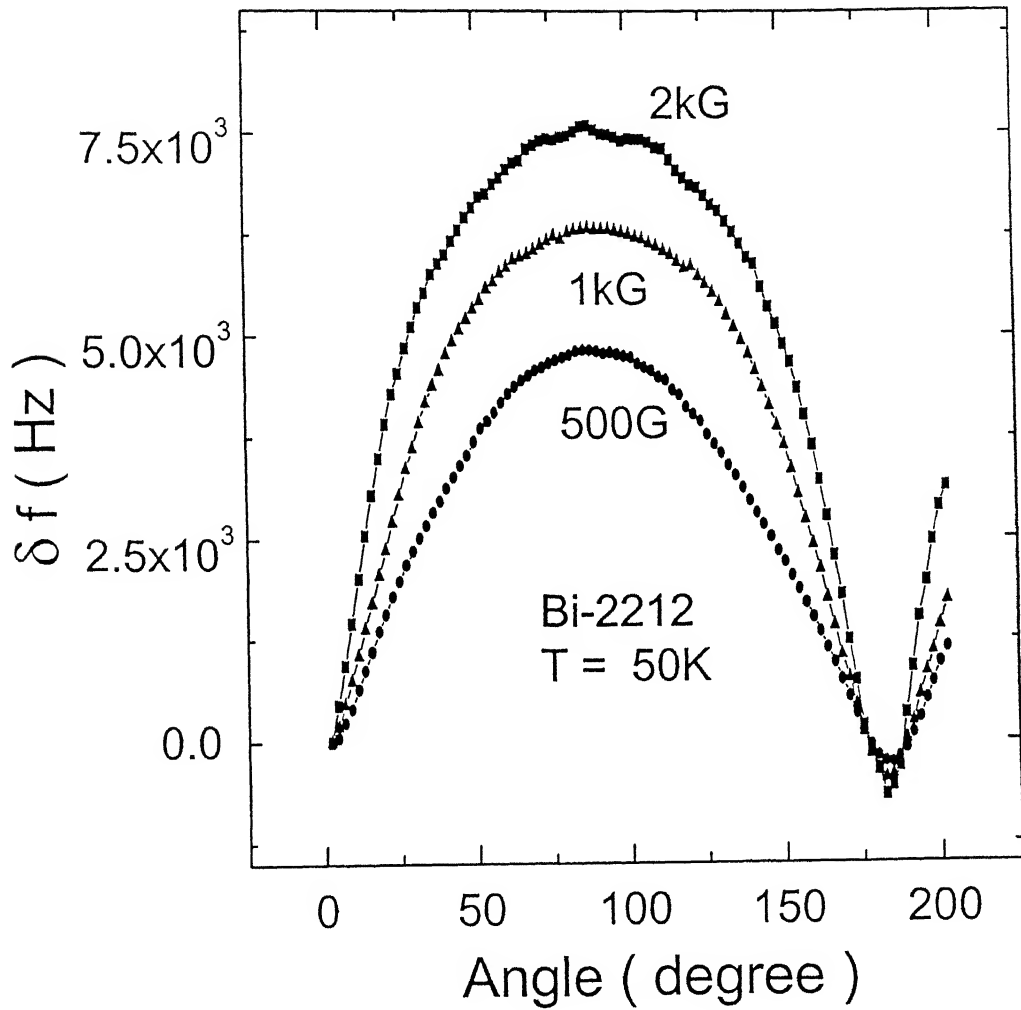


Figure 7.7 Frequency shift δf as a function of angle at 50 K with external dc field of magnitude 0.5, 1 and 2 kG. Notice the sharp cusp in inductive response when the field is made parallel to the ab-plane of the sample. Here $\delta f = f(H, T, 0^\circ) - f(H, T, \theta)$.

We next discuss the angular dependence of rf vortex dynamics in these platelet samples. In Fig. 7.8 is shown the behaviour of δf at 40 K as a function of applied dc field at several values of the angle between the field and the plane of the platelet (*ab* - plane of Bi-2212 lattice). In the inset of the Fig. 7.8 we show an enlarged view of the data between the field range 0 to 1 kG. We notice two interesting features in the data; first the plateau at ~ 0.5 kG in the $\theta = 90^\circ$ data disappears as the field become parallel to the *ab* - planes. This feature is essentially due to the melting of a 3D vortex state. The second feature of the data is the another plateau that develops between 0 and 200 Gauss field as θ goes from ~ 8 to ~ 40 degree (see inset of the Figure). This feature shifts to still lower fields in the data taken at 60 K (Fig. 7.9). We attribute this change to unlocking of the vortices trapped between the *ab* - plane as the normal component of the field exceeds a threshold value. The flux lock-in effect in layered superconductors due to a large suppression of the order parameter between superconducting plains has been discussed by Feinberg and Villard [36] and also by Bulaevskii, Ledvij and Kogan [118]. In this framework, as the normal component of the field increases beyond a threshold value, a steplike field penetration takes place in which large segments of Josephson vortices between the planes are linked by 2D pancake vortices. The response of the system is essentially controlled by these highly mobile 2-dimensional fluxons. As the perpendicular component exceeds the threshold value, there is a sharp crossover to a regime where the dynamics is controlled by 2D pancakes. One would expect the critical value of the applied field at which unlocking takes place to decrease with the angle θ and temperature T . The data of Figures 7. 8 and 7.9 indeed show this feature.

7.2.4 Determination of anisotropy factor γ

We now discuss the overall angular dependence of the rf response at temperatures above the irreversibility line where even at the low fields used in these experiments the vortex state is two dimensional. For a truly 2D system, the number of vortices is given by the normal component of the field (H_L) only. The response of the system therefore must scale with H_L . In order to investigate the 2D behaviour, in Fig. 7.10 we replot the

measurement of δf at 60 K (Fig. 7.9) as a function of c-axis component of the field ($H \sin \theta$).

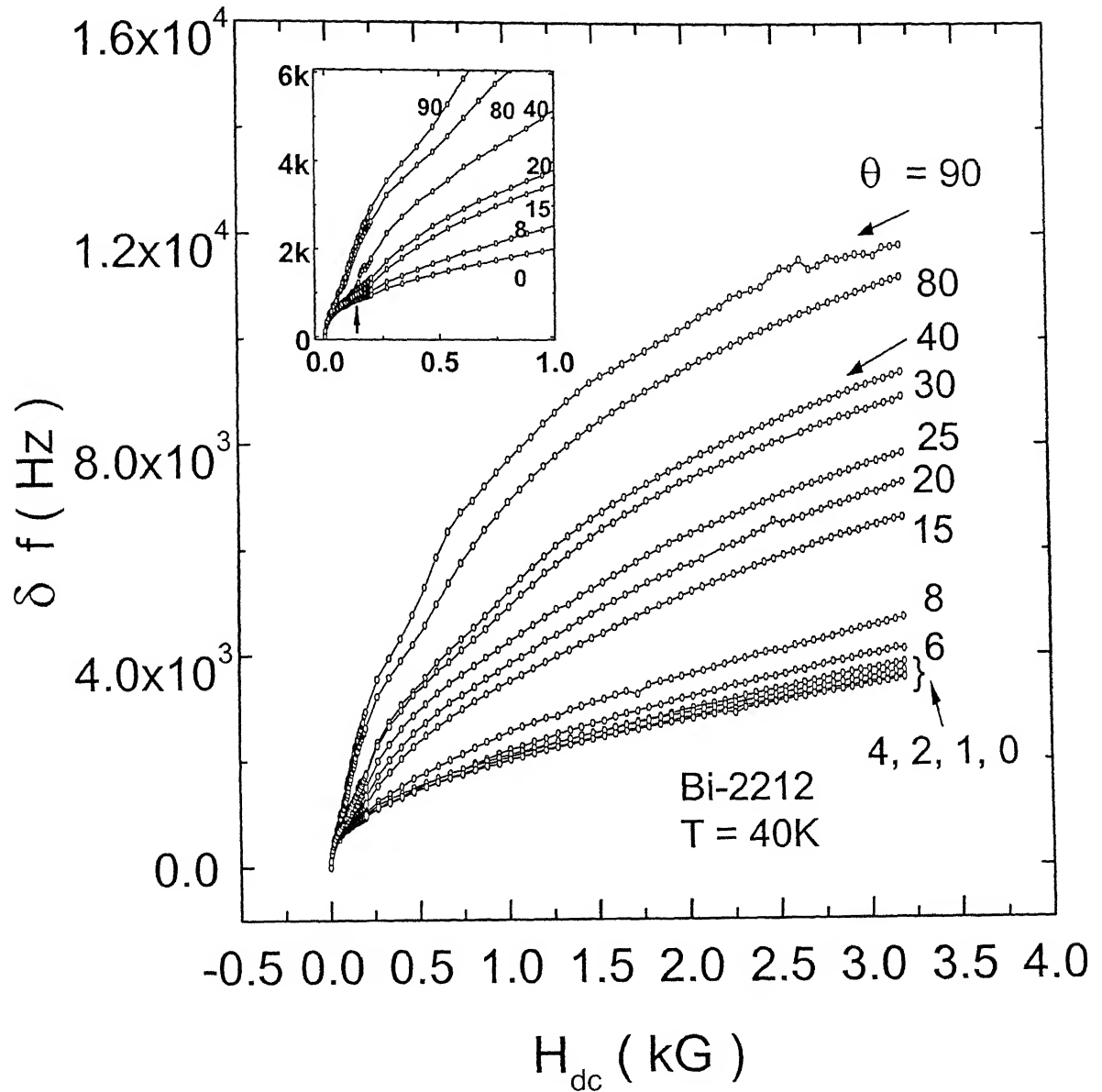


Figure 7.8 Field scans at various angles with respect to ab plane of the sample ($\theta = 0^\circ$ is the parallel to plane configuration) at $T = 40$ K. The inset shows low field regime. The critical value of applied field for vortex unlocking from the planes decreases with increasing angle.

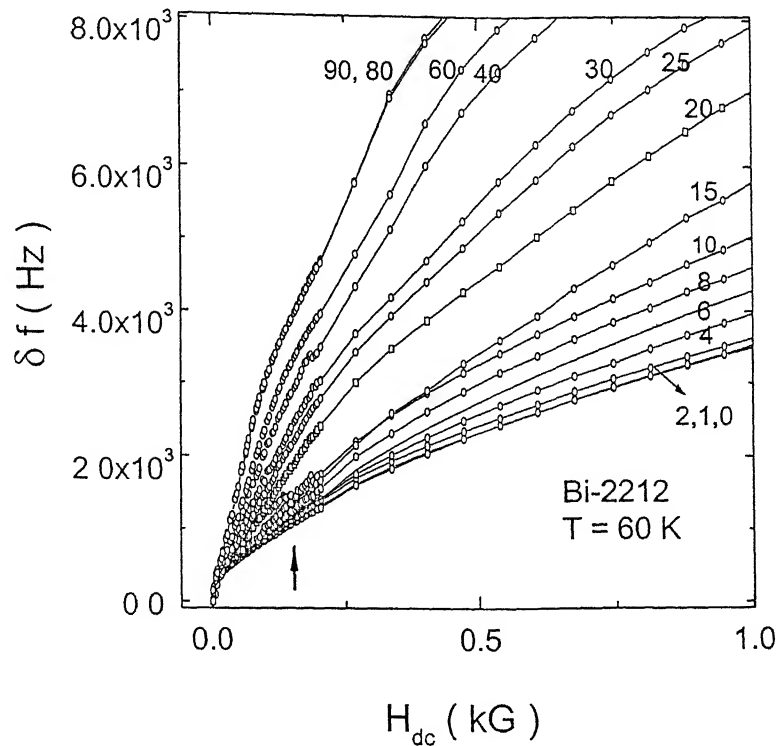


Figure 7.9 Field scans at different angles with respect to ab plane of the sample at $T = 60$ K.

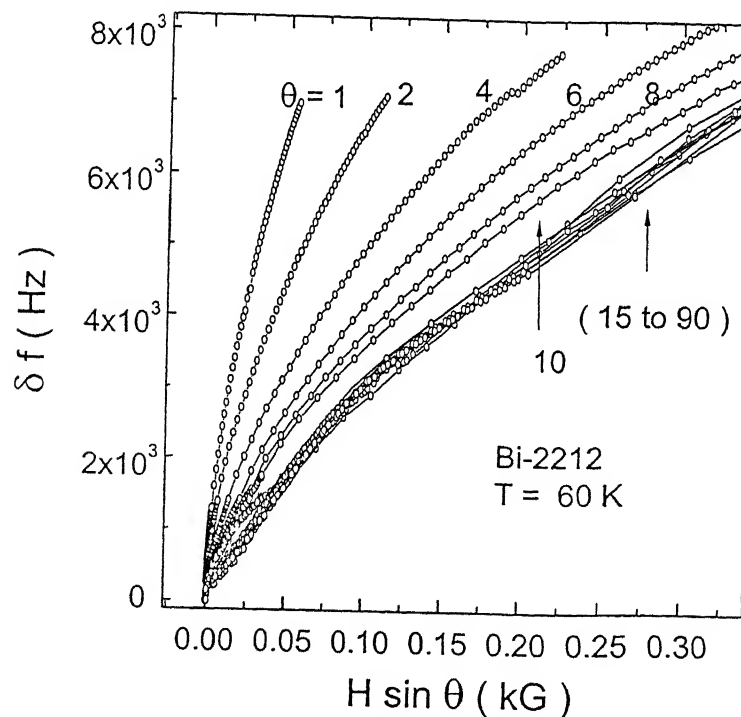


Figure 7.10 The data of Fig. 7.9 as a function of the c-axis component, $H \sin \theta$, of the external field. All the curves collapse into a narrow band for angle θ between 15° to 90° with respect to ab plane.

The curves collapse into a single curve at different values of the angle (with respect to the ab plane) except those taken at $\theta < 15^\circ$. Equivalently, it can be said that the curves are scaled with a scaling parameter ($1 / \sin \theta$). Clearly for $\theta \sim 0^\circ$, this scaling leads to unphysical divergence. The large deviations from 2D scaling at lower angles signifies a non - zero coupling between the superconducting planes and some microstructure related misorientation between the ab planes. This can be modeled in term of a condensate mass anisotropy. Following Raffy et al. [119], we redefine the effective normal component of the field as;

$$H_{\perp} = H(\theta) / \beta \quad (7.1)$$

where $\beta(\theta)$ is a scaling parameter required to collapse all the field scans at different angles to a single curve. The value of $\beta(\theta)$ thus obtained from the translation of each curve to set the best superposition, is used to plot δf Vs. $H / \beta(\theta)$ in a log scale in Fig 7.11. And finally the scaling function $\beta(\theta)$ is plotted as a function of $2\theta / \pi$ on a log - log scale in Fig. 7.12. We have fitted this curve for β to the anisotropic mass model [31],

$$\beta(\theta) = \frac{H(\theta)}{H_{\perp}} = \frac{\gamma}{(\gamma^2 \sin^2 \theta + \cos^2 \theta)^{1/2}} \quad (7.2)$$

with $\gamma = (m_c / m_{ab})^{1/2}$.

The best fit is obtained for $\gamma \approx 10$ at 60 K. Compared to single crystals ($\gamma = 140$) [104] and thin films ($\gamma = 36$) [119] this is rather small. The deviation are essentially due to a non - zero misalignment between the superconducting platelets in these tape samples. A low (~ 6.5) value of γ has also been inferred by Kazumata et al. [57] from dc transport measurements on Bi-2212 tapes prepared by using the doctor blade technique. Fig. 7.12 also shows a fitting assuming $\beta(\theta) = 1 / \sin \theta$. Clearly such scaling is valid only at angles close to c - axis of the sample.

7.2.5 Field dependence of 0.5 T irradiated Bi-2212

The field scans for 0.5 T irradiated samples shown in Fig. 7.13 are entirely different. For $35 \text{ K} < T < 65 \text{ K}$ a strikingly reentrant behaviour is observed. This is in the sense that the rf field penetration decreases with increasing dc field. This is unusual because it implies enhancement of microscopic screening with increasing dc field magnitude.

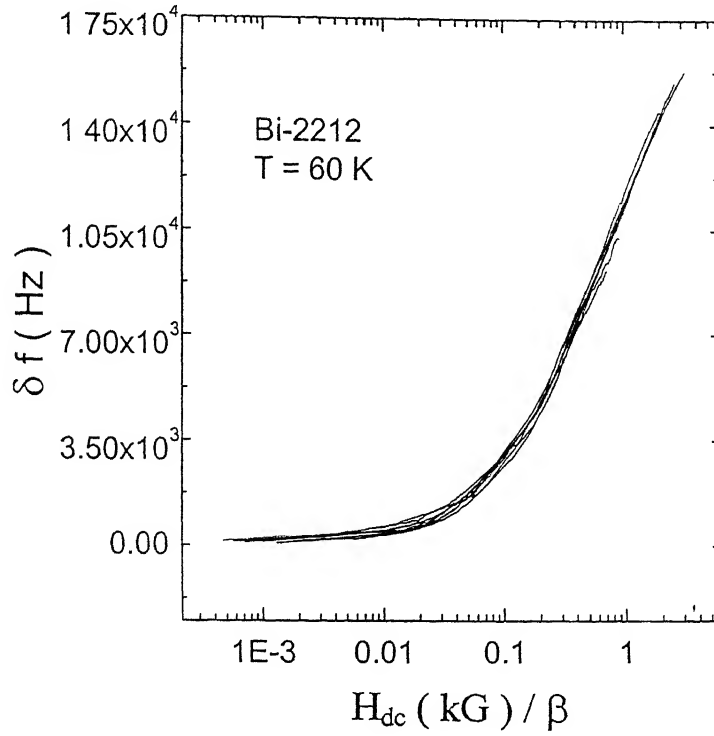


Figure 7.11 Variation of inductive response as a function of $H / \beta (\theta)$ on a logarithmic scale at $T = 60$ K.

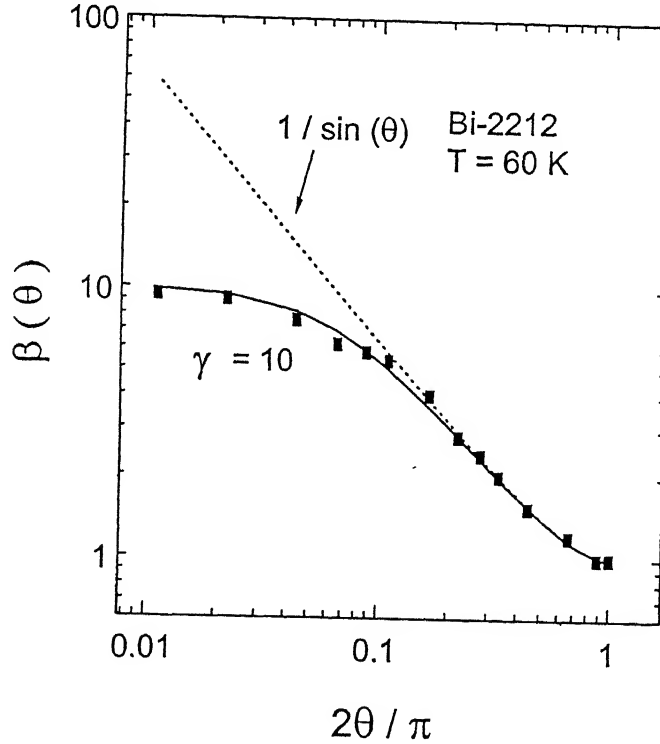


Figure 7.12 Scaling parameter $\beta (\theta)$ as a function of $2\theta / \pi$ for Bi-2212 tape sample at $T = 60$ K. The dotted line is a scaling with $1 / \sin \theta$. The solid line is a best fit to the anisotropic effective mass model (see text) and yields an anisotropy $\gamma = 10$.

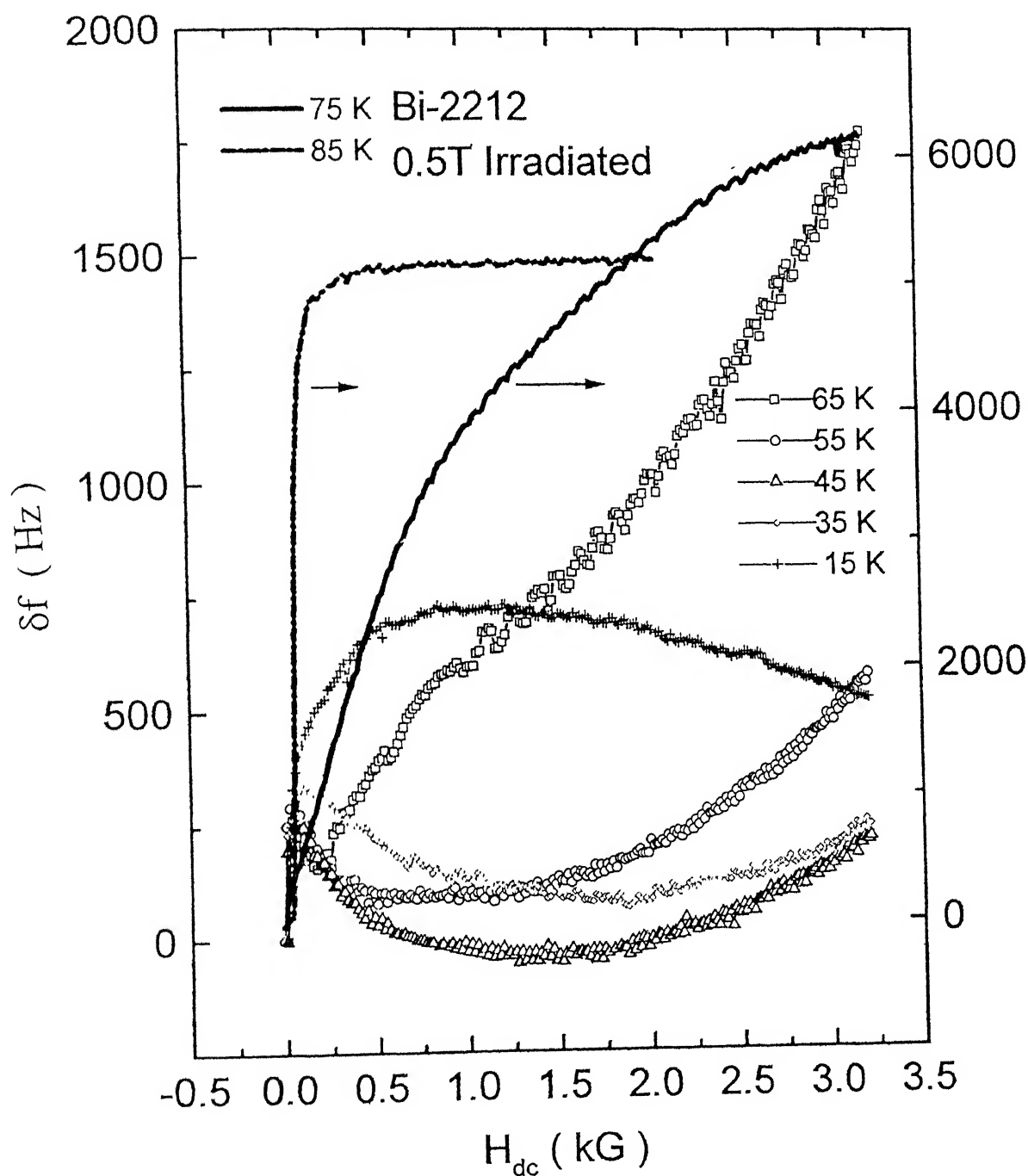


Figure 7.13 Field scans at different temperature for 0.5 T irradiated Bi-2212 platelets. A reentrant behaviour is observed for $35 \text{ K} < T < 65 \text{ K}$. Right y-axis is scaled for 75 K and 85 K.

The key features of this behaviour are; i) this behaviour is not seen in $H \parallel ab$ plane, ii) the onset of decrease in δf and the minima in δf shifts to lower fields with increasing temperature and iii) this non monotonic behaviour vanishes for $0.7 < T/T_c < 0.3$

Reentrant behaviour in c-axis magnetoresistance measurements has been observed by Morozov et. al. in heavy ion irradiated Bi-2212 single crystals [120]. Distinct anomalies have been reported near fractional filling of the columnar defects in Josephson Plasma Resonance experiments as well [121]. Theoretically, this behaviour has been studied by Bulaevskii, Maley and Vinokur (BMV) [122]. To explain the anomalous behavior, it is argued that at low magnetic fields, practically all the vortices are localized in the columnar defect sites but many defect sites remain unoccupied. With increasing external field, as the melting line is exceeded, it becomes energetically favorable for the vortex lines to dissociate into weakly coupled pancakes. The pancakes are still confined to the CDs but due to loss of c-axis correlation, the line tension of vortices is substantially reduced. In our rf experiment, with the DC field applied parallel to the c-axis, this situation implies a reduced penetration of ac field into the sample and consequent decrease in δf . As the applied field increases, so does the filling of defect sites by the pancakes and corresponding to some particular field strength, the out of plane attractive interaction between the pancakes dominate and the vortices regain their c-axis correlation. The overall impact is a reentrance to a line like behaviour and this is understood as a field induced transition from a decoupled liquid state to a coupled liquid state. In the c-axis transport measurements by Morozov et. al. a well defined minima appears at a field corresponding to $B_\phi/4$ in a narrow temperature range. It was also pointed out that the anomaly is better pronounced at lower current values. In our rf experiments where the probe current is negligible (induced by an ac field of $\sim 4 \mu T$), the minima is seen at field value ~ 1.25 kG which is one fourth of the defect density. But the temperature range over which this anomaly is observed is rather broad. At very low temperatures (e.g. 15 K) the reentrant behaviour disappears. Such results are in conformity with experiments by Klein et al. [92] where they notice complete loss of anisotropic pinning at columnar defect sites below 40 K at all fields for Bi-2212 single crystal.

7.3 Summary

In this section we studied the influence of temperature and dc magnetic field on the screening of a weak radio - frequency field by textured tape samples of $\text{Bi}_2\text{Sr}_2\text{CaCu}_2\text{O}_8$ superconductor. The rf screening response shows a single crystal like cusp when the external magnetic field is brought into alignment with the plane of the tape. This anisotropy indicates a platelet type growth of superconducting crystallites with their c-axis normal to the plane of the tape. This inference is supported by direct observation of the surface topography of these samples. The field dependence of rf response suggests the presence of a moderately pinned 3D vortex solid which shows a distinctly different dynamics at high temperatures and fields. This change in dynamics indicates melting of the 3D vortex state to a liquid of two - dimensional vortices. In the angular dependence of the response, we see features of flux lock-in between the Cu-O planes. The angle dependent response in the liquid state scales with normal component of the field. The small value of the mass anisotropy parameter inferred from this analysis suggests some deviations in the parallel alignment of the platelets. With heavy ion irradiation a curious reversal in rf field penetration is observed and the results are discussed by drawing analogy with similar reentrant features seen in c-axis magnetoresistance experiments on Hg Bi-2212 single crystals.

Chapter 8

Conclusion and scope for further work

In this last chapter of the thesis, important results of the present study are summarized. First the pinning and flux flow behavior of vortices in Bi-2223 tapes is discussed. The angular dependence of vortex dynamics due to extrinsic pinning is presented next, followed by studies on granularity and hysteretic aspects in as grown and heavy ion irradiated Bi-2223 tapes. The important results of flux transformer experiment on Bi-2223 and rf vortex dynamics in Bi-2212 tapes are briefly reviewed. In the end a list of possible improvement in the present work are suggested.

8.1 Pinning and flux flow properties of Bi-2223 tapes

Using a high frequency oscillator technique we have made a detailed study of the mixed state properties of highly c-axis oriented Bi-2223 superconductors. Our measurements of rf penetration depth in the unirradiated and heavy ion irradiated platelets of this superconductor unambiguously establish granularity in these composite conductors. The high frequency measurements also enabled us to quantitatively estimate the pinning force constants and its enhancement under heavy ion irradiation for the first time. The different field regimes where the response changes from grain boundary - to - intragrain - to - flux flow dominated with the increasing external dc field strength are ascertained and the corresponding critical fields are obtained. While for the unirradiated sample, the angular dependence of pinning force constant k_p shows that for $T > 85$ K and $\theta > 8^\circ$ the dynamics is essentially controlled by 2D pancakes, in the 0.5 T irradiated platelets a significant increase in k_p is observed for field direction parallel to the columnar tracks at temperature as high as 80 K.

8.2 Angle selective response in HII Bi-2223 tapes

The localization effects at columnar defect sites as functions of temperature, defect density, anisotropy and magnetic field strength are studied through a precision angle dependent measurement. On HII samples the angular studies revealed cusp like features when the external magnetic field is brought into alignment with the defect sites down to 60 K for the 0.5 T irradiated sample and down to 55 K for the 3 T irradiated sample. At temperature very close to T_c the anisotropic pinning vanishes and it is shown that a threshold field is necessary to see the cusp at these temperatures. The overall effects of localization of vortices at columnar defect sites is discussed in the frame work of Bose glass theory applied to anisotropic systems.

8.3 Granularity and hysteresis

Our high frequency hysteresis experiments have detected an anomalous behaviour under field cycling. This behaviour has been assigned to characteristic macroscopic granularity in tape samples. Both in the weak and strong pinning regimes the results have been quantitatively interpreted in terms of the two level critical state model of Ji, Rzechowski, Anand and Tinkham. This analysis also enabled us to calculate the intragrain critical current density and we could compare the enhancement in J_c due to heavy ion irradiation.

8.4 Transport measurements in the FT geometry

The dc transport measurements in the flux transformer geometry shows that the suppression of c-axis correlation takes place at a higher temperature (as the sample is heated from the cooled state) compared to the onset of normal state in ab plane. This two level transition which had been previously seen in twinned YBCO and heavy ion irradiated Bi-2212 is seen in the unirradiated Bi-2223 tapes for the first time. The studies imply that there are two liquid regimes below the transition both in the unirradiated and 3 T irradiated case. For the unirradiated case we also observed the decoupled pancake phase in conformity with our rf measurements. From the Arrhenius plots we could estimate the activation energy for vortex motion in both unirradiated and irradiated Bi-2223 tape samples.

8.5 Vortex dynamics in Bi-2212 tapes

The rf screening response in Bi-2212 tapes delineates the low field 3D vortex phase from the high field pancake liquid regime. The field scans at different angles with respect to ab-plane reflect features similar to lock-in effects. The mass anisotropy and the Ginzburg number are calculated to be ~ 10 and 0.77 respectively and the small value of mass

anisotropy is assigned to finite misorientation between the platelets. An isothermal constant field angular scan on the other hand shows very sharp peaks at $H \parallel ab$ plane almost comparable to single crystals. A comparison of normalized pinning force constant between Bi-2223 and Bi-2212 tapes show higher density of pinning centers in the former. With heavy ion irradiation a marked reentrant behaviour is observed in a broad range of temperature and the results are understood as a field driven transition from a decoupled liquid regime to a coupled liquid state.

8.6 Scope for further work

1) From the experimental technique point of view the following improvements can be made.

a) Although with a close cycle refrigerator we could achieve a stability of the order of 1 Hz in 10^7 Hz, which is sufficient to describe the effects discussed in this thesis, an order magnitude improvement in stability can be achieved by using liquid helium cryostats. Such studies will be important in modeling the frequency response in the TAFV regime due to better overall thermal stability. Fundamental superconducting parameters like London penetration depth and scaling parameters related to pinning and vortex phase transitions can also be determined with greater accuracy if these experiments are carried out with greater stability.

b) In all our high frequency experiments rf field is always perpendicular to the dc field and the frequency is held constant. The frequency can be varied by using a variable capacitor in the LC component of the tunnel diode circuit and the frequency dependence can be studied. Further, the magnitude of the frequency shift would be enhanced manyfold if rf field is applied perpendicular to the sample plane but this configuration has limitations for angular studies with a superimposed dc field.

c) In the flux transformer experiment, the effect of silver is not completely ruled out. It will be better if the silver sheath is removed chemically and contacts are placed by silver evaporation. This would eliminate the silver contribution entirely.

II) The maximum field in all our experiments was ~ 8 kG and for rf experiment we had to restrict ourselves to 3.2 kG. The localization of vortices are best studied when the field values are equal to that of defect density. Both for 0.5 T and 3 T sample we could not access this field regime. High field studies are essential to make conclusive statements on the Bose glass theory of localization of vortices in these anisotropic superconductors.

III) From the FT measurements, we have not done any analysis on the nature of conductivity in the Bi-2223 tapes. While for YBCO the conductivity is established to be non-local (there are some reports against it also), both for unirradiated and heavy ion irradiated Bi-2212 single crystals the conductivity has been shown to be local. The conclusion on the type of conduction mechanism would require proper understanding of current flow path in this ordered granular material.

IV) In our rf measurements, the transition from pinning to flux flow dominated regime is not sharp. This is presumably due to thermally activated flux motion. In our analysis, we have used only the simplest case of Coffey - Clem model where these effects are neglected. The full Coffey- Clem model may be applied for a more quantitative analysis of high temperature data. Further the angular dependence of penetration depth can also be analyzed within the framework of the full Coffey-Clem model.

References

1. P. G. de Gennes, *Superconductivity of Metals and Alloys*, W. A. Benjamin, New York, (1966).
2. A. A. Abrikosov, JETP 5, 1174 (1957).
3. G. Blatter, M. V. Feigel'man, V. B. Geshkenbein, A. I. Larkin, and V. M. Vinokur, Rev. Mod. Phys. 66, 1125 (1994).
4. G. W. Crabtree and D. R. Nelson, Physics Today 50, 4, 38 (1997).
5. R. C. Budhani, Ind. J. Pure and Appl. Phys. 33, 485 (1995).
6. Y. Zhu, Z. X. Cai, R. C. Budhani, M. Suenaga, and D. O. Welch, Phys. Rev. B 48, 6436 (1993).
7. M. Konczykowski, F. Rullier - Albenque, E. R. Yaloby, A. Shaulov, Y. Yeshurun, and P. Lejay, Phys. Rev. B 44, 7167 (1991).
8. W. Gerhäuser, H. W. Neumüller, W. Schmidt, G. Ries, O. Eibl, G. Saemann-Ischenko, and S. Klaumünzer, Physica C 185 - 189, 2339 (1991).
9. L. Civale, A. D. Marwick, T. K. Worthington, M. A. Kirk, J. R. Thomson, L. Krusin-Elbaum, Y. Sun, J. R. Clem, and F. Holtzberg, Phys. Rev. Lett. 67, 648 (1991).
10. L. Krusin-Elbaum, L. Civale, G. Blatter, A. D. Marwick, F. Holtzberg, and C. Feild, Phys. Rev. Lett. 72, 1914 (1994).
11. M. E. McHenry and R. A. Sutton, Progress in Material Science 38, 159 (1994).
12. D. R. Nelson and V. M. Vinokur, Phys. Rev. Lett. 68, 2398 (1992).
13. J. Bardeen and M. J. Stephen, Phys. Rev. 140, A1197 (1965).
14. P. W. Anderson, Phys. Rev. Lett. 9, 309, (1962).
15. M. Golosovsky, M. Tsindlekht and D. Davidov in G. Deutscher and A. Revcolevschi (eds.), *Coherence in High Temperature Superconductors*, World Scientific, Singapore, (1996), p 247.
16. J. I. Gittleman and B. Rosenblum, Phys. Rev. Lett. 16, 734 (1966).
17. A. M. Campbell, J. Phys. C 4, 3186 (1971).
18. E. H. Brandt, Phys. Rev. Lett 67, 2219 (1991).

19. M. W. Coffey and J. R. Clem, Phys. Rev. Lett. 67, 386 (1991).
20. S. Sridhar, B. Maheshwaran, B. Willesmen, D. H. Wu, and R. C. Haddon, Phys. Rev Lett. 68, 2220 (1992).
21. H. Suhl, Phys. Rev. Lett. 14, 226 (1965).
22. E. J. Pakulis and T. Osada, Phys. Rev. B 37, 5940 (1988).
23. L. Ji, M. S. Rzchowki, and M. Tinkham, Phys. Rev. B 42, 4838 (1990).
24. A. M. Portis, K. W. Blazey, K. A. Müller, and J. G. Bednorz, Europhys. Lett. 5, 467 (1988).
25. L. Ji, M. S. Rzchowski, N. Anand, and M. Tinkham, Phys. Rev. B 47 470 (1993).
26. M. Pozek, A. Dulcic, B. Rakvin, Physica C 197, 175 (1992).
27. S. V. Bhat, P. Ganguly, T. V. Ramakrishnan, and C. N. R. Rao, J. Phys. C20, L559 (1987).
28. M. D. Sastry in Anant Narlikar (ed.) *Studies on High Temperature Superconductors*, Vol - II, Nova Science Publishers, Inc., New York (1989), p255.
29. P. Chaddah, S. B. Roy, S. Kumar, A. K. Pradhan, R. Prasad, and N. C. Soni, Ind. J. Pure and Appl. Phys. 32, 541 (1994).
30. V. G. Kogan, Phys. Rev. B 24, 1572 (1981).
31. W. E. Lawrence and S. Doniach in E. Kanda (ed.) *Proc. 12th Int. Conf. Low Temp. Phys.*, Kyoto, Japan (1970) p. 361.
32. J. R. Clem, Phys. Rev. B 42, 4135 (1990).
33. L. I. Glazman and A. E. Koshelev, Phys. Rev. B 43, 2835 (1991).
34. M. Tinkham, *Introduction to superconductivity*, McGraw - Hill, Inc., Singapore (1996).
35. D. S. Fisher, M. P. A. Fisher, and D. Huse, Phys. Rev. B 43, 130 (1991).
36. D. Feinberg and C. Villard, Phys. Rev. Lett. 65, 919 (1990).
37. L. N. Bulaevskii, L. L. Daemen, M. P. Maley, and J. Y. Coulter, Phys. Rev. B 26, 13798 (1993).
38. A. P. Malozemoff, in S. H. Wihang et. al. (eds.), *High temperature superconducting compounds - II*, TMS publications, Warrendale PA, (1990), p3.
39. A. E. Pashitski, A. Polyanskii, A. Gurevich, J. A. Parrell, and D. C. Larbalestier, Physica C 246, 133 (1995).

40. J. E. Tkaczyk, R. H. Arendt, M. F. Garbauskas, H. R. Hart, K. W. Lay, and F. E. Luborsky, Phys. Rev. B 45, 12506 (1992).
41. P. J. Kung, M. E. McHenry, M. P. Maley, P. H. Kes, D. E. Laughlin, and W. W. Mullins, Physica C 249, 53 (1995).
42. Y. Fukumoto, H. J. Wiesmann, M. Garber, M. Suenaga, and P. Haldar, J. Appl. Phys. 78, 4584 (1995).
43. M. Ciszek, A. M. Campbell, and B. A. Glowski, Physica C 233, 203 (1994).
44. S. Labdi, H. Raffy, O. Laborde, and P. Monceau, Physica C 197, 274 (1992).
45. H. Yamasaki, K. Endo, Y. Nakagawa, M. Umeda, S. Kosaka, S. Misawa, S. Yoshida, and K. Kajimura, J. Appl. Phys. 72, 2951 (1992).
46. Qiang Li, M. Suenaga, J. Gohng, D. K. Finnemore, T. Hikata, and K. Sato, Phys. Rev. B 46, 3195 (1992).
47. M. Kiuchi, E. S. Otabe, T. Matsushita, T. Kato, T. Hikata, and K. Sato, Physica C 260, 177 (1996).
48. J. Tenbrink and H. Krauth in H. Maeda and K. Togano (eds.), *Bismuth based High Temperature Superconductors*, Marcel Dekker, Inc. New York, (1996), p369.
49. K. Shibutani, H. J. Wiesmann, R. L. Sabatini, M. Suenaga, S. Hayashi, R. Ogawa, Y. Kawate, L. Motowidlo, and P. Haldar, Appl. Phys. Lett. 64, 924 (1994).
50. J. H. Cho, M. P. Malay, J. O. Willis, J. Y. Coulter, L. N. Bulaevskii, P. Haldar, and L. R. Motowidlo, Appl. Phys. Lett. 64, 3030 (1994).
51. Y. Sun, G. Y. Xu, J. Du, Y. Zhou, R. Zeng, X. Fu, P. Hua, and Y. Zhang, Phys. Rev. B 54, 1382 (1996).
52. Qing Li, H. J. Wiesmann, M. Suenaga, L. Motowidlow, and P. Haldar, Phys. Rev. B 50, 4256 (1994).
53. H. W. Neumüller, W. Gerhäuser, G. Ries, P. Kummeth, W. Schmidt, S. Klaumünzer, and G. Saemann-Ischenko, Cryogenics 33, 14 (1993).
54. L. Civale, A. D. Marwick, R. Wheeler, M. K. Kirk, W. L. Carter, G. N. Riley, and A. P. Malozemoff, Physica C 208, 137 (1993).
55. P. Kummeth, C. Stuller, H. W. Neumüller, and G. Saemann-Ischenko, Appl. Phys. Lett. 65, 1302 (1994).

- 56 Y. Fukumoto, Y. Zhu, Q. Li, H. J. Weismann, M. Suenaga, T. Kaneko, K. Sato, K. Shibusaki, T. Hase, S. Hayashi, and Ch. Simon; Phys. Rev. B, Vol. 54, 10210 (1996).
- 57 Y. Kazumata, H. Kumakura, and K. Togano, Phys. Rev B 54, 16206 (1996).
58. Picdong Yang and C. M. Lieber, Science 273, 1836 (1996).
59. E. Laurmann and D. Sohenberg, Nature 160, 747 (1947).
- 60) A. L. Schawlow and D. E. Devlin, Phys. Rev. 113 , 120 (1959).
- 61 S. M. Anlage, B. W. Langley, G. Deutscher, J. Halbritter, and M. R. Beasley, Phys. Rev. B 44, 9764 (1991).
62. Dong - Ho Wu and S. Sridhar, Phys. Rev. Lett 65, 2074 (1990).
63. I. Giaever, Phys. Rev. Lett. 15, 825 (1965).
64. Y. -I. Wang, W. Bian, Y. Zhu, Y. Fukumoto, H. J. Wiesmann and M. Suenaga, T. R. Thurston, K. Merken, and S. Hong, J. Electronic Materials 24, 1817 (1995).
65. M. S. Walker, D. W. Hazelton, M. T. Gardner, J. A. Rice, D. G. Walker, C. M. Trautwein, N. J. Ternullo, Xin Shi, J. M. Weloth, R.S. Sokolowski, and F.A. List, IEEE Trans. Appl. Superconductivity 7, 889 (1997).
66. C. Varnazis and M. Strongin, Phys. Rev. B 10, 1885 (1974).
67. S. Yan, Q. Jia, X. Wang, G. Xia, and H. Ma, Int. J. Mod. Phys. 1, 469 (1987).
68. A. E. Koshelev and V. M. Vinokur, Physica C 173, 465 (1991).
69. S. Sridhar, C. A. Shiffman, and H. Hamdeh, Phys. Rev. B 36, 2301 (1987).
70. C. Boghosian, H. Mayer, and J. E. Rives, Phys. Rev. 146, 110 (1966).
71. G.E. Tunnel Diode Manual
72. R. B. Goldfarb, M. Lelental, and C. A. Thompson in R. A. Hein, T. L. Francavilla, and D. H. Liebenberg (eds.), *Magnetic susceptibility of superconductors and other spin systems*, Plenum press, New York (1991), p.56.
73. Y. Iye, S. Nakamura, and T. Tamagai, Physica C 159, 433 (1989).
74. T. T. M. Palstra, B. Batlogg, R. B. Vandover, L. F. Schneemeyer, and J. V. Waszczak, Appl. Phys. Lett. 54, 763 (1989).
75. R. C. Budhani, D. O. Welch, M. Suenaga, and R. L. Sabatini, Phys. Rev. Lett. 64, 1666 (1990).
76. K. A. Muller, M. Takashige, and J. G. Bednorz, Phys. Rev. Lett. 58, 1143 (1987).

77. Y. Yeshurun and A. P. Malozemoff, Phys. Rev. Lett. 60, 2202 (1988).
78. Y. Xu, M. Suenaga, Y. Gao, J. E. Crow, and N. D. Spencer, Phys. Rev. B 42, 8756 (1990).
79. T. Matsushita, E. S. Olabe, M. Kiuchi, B. Ni, T. Hikata, and S. Sato, Physica C 201, 151 (1992).
80. A. F. Hubbard, P. L. Gammel, C. E. Rice, and A. F. J. Levi, Phys. Rev. B 40, 5243 (1989)
81. M. Golosovsky, M. Tsindlekht, H. Chayet, and D. Davidov, Phys. Rev. B 50, 470 (1994).
82. T. Hanaguri, Y. Iino, A. Maeda, N. Motohira, and K. Kishio, Physica C 235-240, 1991 (1994).
83. P. A. Mansky, P. M. Chaikin, and R. C. Haddon, Phys. Rev. Lett. 70, 1323 (1993) and Phys. Rev. B 50, 15929 (1994).
84. H. Enriquez, N. Bontemps, P. Fournier, A. Kapitulnik, A. Maignan, and A. Ruyter, Phys. Rev. B 53, 14757 (1996).
85. W. Gerhauser, G. Ries, H. W. Neumuller, W. Schmidt, O. Eibl, G. Saenamm-Ischenko, and S. Klaumunzer, Phys. Rev. Lett. 68, 879 (1992).
86. M. Giura, R. Marcon, R. Fastampa, and E. Silva, Phys. Rev. B, 45, 7387 (1992).
87. M. Tachiki and S. Takahashi in H. Maeda and K. Togano (eds.), *Bismuth based High Temperature Superconductors*, Marcel Dekker, Inc. New York, (1996), p153.
88. L. Civale, Supercond. Sci. Technol. 10, A11 (1997).
89. R. C. Budhani, W. L. Holstein, and M. Suenaga, Phys. Rev. Lett. 72, 566 (1994).
90. R. C. Budhani, M. Suenaga, and S. H. Liou, Phys. Rev. Lett. 69, 3816 (1992).
91. J. R. Thompson, Y. R. Sun, H. R. Kerchner, D. K. Christen, B. C. Sales, B. C. Chakoumakos, A. D. Marwick, L. Civale, and J. O. Thomson, Appl. Phys. Lett. 60, 2306 (1992).
92. L. Klein, E. R. Yacoby, Y. Yeshurun, L. Burlachkov, B. Ya Shapiro, M. Konczykowski and F. Holtzberg, Phys. Rev. B 47, 12349 (1993).
93. V. Hardy, A. Wahl, S. Hebert A. Ruyter, J. Provost, D. Groult, and Ch. Simon, Phys. Rev. B 54, 656 (1996).

94. C. J. van der Beek, M. Konczykowski, V. M. Vinokur, T. W. Li, P. H. Kes, and G. W. Crabtree, *Phys. Rev. Lett.* 74, 1214 (1995).
95. A. E. Koshelev, P. Le Doussal, and V. M. Vinokur, *Phys. Rev. B* 53, R8855 (1996).
96. R. C. Budhani, Presented at the *International workshop on Statistics and Dynamics of vortices in Superconductors*, Eugene, Oregon, July, (1993).
97. R. J. Drost, C. J. Van der Beek, J. A. Heijn, M. Konczykowski, and P. H. Kes, *Phys. Rev. B* 58, R615 (1998).
98. B. Hensel, J. C. Grivel, A. Jeremie, A. Perrin, A. Pollini, and R. Flükiger, *Physica C* 205, 329 (1993).
99. A. K. Pradhan, B. K. Roul, S. B. Roy, P. Chaddah, D. Kanjilal, C. Chen, and B. M. Wanklyn, *Solid State Commun.* 101, 367 (1997).
100. G. Ries, H. - W. Nemuller, W. Schmidt, and C. Struller, *Proc. of the 7th Int. Workshop on critical currents in superconductors*, Alpbach, Austria (1994).
101. C. P. Bean, *Rev. Mod. Phys.* 36, 31 (1964).
102. S. L. Lee, P. Zimmermann, H. Keller, M. Warden, I. M. Savic, R. Schauwecker, D. Zech, R. Cubitt, E. M. Forgan, P. H. Kes, T. W. Li, A. A. Menovsky, and Z. Tarnawski, *Phys. Rev. Lett.* 71, 3862 (1993).
103. R. Cubitt, E. M. Forgan, G. Yang, S. L. Lee, D. McK. Paul, H. A. Mook, M. Yethitaj, P. H. Kes, T. W. Li, A. A. Menovsky, Z. Tarnawski, and K. Mortensen, *Nature* 365, 407 (1993).
104. E. Zeldov, D. Majer, M. Konczykowski, V. M. Geshkenbein, V. M. Vinokur, and H. Strikman, *Nature*, 375, 373 (1995).
105. H. Safar, E. Rodriguez, F. de la Cruz, P. L. Gammel, L. F. Schneemeyer, and D. J. Bishop, *Phys. Rev. B* 46, 14238 (1992).
106. R. Busch, G. Ries, H. Werthner, G. Kreiselmeier, and G. Saemann- Ischenko, *Phys. Rev. Lett.* 69, 522 (1992).
107. R. A. Doyle, W. S. Seow, Y. Yan, A. M. Campbell, T. Mochiku, K. Kodowaki, and G. Wirth, *Phys. Rev. Lett.* 77, 1155 (1996).
108. H. Safar, P. L. Gammel, D. A. Huse, S. N. Majumdar, L. F. Schneemeyer, D. J. Bishop, D. López, G. Nieva, and F. de la Cruz, *Phys. Rev. Lett.* 72, 1272 (1994).

- 109 D. López, E. F. Righi, G. Nieva, F. de la Cruz, W. K. Kwik, J. A. Fendrich, G. W. Crabtree, and L. Paulius, *Phys. Rev. B* 53, R8895 (1996).
- 110 C. J. van der Beek, M. Konczykowski, V. M. Vinokur, G. B. Crabtree, T. W. Li, and P. H. Kes, *Phys. Rev. B* 51, 15492 (1995).
- 111 Y. M. Wan, S. E. Hebboul, D. C. Harris, and J. C. Garland, *Phys. Rev. Lett.* 71, 157 (1993).
- 112 Y. Zhao, G. D. Gu, J. W. Cochrane, G. J. Russell, J. G. Wen, N. Nakamura, S. Tajima, and N. Koshizuka, *Phys. Rev. B* 51, 3806 (1995).
- 113 T. T. M. Palstra, B. Batlogg, L. F. Schneemeyer, and J. V. Waszczak, *Phys. Rev. Lett.* 61, 1662 (1988).
- 114 H. Safar, J. H. Cho, L. N. Bulaevskii, M. P. Maley, R. C. Budhani, J. D. Hettinger, and K. E. Gray (unpublished results).
- 115 L. N. Bulaevskii, S. V. Meshkov, and D. Feinberg, *Phys. Rev. B* 43, 3728 (1991).
- 116 P. H. Kes, J. Aarts, V. M. Vinokur, and C. J. van der Beek, *Phys. Rev. Lett.* 64, 1063 (1990).
- 117 C. J. van der Beek, P. H. Kes, M. P. Maley, M. J. V. Menken, and A. A. Menovsky, *Physica C* 195, 307 (1992).
- 118 L. N. Bulaevskii, M. Ledvij, and V. Kogan, *Phys. Rev. B*, 46, 366 (1992).
- 119 H. Raffy, S. Labdi, O. Laborde, and P. Monceau, *Phys. Rev. Lett.* 66, 2515 (1991)
- 120 N. Morozov, M. P. Maley, L. N. Bulaevskii, and J. Sarrao, *Phys. Rev. B* 57, R8146 (1998).
- 121 M. Kosugi, Y. Matsuda, M. B. Gaifullin, L. N. Bulaevskii, N. Chikumoto, M. Konczykowski, J. Shimoyama, K. Kishio, K. Hirata, and K. Kumagai, *Phys. Rev. Lett.* 79, 3763 (1997).
- 122 L. N. Bulaevskii, M. P. Maley, and V. M. Vinokur, *Phys. Rev. B* 57, 5626 (1998).

List of Publications

Journals

1. *Apparatus for vortex dynamics studies in high T_c samples using close cycle refrigerator and RF oscillators*, S. Patnaik, K. J. Singh, and R. C. Budhani, Review of Scientific Instrumentation 70, 1494, (1999).
2. *Radio frequency vortex dynamics in oriented platelets of $(Bi-Pb)_2Sr_2Ca_2Cu_3O_{10}$ superconductor*, S. Patnaik, R. C. Budhani, Y.-L. Yang, and M. Suenaga, Physica C, 309, 221 (1998).
3. *Effects of granularity and strong pinning on high frequency vortex dynamics in $(Bi-Pb)_2Sr_2Ca_2Cu_3O_{10}$ superconducting platelets*, S. Patnaik, R. C. Budhani, and M. Konczykowski (5 Figures and 17 References, Submitted to Solid State Communications).
4. *Radio frequency vortex dynamics in heavy ion irradiated $(Bi-Pb)_2Sr_2Ca_2Cu_3O_{10}$ superconducting platelets*, S. Patnaik, R. C. Budhani, M. Konczykowski, Y. -L. Yang, and M. Suenaga (8 Figures and 32 References, Submitted to Physica C).
5. *Vortex phases and c-axis correlation in as grown and heavy ion irradiated $(Bi-Pb)_2Sr_2Ca_2Cu_3O_{10}$ superconducting tapes; A Flux transformer study*, S. Patnaik, R. C. Budhani, M. Konczykowski, Y. -L. Yang, and M. Suenaga (4 Figures and 23 References, Submitted to Journal of Applied Physics).
6. *Anisotropy dominated radio frequency vortex dynamics in $Bi_2Sr_2CaCu_2O_8$ thick films on silver tapes*, S. Patnaik, R. C. Budhani, and D. W. Hazelton (13 Figures and 29 References, Submitted to Physica C).
7. *Anomalous reentrant inductive response at fractional filling density in heavy in irradiated Bi-2212 tapes*, S. Patnaik and R. C. Budhani (Under preparation).

Conferences

1. *Direct measurement of penetration depth by inductive transition method for $(Bi-Pb)_2Sr_2Ca_2Cu_3O_{10}$ platelets*, S. Patnaik, H. S. Gupta, R. C. Budhani, DAE Solid state Symposium, Bombay, India (1996).
2. *Apparatus for temperature and field dependent studies of magnetic penetration depth of high T_c samples using IC74LSO4 as RF oscillator*, S. Patnaik, K. J. Singh and R. C. Budhani, Contributed paper, DAE Solid State Symposium, Cochin, India (1997).
3. *Enhancement of Pinning force density after heavy ion irradiation in $H \parallel C$ direction in Bi-2223 tape wires*, S. Patnaik and R. C. Budhani, DAE Solid State Symposium, Cochin, India (1997).
4. *Experimental setup for studies of equilibrium and non - equilibrium photo effects in superconducting films*, L. K. Sahoo, Vivek Aji, Kanwaljeet Singh, S. Patnaik, and R. C. Budhani, National Laser Symposium, Ahmedabad, India (1997).
5. *Optimized pulsed laser deposition technique for thin - films of magnetic and superconducting films*, K. J. Singh, V. Bhatt, N. Pandey, S. Patnaik, C. Roy, L.K. Sahoo, M. K. Srivastava, and R. C. Budhani, National Laser symposium, Ahmedabad, India (1997).
6. *Interplay of extrinsic and intrinsic pinning in heavy ion irradiation Bi-2223 superconductors*, S. Patnaik and R. C. Budhani, in "The 5th IUMRS International conference in Asia, Bangalore, India (1998).
7. *Temperature dependent magnetoresistance studies in irradiated and unirradiated Bi-2223/ Ag tape wires*, S. Patnaik, A. Pasupathy, and R. C. Budhani, DAE Solid State Symposium, Kurukshetra, India (1998).